UNIVERSITÀ
DEGLI STUDI
DI CAGLIARI

Ph.D. DEGREE IN
Electronic and Computer Engineering

Cycle XXXVIII

TITLE OF THE Ph.D. THESIS

DEVELOPMENT OF INNOVATIVE SENSORS FOR DETECTING THE WATER STATUS OF PLANTS IN PRECISION AGRICULTURE APPLICATIONS

Scientific Disciplinary Sector(s)

ING-INF/01

Ph.D. Student: Nasreddine Makni

Supervisor Prof. Massimo Barbaro

Final exam. Academic Year 2024/2025
Thesis defence session: February 2026

This thesis is dedicated to the memory of

Monji Ben Amor

my grandfather.

Your love and strength continue to guide me.
May you rest in peace.

Abstract

This doctoral research addresses the development of innovative sensors and integrated systems for the direct assessment of plant water status, a key parameter in precision agriculture and sustainable irrigation. The thesis is organized into three main experimental parts, each addressing a different level of plant-based monitoring, from direct leaf sensing to whole-plant motion and irrigation automation. Unlike conventional approaches that infer water availability indirectly from soil or environmental measurements, this work focuses on plant-based sensing, enabling real-time and non-invasive detection of water stress.

Four complementary approaches were investigated: (i) electrical impedance spectroscopy (EIS) of leaf tissues to characterize physiological and structural changes linked to hydration levels; (ii) optical sensing through near-infrared (NIR) spectroscopy, exploiting absorption variations related to leaf water content; (iii) monitoring of petiole movements using low-power inertial measurement units (IMUs) to capture circadian and stress-induced motion patterns; and (iv) the design and validation of a smart irrigation platform (SPRITZ project) integrating soil and environmental sensors, wireless communication, and automated control via cloud-based IoT infrastructure.

Dedicated electronic boards, embedded firmware, and LoRa-based communication modules were developed to ensure reliable, energy-efficient data acquisition under both controlled greenhouse and outdoor field conditions. Experimental campaigns were carried out on multiple plant species, subjected to differentiated irrigation regimes, to evaluate sensor performance and their correlation with reference physiological indicators such as relative water content (RWC).

Data processing combined statistical analysis, modeling, and machine learning algorithms to extract relationships between sensor outputs and plant water dynamics. Results demonstrated the feasibility and the robustness of the proposed sensing methods, showing that plant-centric measurements can effectively discriminate between hydration levels and environmental treatments.

Overall, this research establishes a comprehensive framework for plant-based IoT sensing, bridging physiological monitoring with automated irrigation control.

The proposed technologies provide a foundation for future multi-sensor fusion systems capable of predictive water management, thereby contributing to improved water-use efficiency and the sustainability of modern agriculture.

Contents

Figures

Tables

1 General Introduction

The escalating global water crisis, driven by climate change and the unsustainable use of groundwater resources, poses a serious threat to agricultural sustainability [17]. This scarcity directly affects irrigation capacity, forcing farmers to abandon traditional crops or switch to drought-tolerant varieties, thereby threatening agricultural biodiversity [18, 19]. Climate change further intensifies this challenge by amplifying the greenhouse effect, which accelerates evapotranspiration and increases water demand even as available resources continue to decline [20, 21]. In addition, global warming alters precipitation patterns, leading to greater aridity in regions such as the Mediterranean basin and sub-Saharan Africa [22, 23].

One of the most promising approaches to address this problem is *precision agriculture*, which uses advanced technologies to optimize the management of agricultural resources. At the core of this concept is the development of sensing systems capable of accurately quantifying plant water requirements, moving beyond indirect indicators such as soil moisture [24].

However, a major challenge remains: the lack of reliable, plant-centered monitoring systems capable of directly assessing plant water status in real time. In parallel, the limited availability of integrated global agricultural databases represents an additional barrier for large-scale resource planning and predictive analytics [25].

This thesis specifically addresses the first challenge by considering the plant itself as the primary indicator of its water needs. It is based on the assumption that

a solid understanding of plant structure and water physiology is fundamental to the development of sensors capable of real-time health monitoring. Accordingly, this research focuses on the design and validation of two complementary techniques: *electrical impedance spectroscopy* and *infrared spectroscopy*, both applied directly to plant leaves. By linking physiological knowledge with sensor technology, the study contributes to the creation of intelligent irrigation systems that respond to the actual physiological state of crops, promoting more resilient and sustainable agricultural practices.

The manuscript is structured as follows:

chapter 2 introduces the fundamental principles that govern plant–water interactions and reviews the main approaches for assessing plant water status.

chapter 3 describes the experimental setups, tools, and characterization techniques used throughout this work.

chapter 4 presents the development of optical and electrical sensors for non-invasive monitoring of plant water status.

chapter 5 details the design and testing of an innovative wireless IMU-based sensor for real-time monitoring of plant movements.

chapter 6 illustrates the implementation of an IoT-based irrigation management platform designed to enhance water-use efficiency and decision-making in small- and medium-sized farming systems.

Overall, this thesis advances the field of precision agriculture by integrating physiological understanding with technological innovation. It demonstrates how the combination of plant-based sensing and IoT connectivity can improve irrigation efficiency and support sustainable water management in the context of a changing climate.

2
State of Art

2.1 Introduction

This chapter provides a comprehensive overview of the biological and technological foundations essential for monitoring plant water status. It begins by examining plant structure and internal water transport mechanisms, with particular focus on leaf anatomy, stomatal regulation, and the concept of water potential. This section also addresses how plants physiologically respond to water stress.

The second part of the chapter introduces the main techniques used to assess plant water status, which are broadly categorized into direct and indirect methods. Direct methods involve measurements closely linked to the plant's internal water potential, such as pressure chamber readings, psychrometric techniques, and osmotic potential analysis, providing physiological and quantitative indicators of plant hydration. Indirect methods, on the other hand, are based on observable plant responses to water stress, including changes in stomatal conductance, leaf temperature, stem diameter, and sap flow. While these techniques do not measure water potential directly, they offer valuable insights into how plants react to drought or suboptimal irrigation.

The third section shifts toward advanced sensor-based approaches, which form the core of the experimental work presented in this thesis. These include electri-

cal impedance spectroscopy (EIS), infrared spectroscopy (NIRS), and the use of inertial measurement units (IMUs) to track petiole orientation. Details on measurement setups, data processing techniques, and modeling strategies are provided to highlight the relevance of these methods for real-time, plant-based water stress detection.

Finally, the chapter reviews the irrigation methods and infrastructures, which cover both traditional surface irrigation and modern pressurized systems. Then, it concludes with an overview of smart irrigation infrastructures, which integrate wireless communication technologies with a focus on LoRaWAN communication and cloud computing platforms to enable data-driven irrigation management. These innovations represent a key advancement in sustainable agriculture, aiming to optimize water use while maintaining crop productivity.

2.2 Plant Structure and Water Physiology

2.2.1 Plant Structure

2.2.1.1 The Roots

Roots anchor the plant and absorb water and minerals from the soil. They can adapt their growth based on water availability, for example by growing deeper in response to drought. Water absorption is regulated by membrane proteins called *aquaporins* [26], which help roots function effectively in both arid and nutrient-rich environments. The absorbed water moves through the *xylem* vessels (a system of interconnected tubes) toward the stem, leaves, and other organs [27, 28]. This upward movement is driven by two main forces: *root pressure*, a positive pressure generated by the active absorption of ions, and *leaf transpiration*, a suction effect caused by water evaporation from the stomata [29].

The root is structured into several zones: a protective *root cap* that shields the apical meristem during growth [30]; a *meristematic zone*, where active cell division occurs; an *elongation zone*, where cells grow in length; and a *maturation zone*, characterized by absorbent root hairs that increase the surface area for water uptake [31, 32]. The root structure is illustrated in Figure 2.1a.

2.2.1.2 The Stem

The stem is a crucial part of the plant. It distributes nutrients, provides structural support, and responds to environmental stressors such as drought and salinity [33,

34, 35, 36]. The stem is composed of specialized tissues, including the *xylem*, which transports water and minerals from the roots to the leaves; the *phloem*, which carries photosynthetic products to growing organs; the *cambium*, which enables secondary growth in thickness in woody plants; and the *parenchyma*, which stores nutrients and contributes to gas exchange [33].

2.2.1.3 The Leaf

The leaf is an aerial organ of the plant that grows laterally from the stem at the nodes where it is attached. Its development begins in the meristem, a growth zone located at the tip of the stem [37, 38]. The position, orientation, and shape of leaves are regulated by hormones, proteins, and genes [37, 38, 39, 40]. A leaf has an upper side, called the *ventral surface*, and a lower side, known as the *dorsal surface*. Its flat shape maximizes sunlight capture to support photosynthesis [41]. In this process, the leaf functions as a true laboratory, where raw sap is transformed into elaborated sap through gas exchange with the surrounding environment [42].

A leaf typically consists of two main parts: the *blade* and the *petiole*. The blade is the flat part responsible for most of the plant's essential functions. It is green in color and covered with stomata, which play a key role in regulating water loss. Veins cross the blade, and its edge is known as the margin. The petiole has a cylindrical shape, sometimes slightly flattened, and connects the blade to the stem. In some species, the petiole is absent; in this case, the leaf is described as *sessile* [43].

Stipules usually appear in pairs where the petiole attaches to the stem or at the node, and they are particularly well developed in plants of the rose and legume families. The veins, including the main central vein, extend through the blade. All these components are illustrated in Figure 2.1b.

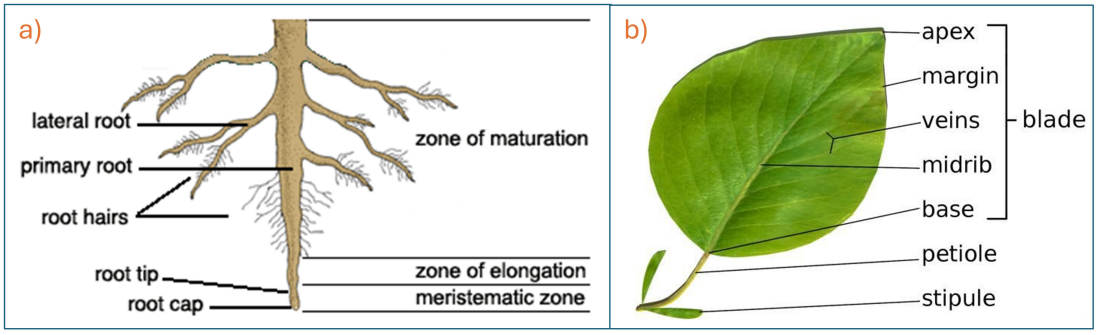

Figure 2.1: (a) Root structure; (b) Leaf structure.

Plants can be classified based on their photosynthetic pathway and vascular structure. With respect to photosynthesis, there are three main types: C3 plants (e.g., wheat and rice), C4 plants (e.g., corn, maize, and sugarcane), and CAM plants (e.g., cacti and pineapples), each adapted to different climatic conditions. Structurally, plants are divided into vascular plants (with roots and stems, such as ferns, conifers, and flowering plants) and non-vascular plants (such as mosses). Some species exhibit specialized adaptations, including carnivorous plants (e.g., *Dionaea*), parasitic plants (e.g., mistletoe), and aquatic plants (e.g., water lilies) [44, 45, 46].

Although this classification provides a general biological framework, the experimental investigations presented in this thesis focus on vascular, broad-leaf plants belonging to specific photosynthetic categories, selected as representative case studies rather than as an exhaustive coverage of all plant types.

The differences in leaf shape between C3, C4, and CAM plants are shown in Figure 2.2.

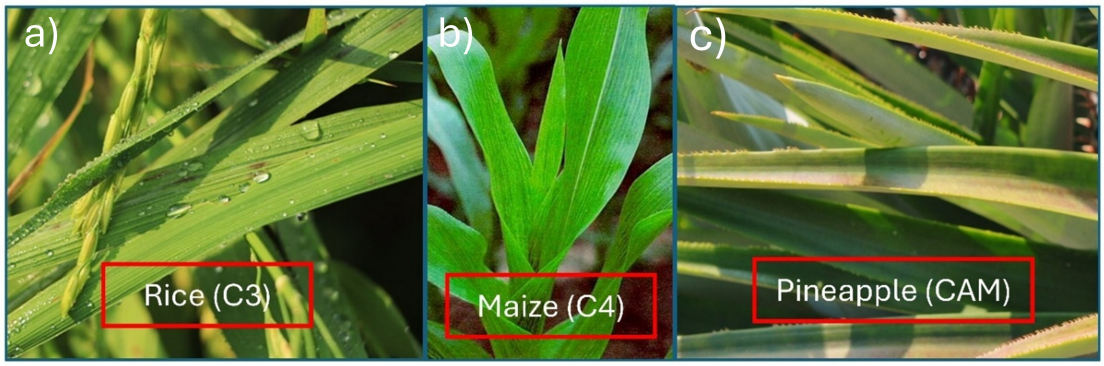

Figure 2.2: Examples of leaf morphology in plants with different photosynthetic pathways: (a) Rice (C3); (b) Maize (C4), and (c) Pineapple (CAM).

2.2.2 Leaf Anatomy

Despite differences in photosynthetic pathways, all leaves share a similar basic anatomy [47, 48, 49, 50, 51]. As illustrated in Figure 2.3, both C3 and C4 leaves have an outer epidermis covered by a waxy cuticle, which helps reduce water loss. Beneath the epidermis are the mesophyll cells, where photosynthesis occurs, and the vascular bundles, which transport water, nutrients, and photosynthetic products. Stomata, mainly located on the lower surface, enable gas exchange (absorption of CO_2 and release of O_2) and facilitate transpiration.

C3 leaves typically have a homogeneous arrangement of mesophyll cells, as

shown in Figure 2.3a. In contrast, C4 leaves contain additional bundle sheath cells surrounding the vascular tissue, as demonstrated in Figure 2.3b, improving the efficiency of carbon fixation in high-light and low-CO_2 environments. CAM plants (not shown) are also adapted to arid conditions, storing water and fixing CO_2 during the night to conserve moisture.

Since leaves are rich in water and play a central role in transpiration and gas exchange, monitoring their hydration provides valuable and direct information about plant water status and overall physiological condition. While plant water status can also be assessed through other indicators, leaf-based measurements offer the advantage of directly reflecting the plant's physiological response to environmental and irrigation conditions. Various techniques are available to measure leaf water status, which will be discussed in the following sections.

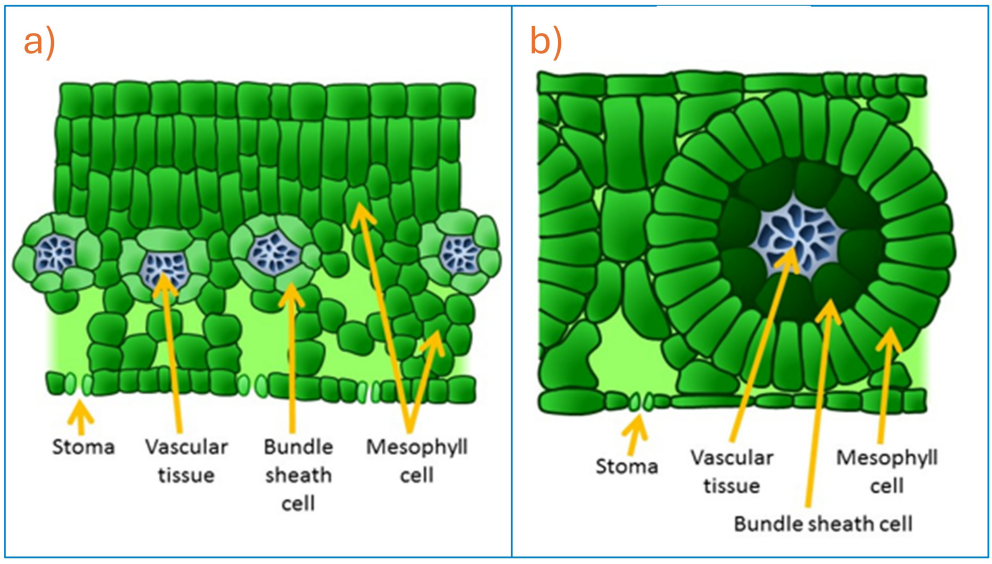

Figure 2.3: Anatomical differences between (a) C3 and (b) C4 type leaves.

Stomata are generally formed by two sclerenchyma-type cells known as *guard cells*. These cells have very thick cell walls [52, 49],which restrict uniform expansion. When guard cells absorb water and increase their turgor pressure, they curve outward, creating the stomatal opening [50] as shown in Figure 2.4a.

Stomatal movement is governed by a well-established osmotic mechanism driven by changes in ion concentrations within guard cells, although the complete regulatory signaling pathways are still under investigation [51].

During daylight hours or under conditions of high humidity, when CO_2 is required for photosynthesis and water loss is less critical, guard cells actively accumu-

late potassium and other ions. This ion uptake promotes water influx by osmosis into the guard cells, primarily into their vacuoles, increasing turgor pressure and resulting in stomatal opening.

Under water-stress conditions, overall photosynthesis decreases due to reduced leaf area and lower photosynthetic activity per unit leaf area. In such conditions, roots release the hormone *abscisic acid* (ABA), which binds to receptors on guard cell membranes, triggering ion efflux [52]. As ions exit the cytoplasm, water flows out of the guard cells by osmosis, the vacuoles shrink, turgor pressure decreases, and the cells become flaccid, leading to stomatal closure [51], as illustrated in Figure 2.4b.

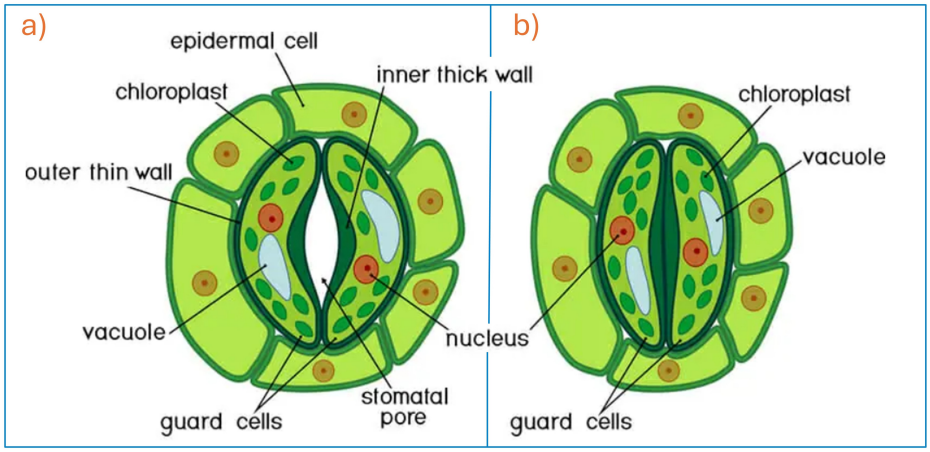

Figure 2.4: Stomatal structure in two states: (a) open and (b) closed. Guard cells control the pore opening to regulate gas exchange and water loss.

2.2.3 Water Movement Through the Plant (Water Potential Theory)

Water transport in higher plants occurs along a continuous pathway extending from the soil, through the roots and vascular tissues, to the leaves and ultimately to the atmosphere. This pathway is commonly referred to as the soil–plant–atmosphere continuum (SPAC). Within this system, water movement is driven by gradients in *water potential* (ψ_w), a thermodynamic quantity that describes the free energy status of water relative to a reference state. Water naturally moves from regions of higher (less negative) water potential to regions of lower (more negative) water potential, enabling its upward transport against gravity.

Plants maintain water under tension within the xylem as a consequence of tran-

spiration. When water evaporates from the leaf surface through the stomata, it generates a negative pressure (suction force) that is transmitted downward through the xylem vessels. This mechanism, often described by the cohesion–tension theory, allows the plant to sustain a continuous flow of water from the roots to the leaves [53].

The circulation of water within the plant is therefore governed by the total water potential (ψ_w), which integrates several distinct physical components. These components represent different forces acting on water in the soil and plant tissues, and their relative contribution varies along the SPAC. According to the classical formulation proposed by Papendick and Campbell [54] and Cowan [55], the total water potential can be expressed as the sum of its individual components, as shown in Equation 2.1.

$$\psi_w = \psi_m + \psi_s + \psi_p + \psi_g \tag{2.1}$$

where ψ_m is the matrix potential, associated with capillary and adsorptive forces; ψ_s is the osmotic potential, related to solute concentration; ψ_p is the pressure potential, reflecting hydrostatic or turgor pressure; and ψ_g is the gravitational potential, accounting for height differences within the plant.

The matrix potential can be expressed by Equation 2.2.

$$\psi_m \text{ (MPa)} = -\frac{2\,\gamma\,\cos\theta}{r\,\rho_w} \tag{2.2}$$

where γ is the surface tension of water (generally 0.0728 N/m at 20°C), θ is the water/soil contact angle (0° for hydrophilic soils), r is the soil pore radius (m), and ρ_w is the density of water (1000 kg/m^3).

In soil, ψ_m is always negative, dominates, and reflects capillary retention forces, while the osmotic potential (ψ_s) becomes significant in saline soils. It can be formalized in Equation 2.3.

$$\psi_s \text{ (MPa)} = -i\,C\,R\,T \tag{2.3}$$

where i is the *van't Hoff* coefficient (equal to 1 in the case of non-dissociation), C is the molar concentration (mol/m^3), R the gas constant (8.314 J/mol/K), and T the absolute temperature (K).

Water is absorbed by the roots when the ψ_w of the soil is higher than that of the roots, then transported via the xylem where the pressure potential (ψ_p) becomes negative under the effect of the tension created by transpiration. In leaves, the water potential is determined by cell turgor, equal to the sum of ψ_s and ψ_p. A drop in this potential (for example, during drought) triggers stomatal closure to

limit water loss. The leaf water potential (ψ_{Leaf}) can therefore be expressed by Equation 2.4.

$$\psi_{\text{Leaf}}\ (\text{MPa}) \approx (-i\,C\,R\,T) + (P - P_{\text{atm}}) \tag{2.4}$$

where P and P_{atm} represent hydrostatic and atmospheric pressure, respectively.

Because fruits are the richest source of water in the plant [56], during the fruiting stage less water is allocated to the leaves, reducing water consumption, particularly in treatments where water is limited [57].

The soil water potential integrates ψ_m, ψ_s, and ψ_g; its reduction decreases water availability for the plant. The gravitational potential is given by Equation 2.5.

$$\psi_g = \rho_w\, g\, h \tag{2.5}$$

where g is gravitational acceleration (9.81 m/s^2) and h is the height of the water column (m).

These water transport mechanisms are illustrated in Figure 2.5, which shows a comparison between well-watered and poorly-watered plants within the soil-plant-atmosphere continuum. The diagram highlights the typical values of water potential components (Ψ_w) across different compartments (symplast and apoplast/xylem). When water potential becomes too low, it restricts water flow to the shoots and leaves, resulting in visible wilting and a reduction in crop yield.

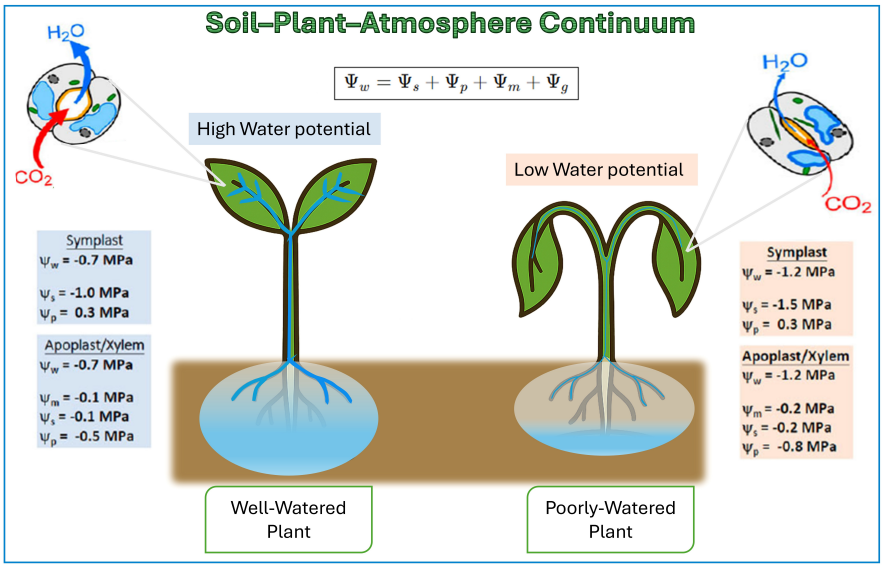

Figure 2.5: The diagram shows differences in water potential (Ψ_w) components across the symplast and apoplast/xylem pathways for a well-watered versus poorly-watered plant.

2.2.4 Responses to Water Stress

Plants are remarkably resilient in the face of water stress. They activate various natural defense mechanisms, including physiological adjustments and molecular responses, to protect themselves. One key strategy is the closure of stomata, which reduces water loss through transpiration. This response is regulated by the stress hormone *abscisic acid* (ABA), which accumulates in the plant when the roots detect low soil moisture [58, 52]. By conserving water in this way, plants can preserve cellular integrity and better withstand drought conditions.

Plants also respond to water stress by altering the angle of their leaves [59], stomatal conductance, and hydraulic conductance [60, 61, 62, 63, 64, 65, 66, 2, 4, 67, 68, 69]. Over time, they maintain a relatively stable water status by adjusting the rates of leaf expansion and root growth [32, 70].

On a macroscopic scale, these disturbances manifest in visible symptoms such as leaf wilting (due to loss of turgor), curling, or changes in pigmentation (yellowing or reddening associated with chlorophyll degradation or anthocyanin accumulation). These signs, which frequently indicate ongoing stress, reflect both structural damage and adaptive strategies that enhance survival under water shortage.

Water stress has been shown to negatively affect plant growth and productivity [71]. Different indicators of water stress can be used to guide irrigation scheduling in vegetable crops and emphasize the importance of accurate water status monitoring [57]. Measuring plant water status is therefore essential for optimizing irrigation strategies and improving water-use efficiency (WUE). The following sections review the main methods used to assess plant water status.

2.3 Measurements of Plant Water Status

2.3.1 Direct Measurements of the Plant Water Status

2.3.1.1 Water Potential Measurement (ψ_w)

Psychrometer. Psychrometers estimate total water potential (ψ_w) by measuring vapor pressure depression using the Kelvin equation [72, 1]. There are two types of psychrometers: the field version and the laboratory version. Each model has its own characteristics and specifications.

The field model is useful for leaf or *in situ* measurements and generally consists of a ceramic shield or stainless-steel screen covering a fine-wire thermocouple junction, as shown in Figure 2.6a. The "wet" sensor is surrounded by a wick soaked in water. As the water evaporates, the temperature of the sensor drops

because evaporation consumes latent heat. The temperature difference between the two sensors can be used to calculate the relative humidity of the air or the water potential of plant tissue.

The laboratory model is designed for high-precision measurements of soil samples under controlled conditions, as shown in Figure 2.6b. Its operating principle is based on comparing the vapor pressure above pure water (the reference state, where $\psi_w = 0$) with the vapor pressure above water in a soil sample, which is reduced due to matrix forces. This reduction in vapor pressure is related to relative humidity (RH) and water potential through the Kelvin equation [1], as shown in Equation 2.6:

$$\psi_w = \frac{M_w}{RT} \ln\left(\frac{e}{e_0}\right) \tag{2.6}$$

where e is the vapor pressure above soil water, e_0 is the vapor pressure above pure water, R is the ideal gas constant, T is the absolute temperature, and M_w is the molecular weight of water.

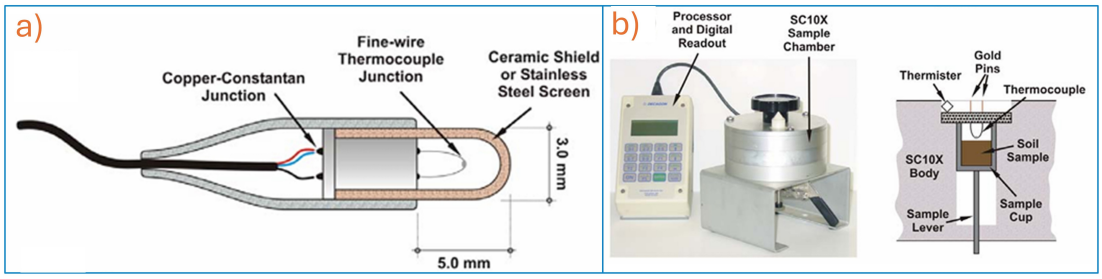

Figure 2.6: Psychrometer models: (a) Field model and (b) Laboratory model [1].

Pressure Chamber. The pressure chamber, also known as the *pressure bomb*, is a widely used instrument for measuring plant water potential [73]. The technique is based on the cohesion–tension theory, in which pressure is applied within the chamber to counterbalance the tension in the xylem, allowing estimation of the water potential. During the measurement, the leaf or shoot is placed inside the chamber while the cut stem remains outside. Pressure is gradually increased until sap appears at the cut surface, indicating equilibrium. This method is rapid, reproducible, and suitable for both field and laboratory use [74, 75].

To obtain reliable readings, environmental conditions such as humidity, temperature, and light should be stabilized before measurement [73]. Studies have shown that plants reach a stable water potential after two days in a humidified chamber and can maintain it for up to seven days, enabling precise investigations

of water stress effects. Moreover, water potential gradients have been observed in transpiring organs such as rose and wheat leaves; these gradients tend to dissipate after equilibration during the night [76]. It should be noted that the pressure chamber measures the highest water potential within the organ, typically in the xylem near the cut surface, rather than providing an average value across all tissues.

Microtensiometer. The microtensiometer is a device employed for measuring plant water potential. It can be placed in the trunk or xylem and operates on the same principle as conventional tensiometers. The sensor comprises a hermetically sealed pressure cell filled with water, connected to a porous membrane in direct contact with the xylem. Under water-stress conditions, water molecules move from the sensor into the plant tissues, inducing a pressure change detected by an integrated pressure transducer, which converts it into a digital water potential value.

As illustrated in Figure 2.7, FloraPulse Systems offers a widely used version of the microtensiometer sensor. A recent study demonstrated its effectiveness for continuous monitoring of stem water potential in fruit crops, identifying it as a reliable alternative to the traditional Scholander pressure chamber [2].

The microchip sensor contains a water volume of 5–10 nL and measures pressure using a piezoresistive transducer embedded in an 8 mm-diameter cylindrical probe. The sensing edge of the chip, which interfaces with xylem water, is exposed at the tip of the device. Tests conducted on apple, almond, and grapevine plants showed strong agreement with pressure chamber readings, although some species-specific differences were observed due to anatomical variations.

The results revealed distinct diurnal patterns, with minimum stem water potential typically occurring around 16:00 h, followed by partial recovery later in the day. This real-time monitoring enables dynamic irrigation scheduling. However, certain limitations were noted in crops like walnut, where high xylem transpiration rates can reduce accuracy. Overall, this technology shows strong potential for advancing precision irrigation, although further refinement is needed for large-scale deployment.

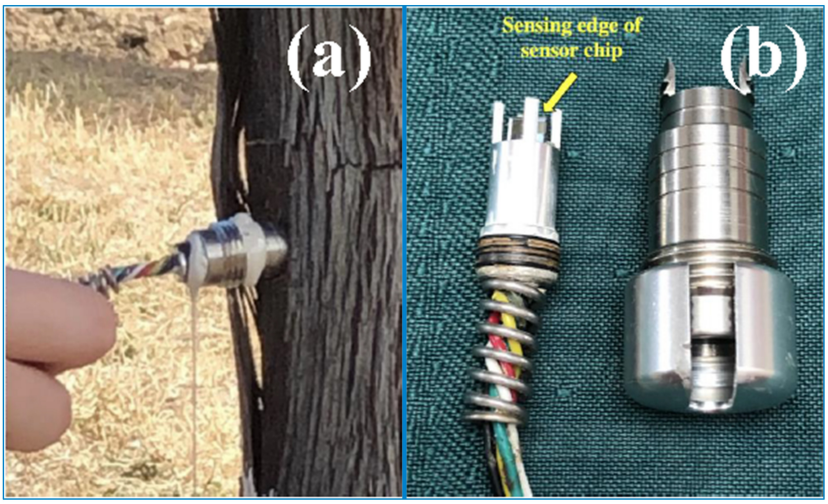

Figure 2.7: (a) Microtensiometer installed on a tree trunk, offered by FloraPulse Systems; (b) Close-up of the microchip sensor showing the exposed sensing edge for xylem contact [2].

2.3.1.2 Osmotic Potential Measurement (ψ_s)

Several methods have been developed to measure ψ_s, among them:

Pressure–Volume (PV) Analysis. This method is based on the relationship between water potential (ψ) and relative water content (RWC) in plant tissue. Details of the RWC method will be described in the following section. In this approach, a leaf is subjected to increasing pressure in a pressure chamber, and the resulting water loss is measured to construct a pressure–volume (PV) curve. By extrapolating the linear portion of the curve, it is possible to determine the osmotic potential (ψ_s) at full turgor and at the turgor-loss point. However, this technique is not well suited for large-scale studies [60, 61].

Expressed Sap (ES) Osmometry. In this method, sap is extracted from plant tissue by centrifugation or mechanical pressure, and its osmolality is measured using an osmometer (either vapor-pressure or freezing-point type). The osmotic potential is then calculated using the Equation 2.7 of Van't Hoff [61].

$$\psi_s = -\frac{n}{V}RT \tag{2.7}$$

where n/V is the osmolality, R is the gas constant, and T is the absolute temperature.

The most commonly used instrument is the vapor-pressure osmometer (VPO) [63], which is suitable for small samples, such as thawed leaf discs or expressed sap. It operates based on the Peltier effect, cooling the sample to induce condensation, and then measures the equilibrium vapor pressure, which is proportional to solute concentration [63, 62, 64]. This method is rapid and efficient, requiring only a few minutes per sample, and is applicable to a wide variety of plant tissues.

2.3.1.3 Leaf Turgor Pressure Sensors

Leaf turgor pressure sensors are used to monitor plant water stress by detecting relative changes in turgor pressure within the leaf tissue [77]. Turgor pressure reflects the balance between water uptake by the roots, water loss through transpiration, and the osmotic pressure inside cells [78, 79].

A prominent example is the non-invasive *leaf patch clamp pressure probe* (ZIM-Probe) [80], which allows real-time monitoring of subtle fluctuations in leaf turgor pressure. The ZIM-Probe consists of two opposing magnetic pads (stamps): one includes a sensitive pressure sensor connected to a ZIM-transmitter and telemetry unit, while the other applies a constant magnetic force via a threaded mechanism to ensure reliable contact with the leaf [80, 3]. Its working principle is illustrated in Figure 2.8.

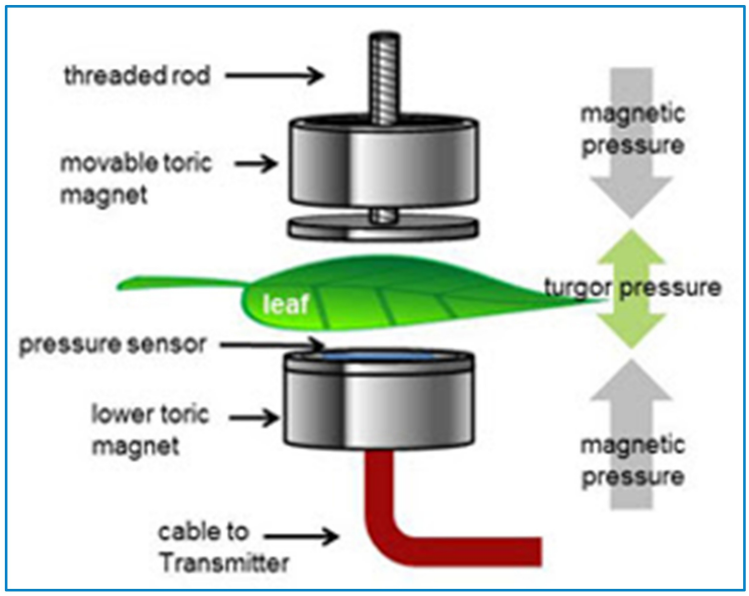

Figure 2.8: Working principle of the ZIM-Probe. Magnetic pads apply pressure on the leaf, and a pressure sensor records turgor variations, which are transmitted in real-time [3].

2.3.1.4 Relative Water Content Measurement

The relative water content (RWC) of a plant provides a quantitative measure of the leaf's water status relative to its maximum water-holding capacity. It reflects both water potential and cellular osmotic adjustment [81, 82, 83, 84]. A drop in RWC below 80% is typically associated with a decrease in water potential to around –1.5 MPa [85].

This method is simple, low-cost, and does not require specialized instruments, although it can be time-consuming [86]. RWC values are influenced by species-specific traits (e.g., isohydric vs. anisohydric behavior), soil conditions, and environmental factors. As a result, RWC alone cannot always identify the underlying cause of water stress and may not be a universal indicator. However, in anisohydric crop species, RWC can provide a relatively accurate estimation of water stress under varying soil moisture levels when environmental conditions are stable [57].

2.3.2 Indirect Measurements of the Plant Water Status

2.3.2.1 Stomatal Conductance and Transpiration Rate as Indicators of Plant Water Stress

Stomatal conductance and transpiration rate are complementary parameters that provide valuable insights into how plants respond to environmental conditions and water availability. Stomatal conductance regulates both the entry of carbon dioxide for photosynthesis and the exit of water vapor through the stomata.

As discussed in subsection 2.2.2, when water levels in the plant are high, stomata remain open, facilitating enhanced gas exchange and higher transpiration rates. Conversely, under water-stress conditions, stomata partially or completely close to minimize water losses, resulting in reduced transpiration. Consequently, stomatal conductance is a crucial variable for evaluating gas exchange through leaf stomata, particularly regarding carbon dioxide uptake and water loss through transpiration.

This parameter is determined using portable porometers [87], which allow rapid assessment under field conditions, particularly in irrigation trials. A range of instruments is available to measure conductance as a function of the moisture gradient inside a closed chamber. Examples include steady-state porometers (e.g., Decagon SC-1, PP Systems PMR-5) [4], dynamic diffusion porometers (e.g., Delta-T AP4) [67], viscous or mass-flow systems (e.g., Thermoline) [68], and zero-equilibrium porometers (e.g., LICOR LI-1600) [69].

As shown in Figure 2.9, the Decagon SC-1 instrument is illustrated during operation, displaying the result of a measurement.

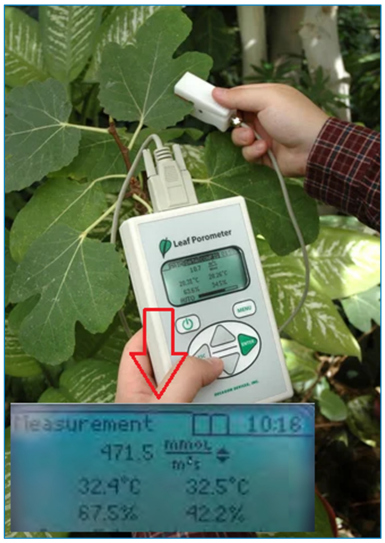

Figure 2.9: The Decagon SC-1 instrument [4].

For optimal reliability, measurements should be taken on fully developed, clean leaves exposed to sufficient sunlight, ideally between 11:00 a.m. and 2:00 p.m. Typical stomatal conductance values under irrigated conditions range between 300 and 700 mmol m^{-2} s^{-1}, whereas under moderate water stress they range between 80 and 300 mmol m^{-2} s^{-1}. These values can also indirectly estimate transpiration rates, as high conductance is generally associated with increased transpiration and improved canopy thermal regulation [4].

Recently, researchers at the Massachusetts Institute of Technology (MIT) have developed an innovative sensor that leverages the natural function of stomata-microscopic pores on leaf surfaces responsible for water evaporation and gas exchange. This sensor is fabricated by printing a carbon-nanotube-based conductive ink directly onto the leaf surface, enabling real-time monitoring of stomatal dynamics [88, 89].

The sensor is placed directly over a stoma. When the stoma is closed, the conductive path is complete, allowing current to flow. When the stoma opens, the circuit is broken, interrupting the current. By tracking these current fluctuations using a simple multimeter, stomatal behavior can be monitored in real time [5]. The sensor design and application are illustrated in Figure 2.10.

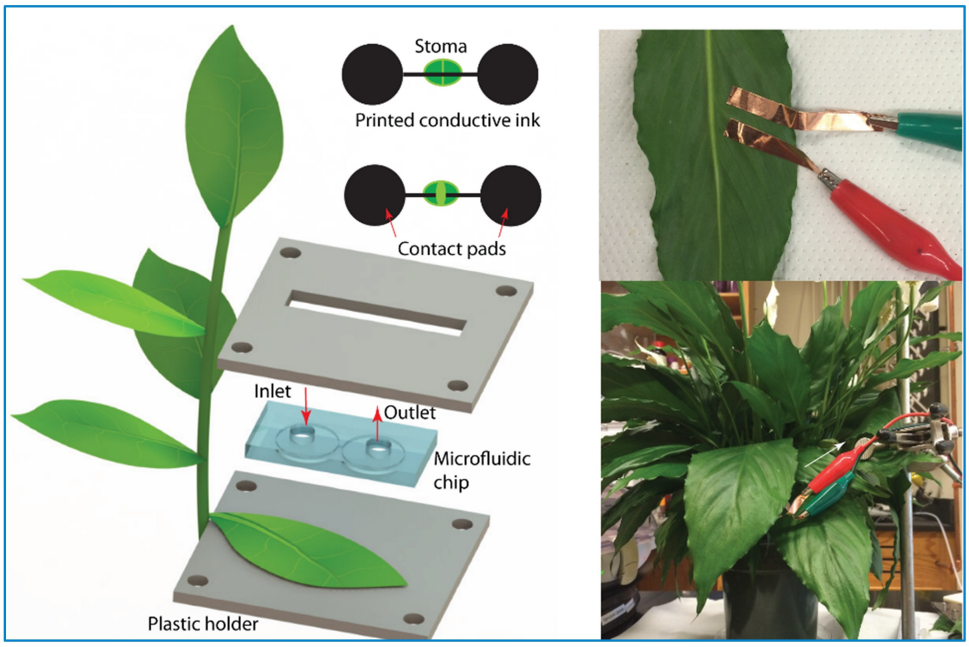

Figure 2.10: Sensor system developed at MIT for monitoring stomatal behavior. The printed carbon-nanotube ink forms a circuit that opens and closes in response to stomatal movement [5].

2.3.2.2 Canopy Temperature as an Indicator of Plant Water Stress

Canopy temperature plays a critical role in plant metabolic activity and is primarily regulated by transpiration. Through evaporation from leaf surfaces, transpiration removes latent heat and cools the plant canopy [90, 91]. Under water-stress conditions, reduced soil moisture leads to decreased transpiration, resulting in elevated leaf and canopy temperatures.

Because of this, canopy temperature is closely correlated with plant water status and serves as a sensitive indicator for detecting water stress. To quantify this relationship, the *Crop Water Stress Index* (CWSI) was introduced, based on the temperature difference between canopy and air ($T_c - T_a$) and the vapor pressure deficit (VPD).

CWSI is defined between two baselines:

- a lower baseline $(T_c - T_a)_{LL}$, representing a well-watered plant with maximum transpiration (no stress), and
- an upper baseline $(T_c - T_a)_{UL}$, corresponding to a non-transpiring plant under maximum stress.

The empirical formula for CWSI, as proposed by Idso *et al.* [81], is given by Equation 2.8:

$$\text{CWSI} = \frac{(T_c - T_a) - (T_c - T_a)_{LL}}{(T_c - T_a)_{UL} - (T_c - T_a)_{LL}} \tag{2.8}$$

where T_c is the canopy temperature and T_a is the ambient air temperature.

To measure leaf or canopy temperature, two types of instruments are commonly used: infrared thermometers and thermal cameras [6, 92]. A comparison of these approaches was carried out using a FLIR T335 thermal camera (for infrared thermography) and an AG-42 handheld infrared thermometer (Telatemp), as shown in Figure 2.11.

Measurements performed on two wheat varieties subjected to drought, salinity, and combined stress revealed strong correlations between canopy temperature and leaf water potential, particularly under severe stress conditions. Temperature differences of up to 9 °C were observed between treatments. Both infrared thermography and thermometry effectively distinguished stress levels and cultivar tolerance.

However, thermography provides additional advantages, such as image-based visualization of spatial thermal variations across the plant. This allows for more precise assessment by excluding soil interference and enabling whole-canopy temperature mapping, particularly valuable when plant coverage is sparse.

Figure 2.11: (a) AG-42 handheld infrared thermometer (Telatemp), and (b) FLIR T335 thermal camera used for canopy temperature measurements [6].

2.3.2.3 Sap Flow as an Indicator of Plant Water Stress

Sap flow measurement provides an important plant-based approach to quantifying water stress [92]. Sap, the water transported through xylem tracheary elements, reflects the transpiration stream. Since water stress reduces transpiration via stomatal closure, sap flow decreases accordingly, making it a valuable indicator of plant water status [93].

Technological advances, such as heat-pulse thermal sensors, have enabled accurate sap flow measurements in plant stems, providing a useful tool for irrigation scheduling [94, 95]. However, interpreting sap flow data requires caution, as it is influenced by both internal and external factors. Internal factors include root and stem hydraulic conductivity, canopy structure, and stomatal regulation, while external factors include soil moisture, solar radiation, air temperature, and vapor pressure deficit (VPD).

Sap flow typically shows a positive linear correlation with solar radiation, VPD, and temperature, with solar radiation being the dominant driver. Under varying environmental and soil conditions, it can be difficult to determine whether a decline in sap flow is due to reduced soil water availability or increased atmospheric evaporative demand [96].

As a result, uncalibrated use of sap flow data for irrigation control can lead to under- or over-irrigation. Effective irrigation scheduling based on sap flow requires species-specific calibration and appropriate threshold values [93, 94, 97, 96]. Despite these challenges, the automatic recording capability of sap flow sensors makes this method promising for integration into automated irrigation systems, provided that accurate crop-specific thresholds are established.

2.3.2.4 Leaf Thickness as an Indicator of Plant Water Stress

Leaf thickness sensors have emerged as promising tools for monitoring plant water status, offering non-destructive and continuous measurement capabilities. These sensors operate on the principle that leaf thickness varies with water content decreasing during dehydration and increasing with rehydration [7, 98].

The relationship between leaf thickness and water status is typically expressed through relative water content (RWC). Studies have shown a distinct breakpoint in the RWC–thickness curve, corresponding to the turgor-loss point (TLP), which is a critical threshold for detecting water stress [7]. Modern magnetic-field-based thickness sensors offer high precision (up to 1 µm) and can be automated for real-time monitoring, making them suitable for irrigation scheduling and drought research. The sensing principle is illustrated in Figure 2.12.

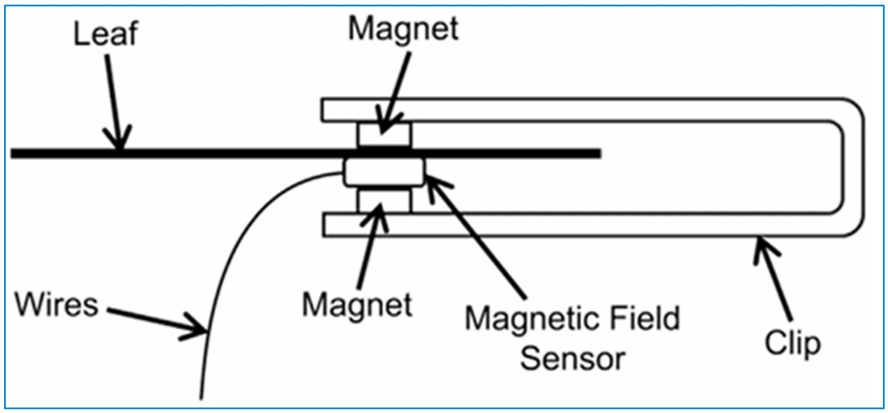

Figure 2.12: Leaf-thickness sensor composition [7].

However, the relationship between thickness and water status is species-specific and influenced by anatomical characteristics, leaf position, and environmental factors, requiring calibrated models for accurate interpretation [7, 98]. For example, drought-tolerant species such as sorghum exhibit larger thickness breakpoints than sensitive species like fava bean, reflecting differences in cell wall rigidity and osmotic adjustment [7]. Despite their potential, challenges such as diurnal fluctuations and environmental noise must be addressed for reliable field deployment. Integrating leaf thickness data with other physiological indicators, such as water potential and stomatal conductance, can improve the overall accuracy of water status assessments [98].

2.3.2.5 Stem Diameter Variation as an Indicator of Plant Water Stress

Monitoring stem-diameter variation (SDV) has emerged as an effective approach for assessing plant water status, particularly in vegetable crops. SDV reflects the dynamic exchange of water between xylem and phloem tissues. Early in the morning, root water uptake may be insufficient to meet the increasing atmospheric demand caused by rising solar radiation, resulting in xylem tension and the mobilization of stored phloem water to sustain transpiration. At night, phloem tissues are rehydrated [99, 100].

These diurnal shrinkage–expansion cycles correspond to variations in xylem water potential [99, 100]. Under water-stress conditions, greater daily stem shrinkage is typically observed, which may eventually restrict stem growth [101]. Consequently, SDV serves as a sensitive indicator of plant water availability.

Several indices have been developed to quantify SDV, including the *Stem Growth Rate* (SGR), *Maximum Daily Stem Shrinkage* (MDS), *Minimum Stem*

Diameter (MNSD), and *Maximum Stem Diameter* (MXSD). Among these, SGR and MDS are the most widely used in research [101, 94, 102].

Despite its high sensitivity, applying SDV indices for automated irrigation scheduling remains challenging. Nonetheless, SDV is a valuable tool for detecting early signs of water stress and enhancing the understanding of plant-water interactions.

2.4 Advanced Measurement Methods

2.4.1 Electrical Impedance Spectroscopy Method

Electrical impedance can provide a non-destructive, real-time assessment of leaf water status [103]. Impedance reflects electrical properties linked to cell structure and water content. Under water stress, reduced water content generally increases tissue impedance, particularly at low frequencies [104, 105, 106, 107].

Definitions. Impedance Z is the ratio of applied voltage $V(t)$ to resulting current $I(t)$, as shown in Equation 2.9

$$Z = \frac{V(t)}{I(t)}. \tag{2.9}$$

For AC analysis with sinusoidal excitation, the voltage and current signals are represented in Equation 2.10 and Equation 2.11, respectively.

$$V(t) = V_0 \sin(\omega t), \tag{2.10}$$

$$I(t) = I_0 \sin(\omega t + \phi), \tag{2.11}$$

where V_0 and I_0 are the voltage and current amplitudes, respectively, $\omega = 2\pi f$ is the angular frequency (with f being the frequency in hertz), and ϕ is the phase shift between the voltage and current signals.

In complex notation, the frequency-dependent impedance is represented in Equation 2.12.

$$Z(\omega) = \frac{V_0}{I_0} e^{j\phi} = |Z| e^{j\phi}, \tag{2.12}$$

and the rectangular form is represented in Equation 2.13.

$$Z = R + jX, \tag{2.13}$$

where R is the resistance (dissipative part) and X is the reactance (energy-storage part).

For ideal reactive elements, the reactances are defined in Equation 2.14.

$$X_C = -\frac{1}{\omega C}, \qquad X_L = \omega L, \tag{2.14}$$

where X_C and X_L represent the capacitive and inductive reactances, respectively, $\omega = 2\pi f$ is the angular frequency, C is the capacitance, and L is the inductance.

Evidence from controlled studies. In a study on *Labisia pumila* subjected to evapotranspiration (ET) replacement levels of 100%, 75%, 50%, and 25%, leaf impedance increased with water stress [107]. ECG-type electrodes were attached to leaves and connected to a precision impedance converter/network analyzer. Frequencies were set via a software interface. At higher frequencies (70–100 kHz), impedance showed improved stability and better separation among stress levels. By week 20, plants at 25% ET replacement had the highest impedance (up to ~ 150 kΩ), consistent with reduced leaf water content. Impedance correlated with standard leaf water status metrics, including leaf water potential and relative water content (RWC), with a coefficient of determination $R^2 \approx 0.78$.

Similarly, in canola, EIS achieved near-perfect correlation with RWC where the coefficient of determination is $R^2 \approx 0.99$ and a root mean square error of $\sim 0.30\%$ [108]. These findings suggest impedance-based sensing as a cost-effective, real-time alternative to conventional measurements suitable for precision irrigation. However, most results to date come from laboratory or greenhouse conditions; in open-field settings, environmental variability and soil heterogeneity can reduce stability and require additional calibration [108, 107].

Single- vs. multiple-frequency measurements. Single-frequency impedance has been used in plant studies to probe specific physiological conditions by measuring at a fixed frequency (typically ∼1–100 kHz) [109]. It enables rapid screening of plant water status or detection of cellular damage, since changes in extracellular resistance correlate with tissue hydration and membrane integrity [110]. Single-frequency readings are also sensitive to environmental stresses (e.g., drought, frost) that alter membrane permeability, causing measurable impedance changes [8]. However, a single frequency provides limited insight into the distribution of electrical pathways and cannot clearly separate contributions from different cellular compartments [111].

Measuring impedance over a range of frequencies (*impedance spectroscopy*) reveals key physiological and structural features [109, 111]. At low frequencies (below

$\sim$ 1 kHz) the capacitive cell membranes confine current mostly to the extracellular space; as frequency increases, membranes are progressively bypassed and current penetrates cells. Above $\sim$ 100 kHz the response increasingly reflects intracellular properties [112, 113].

From a physiological perspective, the frequency dependence of impedance measurements is particularly relevant for assessing leaf water status. Low-frequency responses are dominated by extracellular pathways and membrane polarization effects, which are sensitive to changes in apoplastic hydration. At higher frequencies, the reduced influence of cell membranes allows current to probe intracellular compartments, whose electrical properties are affected by cytoplasmic conductivity and vacuolar water content. As a result, multi-frequency impedance measurements provide a means to separate and interpret hydration-related changes occurring in different tissue compartments, forming the basis for the equivalent circuit models introduced in the following sections.

Two-terminal (2T) The two-electrode (2T) configuration is the simplest setup in impedance spectroscopy, but it is affected by electrode polarization, particularly at low frequencies [114]. In plant tissues, 2T measurements include both the tissue impedance and the electrode–tissue interface impedance, the latter often dominating at low frequencies [115].

To mitigate this effect, higher excitation frequencies (typically above 1 kHz) and surface treatments are commonly used to reduce polarization [116]. Despite its limitations, the 2T configuration remains useful for rapid measurements or when electrode placement is restricted, such as in small organs or delicate tissues [117]. The configuration is illustrated in Figure 2.13a.

Four-terminal (4T) configuration. For more precise measurements, the four-electrode (4T) configuration, also known as *the Kelvin method*, is preferred, as it separates current injection from voltage sensing, thereby minimizing the influence of contact impedance [110, 118].

In plant studies, the 4T setup provides more reliable and accurate data, especially at low frequencies where cellular properties dominate the impedance response [119]. This configuration is particularly useful for monitoring rapid physiological responses, such as those triggered by cold shock or mechanical stimuli, through time-resolved measurements [8]. The configuration is illustrated in Figure 2.13b.

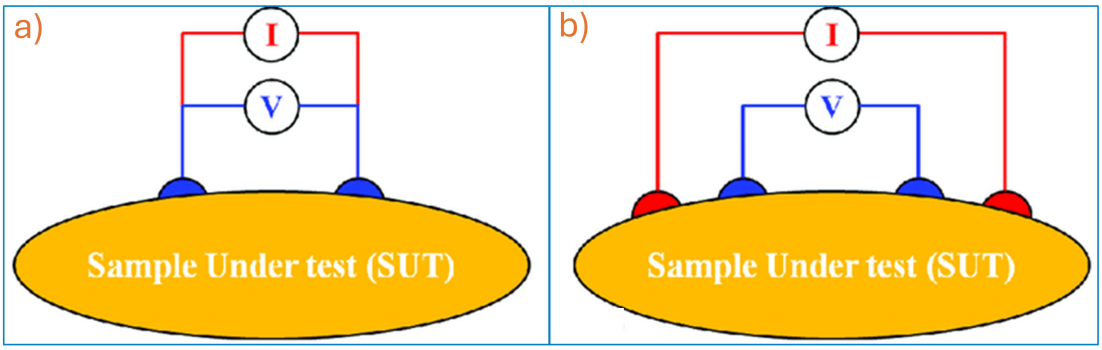

Figure 2.13: (a) Two-electrode; (b) four-electrode impedance configurations [8].

2.4.1.1 Electrical Modelling Components

Cole model. The Cole model is widely used in plant studies to analyze tissue impedance spectra by representing the electrical response of biological tissues in a compact frequency-domain formulation [120, 121]. In its simplest physical interpretation, plant tissue can be described as a parallel combination of an extracellular resistance (R_1), an intracellular resistance (R_2), and a membrane capacitance (C). This representation captures the dominant conduction pathways and membrane polarization effects. However, its simplicity is also a limitation: highly structured tissues with pronounced subcellular compartments may require more complex models [122].

The frequency-dependent impedance of the Cole (or Cole–Cole) model is described by Equation 2.15.

$$Z(\omega) = R_\infty + \frac{R_0 - R_\infty}{1 + (j\omega\tau)^\alpha}, \tag{2.15}$$

where R_0 is the low-frequency (DC) resistance and R_∞ is the high-frequency resistance. These parameters represent the asymptotic impedance limits of the tissue and can be directly related to the lumped electrical elements of the equivalent circuit. Specifically, in the ideal case ($\alpha = 1$), the Cole model is mathematically equivalent to a parallel RC circuit, for which

$$R_0 = R_1 + R_2, \qquad R_\infty = R_1, \qquad \tau = R_2\, C. \tag{2.16}$$

Accordingly, the resistance difference ($R_0 - R_\infty$) corresponds to the intracellular contribution, while R_∞ reflects predominantly extracellular conduction. The relaxation time constant τ characterizes the membrane charging process and depends on both the intracellular resistance and the membrane capacitance. The

parameter α (with $0 < \alpha \leq 1$) accounts for dielectric dispersion and tissue heterogeneity; when $\alpha < 1$, the impedance response deviates from ideal Debye-type behavior and should be interpreted phenomenologically rather than as a strict lumped-element circuit. Here, $j = \sqrt{-1}$ is the imaginary unit and $\omega = 2\pi f$ is the angular frequency.

To better model the depressed semicircles commonly observed in Nyquist plots of biological tissues, the ideal capacitor is often replaced by a constant phase element (CPE). The impedance of the CPE is given by Equation 2.17:

$$Z_{\mathrm{CPE}} = \frac{1}{C(j\omega)^n}, \qquad 0 < n \leq 1, \tag{2.17}$$

which reduces to the impedance of an ideal capacitor when $n = 1$.

A schematic diagram of the equivalent circuit for the Cole model, including the optional CPE, is shown in Figure 2.14.

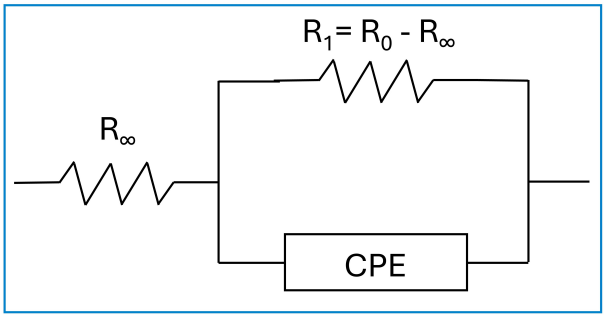

Figure 2.14: Schematic equivalent circuit for the Cole model (with optional CPE).

Hayden model. The Hayden model represents plant tissue as a network of multiple resistive pathways combined with a membrane capacitive element [9, 123]. In this model, resistances R_1, R_2, and R_3 correspond to different apoplastic and symplastic conduction paths, while the capacitor C models the membrane's dielectric behavior. In many practical cases, $R_3 \gg R_1, R_2$, allowing for a simplified circuit in which R_3 is omitted. The full and simplified configurations are illustrated in Figure 2.15.

These equivalent circuits have been widely used to interpret tissue electrical responses under abiotic stresses such as frost and salinity, offering a way to link electrical parameters with physiological status.

A more compact formulation, known as the *improved Hayden model*, treats the extracellular (apoplastic) resistance R_a, the intracellular (symplastic) resistance

R_s, and the membrane impedance Z_m as parallel components. The impedance of this model is described by Equation 2.18.

$$Z(\omega) = \left(\frac{1}{R_a} + \frac{1}{R_s} + \frac{1}{Z_m(\omega)} \right)^{-1}. \tag{2.18}$$

To account for membrane dispersion, the membrane impedance Z_m is often expressed with a fixed phase angle φ as shwon in Equation 2.19.

$$Z_m(\omega) = \frac{e^{j\varphi}}{C_m\,\omega} = \frac{\cos\varphi + j\,\sin\varphi}{C_m\,\omega}, \tag{2.19}$$

where C_m is the effective membrane capacitance and $\omega = 2\pi f$ is the angular frequency.

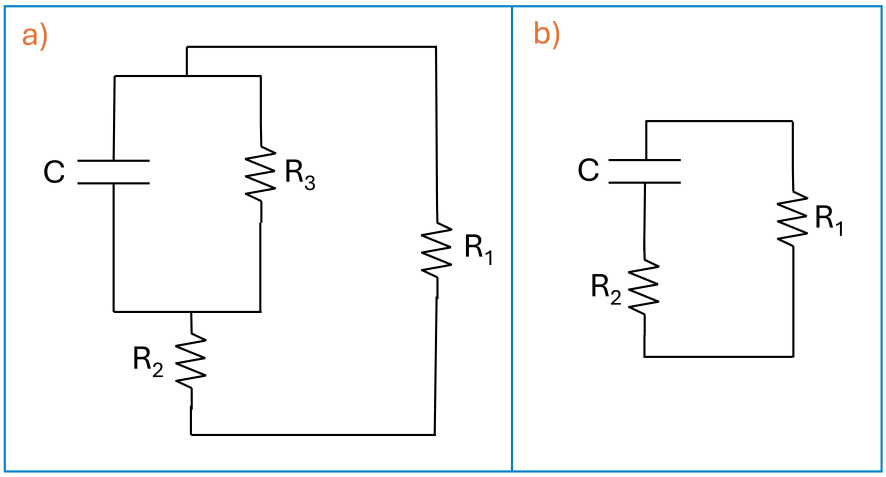

Figure 2.15: (a) Full Hayden model with multiple resistive paths and a membrane capacitor; (b) simplified Hayden model when $R_3 \gg R_1, R_2$ [9].

Double-Shell model. A recent study applied non-invasive bioimpedance spectroscopy (BIS) measurements to assess plant water stress using gold electrodes over a frequency range of 1 Hz to 100 kHz [124]. The bioimpedance data were acquired using standard electrode configurations, consistent with the measurement principles described earlier and illustrated in Figure 2.13. The novelty of the approach lies in the interpretation of the measured impedance spectra through the double-shell electrical model, rather than in a different experimental acquisition method.

Within this framework, the extracellular resistance (R_1) exhibited a linear relationship with water loss, making it a reliable indicator of water stress. Particle swarm optimization (PSO) was employed to estimate the model parameters, providing more stable and physiologically meaningful fits than conventional fitting techniques. The optimized parameters correlated strongly with relative water content (RWC) and photosynthetic efficiency, demonstrating the potential of the double-shell model for linking electrical impedance measurements to plant hydration status.

The total impedance of the double-shell model [125] is expressed by Equation 2.20.

$$Z(j\omega) = \frac{R_1\left(\frac{1}{(j\omega)^{\beta}Q_3} + Z_{\text{partial}}\right)}{R_1 + \frac{1}{(j\omega)^{\beta}Q_3} + Z_{\text{partial}}}, \tag{2.20}$$

where the partial branch is given by Equation 2.21.

$$Z_{\text{partial}} = \frac{R_2\left(R_4 + \frac{1}{(j\omega)^{\alpha}Q_5}\right)}{R_2 + R_4 + \frac{1}{(j\omega)^{\alpha}Q_5}}, \tag{2.21}$$

where R_1, R_2, and R_4 represent the extracellular, intracellular, and vacuolar resistances, respectively. The elements Q_3 and Q_5 are constant-phase elements (CPEs) that describe the dispersive properties of the membranes, with the exponents $0 < \alpha, \beta \leq 1$ accounting for dielectric dispersion. The general expression for a CPE is given by Equation 2.17.

Due to the increased number of parameters and the strong nonlinearity of the double-shell model, parameter estimation is typically performed using global optimization strategies rather than simple local or gradient-based fitting methods.

2.4.1.2 Fitting Methodologies

Following the introduction of EIS measurements and equivalent circuit models, this section presents the main strategies used to estimate circuit parameters from experimental impedance spectra.

Levenberg–Marquardt algorithm (LM). The most commonly used approach for model fitting is nonlinear least squares (NLLS), typically implemented using the Levenberg–Marquardt algorithm [126]. NLLS iteratively minimizes the sum

of squared errors between the measured and model-predicted impedance values across frequencies. Once fitted, model parameters such as R, C, and the CPE elements can be tracked over time or hydration states, enabling quantitative and non-invasive monitoring of plant water status, drought progression, and overall plant health [127, 128]. This combination of EIS with NLLS-based fitting, particularly via the LM algorithm, is now widely adopted in both precision agriculture and plant physiological research.

Genetic Algorithms (GA). Genetic algorithms (GAs) provide a global optimization framework for EIS model fitting and are well suited to the nonlinear, multi-parameter nature of equivalent circuit models [127]. By exploring the parameter space through crossover and mutation, GAs reduce sensitivity to local minima and improve initialization for complex fitting problems [129].

Several studies have shown that GA-based EIS fitting effectively tracks hydration-induced impedance changes, such as increases in resistance and decreases in capacitance, which are characteristic of drought stress [127, 129, 130, 128, 131].

Hybrid methods. Hybrid optimization schemes combine genetic algorithms (GA) for global search with nonlinear least squares (NLLS) for local refinement, commonly referred to as *GA+NLLS*, to obtain accurate and physiologically meaningful parameters with enhanced robustness [127]. Such approaches have achieved fitting errors below approximately 5% in plant tissue studies and are particularly attractive for automated pipelines in precision irrigation. However, practical challenges remain in balancing computational cost and accuracy for near real-time field applications [127, 132].

Machine Learning (ML) approaches. Machine learning (ML) can augment or replace explicit circuit fitting by learning direct mappings from impedance spectra to plant hydration metrics. Models such as support vector machines (SVMs) and neural networks can process raw spectra or engineered features (e.g., R_1, C_m, CPE exponents) to predict water status with high accuracy, with reported coefficients of determination of $R^2 = 0.95$ for leaf water content [52, 133]. Although physical interpretability may be limited, integrating ML models with miniaturized EIS hardware and IoT platforms enables real-time, *in situ* monitoring and provides valuable decision support for irrigation management [127, 108].

2.4.2 Infrared Spectroscopy Measurement Methods

Infrared spectroscopy has emerged as a powerful, non-destructive alternative for rapid evaluation of plant water status across several spectral regions: near infrared (NIR: 750–2500 nm), mid-wave infrared (MWIR: 2.5–6 µm), and thermal infrared (TIR: 3–16 µm) [134, 135].

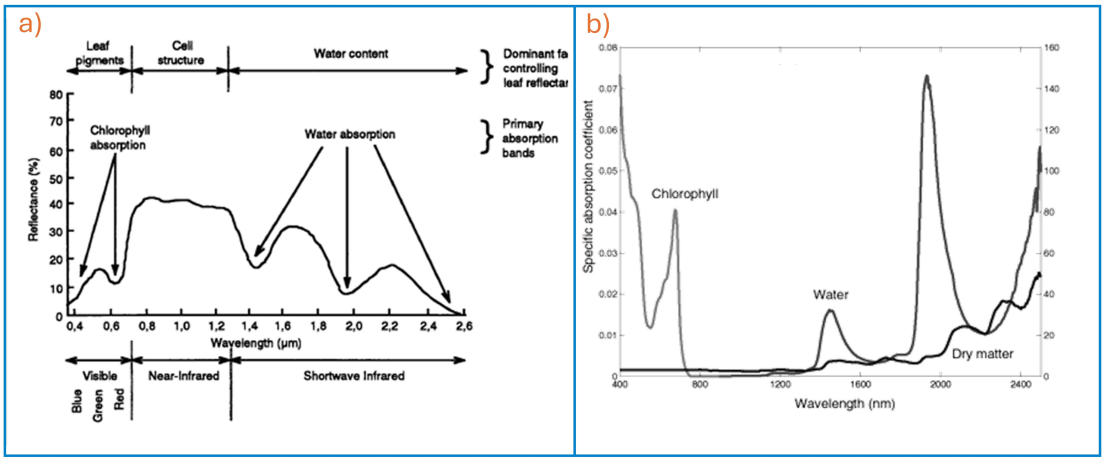

Figure 2.16: (a) Leaf reflectance and dominant drivers across the spectrum [10]; (b) Reference spectra of chlorophyll, water, and leaf dry matter [11].

Principles of spectral reflectance. Plant leaves exhibit characteristic spectral signatures that reflect their biochemical composition, primarily water, chlorophyll, and dry matter, as well as their internal structure [10]. In the visible range (400–700 nm), chlorophyll strongly absorbs light, particularly near ∼450 nm and ∼650 nm [11]. In the near-infrared (NIR; 750–1300 nm), reflectance increases due to scattering from internal leaf structure. In the short-wave infrared (SWIR; 1300–2500 nm), water absorption bands become dominant, especially around 1450 nm and 1940 nm [10, 11].

As illustrated in Figure 2.16, these spectral features are highly informative for assessing plant water status. Under drought stress, reflectance typically increases at water-sensitive wavelengths due to the reduction in leaf water content. Additionally, shifts or reductions in chlorophyll absorption may occur as a result of pigment degradation [136].

2.4.2.1 Near-Infrared (NIR) Spectroscopy

Near-infrared (NIR) spectroscopy is widely used to assess plant water status by analyzing changes in leaf reflectance or transmittance in the 700–1300 nm spectral range [12]. In this region, water does not exhibit strong absorption features; instead, NIR signals are primarily governed by internal leaf structure, multiple scattering, and refractive index contrasts between air-filled and water-filled tissues. Variations in leaf water status therefore influence NIR reflectance indirectly through structural and optical pathway changes rather than through direct water absorption.

Recent studies using Partial Least Squares (PLS) regression on second-derivative spectra in the 700–990 nm range have achieved high accuracy for predicting leaf water potential (LWP), with coefficients of determination up to $R^2 \sim 0.86$ [12]. Field measurements on the abaxial (lower) leaf surface, which is characterized by a thinner cuticle, have shown even greater sensitivity, with reported $R^2 \approx 0.92$ for grapevine cultivars [134].

As illustrated in Figure 2.17, second-derivative spectral processing enhances subtle reflectance variations associated with structural and hydration-related changes, enabling effective discrimination between different water-stress levels in tomato leaves [12].

2.4.2.2 Mid-Wave Infrared (MWIR) Indices

While near-infrared (NIR) methods are well established, the mid-wave infrared (MWIR, 2.5–6 µm) region offers unique advantages for estimating leaf water content, as it encompasses fundamental absorption bands of water near 2.90, 4.65, and 6.08 µm [136]. Several two-band spectral indices have been developed for this purpose, including:

$$\text{MNDWI} = \frac{R_{\lambda_1} - R_{\lambda_2}}{R_{\lambda_1} + R_{\lambda_2}}, \tag{2.22}$$

$$\text{MSRWI} = \frac{R_{\lambda_1}}{R_{\lambda_2}}, \tag{2.23}$$

$$\text{MSDWI} = R_{\lambda_1} - R_{\lambda_2}, \tag{2.24}$$

where R_{λ_1} and R_{λ_2} are the reflectance values at two selected wavelengths. Among these, the Modified Normalized Difference Water Index (MNDWI) has demonstrated strong predictive power, with reported coefficients of determination up to $R^2 \approx 0.89$ for estimating leaf water content [137].

A key benefit of MWIR-based indices is their reduced saturation at high water contents compared to many NIR indices, allowing more accurate tracking over a broader range of hydration states [137].

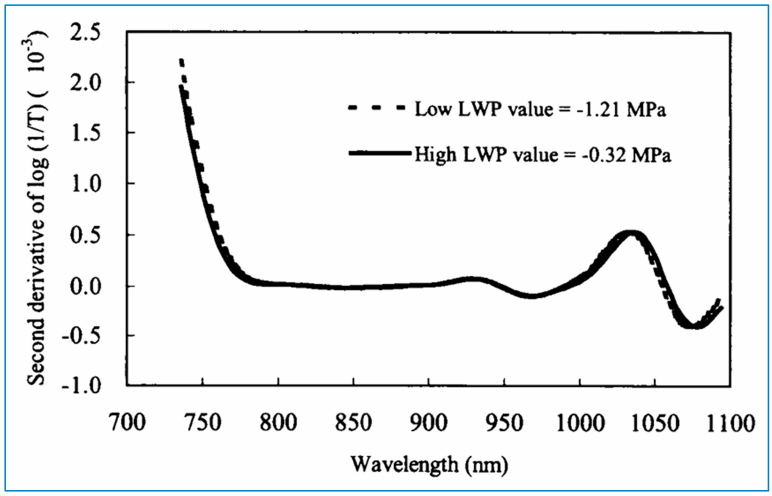

Figure 2.17: Second derivative of tomato leaf spectra highlighting water-stress discrimination [12].

2.4.2.3 Thermal Infrared (TIR) Spectroscopy

TIR provides a complementary perspective by measuring the natural thermal emission from leaves [138]. Water stress can affect both leaf emissivity and temperature. These responses are often species-specific: for instance, *Fagus sylvatica* (beech) exhibited decreased emissivity under stress, associated with cuticle changes, whereas different species within the *Rhododendron genus* showed increased emissivity [138]. Such variability underscores the importance of species-specific calibration for TIR-based stress detection. TIR signals are also sensitive to environmental conditions, such as ambient temperature and wind, which must be controlled or corrected [138].

Despite the advantages of infrared methods, several challenges persist. Spectral saturation in the NIR at high water contents can limit accuracy [12]; interspecific differences in leaf anatomy and structure require careful calibration [137, 134]; and environmental factors such as atmospheric conditions, solar angle, and soil background can influence spectral measurements. These must be considered in both the acquisition protocol and the modeling workflow [134, 138].

2.4.3 Leaf and petiole orientation as an indicator of plant water stress

The orientation of leaves and petioles serves as a valuable morphological indicator of plant water stress, reflecting adaptive mechanisms that minimize water loss while preserving essential physiological functions. Under drought conditions, plants often exhibit leaf rolling or adopt more erect leaf angles to reduce light interception and transpirational water loss. For instance, leaf rolling in *Cistus incanus* has been shown to correlate strongly with reductions in stomatal conductance and photosynthesis, thereby protecting the PSII complex during water stress [139]. Similarly, tomato plants under water deficit display increased mean tilt angles (MTAs) of leaves, a response associated with decreased leaf water potential and lower gas-exchange rates [140].

Digital sensors such as inertial measurement units (IMUs) enable real-time detection of these stress-induced movements, including epinasty (downward bending) in tomato and hyponasty (upward bending) in other species [14]. Changes in leaf orientation are often accompanied by declines in photosynthesis and stomatal conductance, reinforcing their utility as early indicators of water stress. These morphological adjustments contribute to water conservation and offer a non-destructive, practical approach for monitoring crop water status in precision agriculture and stress-management strategies.

2.5 Irrigation: Methods and Infrastructures

2.5.1 Irrigation Methods: Traditional vs Pressurized

All irrigation techniques can generally be categorized into two broad classes: traditional and modern (pressurized) methods. Traditional systems, including surface irrigation practices such as flooding, furrow, border, and basin irrigation, operate primarily through gravity flow. While widely used, these approaches are often characterized by low efficiency and substantial water losses. In contrast, modern irrigation systems employ pressurized delivery mechanisms to enhance precision and water-use efficiency. These include sprinkler systems, drip irrigation, and subsurface drip irrigation (SDI), each offering improved control over water distribution. The following sections provide an overview of the operating principles and typical benefits associated with each method.

2.5.1.1 Traditional Irrigation Methods

Traditional irrigation systems apply water without considering spatial or temporal variability in soil properties or weather conditions influencing evaporation and transpiration [141]. Surface irrigation remains one of the most common practices worldwide and is often the default choice among farmers [142, 143]. However, these methods are often inefficient, with overall water-use efficiency typically around 50% [144].

Border or flat irrigation. In this method, water is distributed over parallel strips of a leveled field. When land leveling is performed accurately, the uniformity of water distribution improves and efficiency can reach between 40% and 60% [145, 146]. The layout of a typical border irrigation system is shown in Figure 2.18a.

Basin irrigation. This approach involves subdividing a level field into sections surrounded by small embankments, forming basins that are temporarily flooded. Although the method is simple and inexpensive, its efficiency generally remains around 40% due to infiltration and runoff losses [147]. Basin irrigation continues to be widely used, particularly in rice cultivation. A schematic representation is shown in Figure 2.18b.

Furrow irrigation. In furrow irrigation, water flows along shallow channels formed between crop rows [13]. This method provides better control than surface or basin irrigation, but runoff losses can still reach about 30% [142]. Automation of inflow timing and volume can further improve efficiency [148]. An example is shown in Figure 2.18c.

2.5.1.2 Modern Irrigation Methods

Modern irrigation systems use pressurized delivery to apply water more efficiently and precisely. These methods include sprinkler, drip, and subsurface drip irrigation (SDI) and are increasingly adopted in water-scarce regions due to their high application efficiency reaching up to approximately 95% [25].

Sprinkler irrigation. This method distributes water by spraying it into the air to simulate rainfall, making it suitable for a wide range of field crops. Application efficiency typically ranges from 50% to 90%, depending on wind and evaporative conditions. When well-managed, sprinkler systems have been shown to reduce

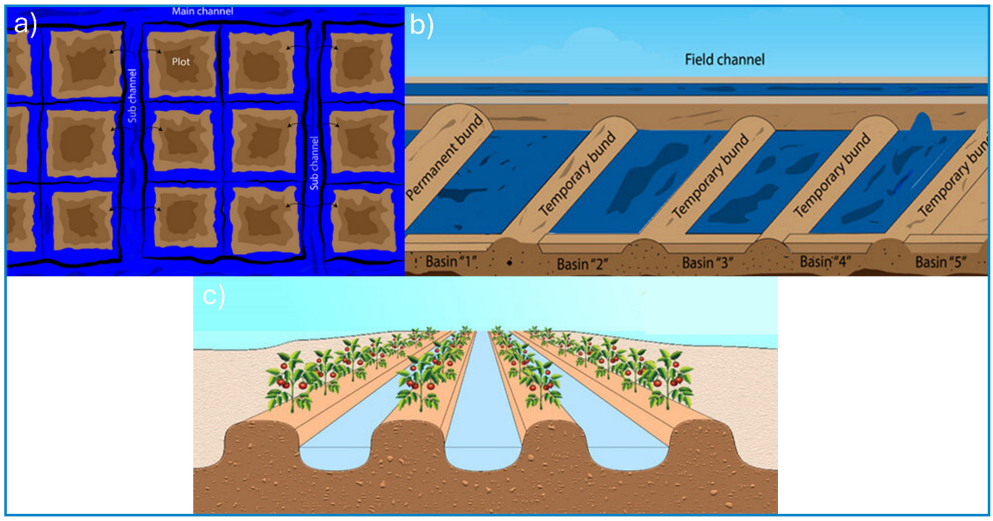

Figure 2.18: Traditional irrigation methods: (a) border or surface irrigation; (b) basin irrigation; (c) furrow irrigation [13].

water usage by up to 26% while maintaining or improving crop yields [147]. An example is shown in Figure 2.19a.

Drip irrigation. Drip systems deliver water slowly and directly to the root zone through a network of emitters, minimizing losses due to evaporation and deep percolation. Efficiency can range from approximately 65% to 95% [149, 150]. Drip irrigation has demonstrated substantial benefits, including yield increases of up to 40% in India [151] and water savings of around 50% for wheat and cotton in Pakistan [150]. Advanced systems can be fully automated or controlled remotely [77]. A typical setup is illustrated in Figure 2.19b.

Subsurface drip irrigation (SDI). SDI places water-delivery laterals beneath the soil surface, ensuring water and nutrients reach the root zone directly. This improves moisture distribution, reduces evaporation, and supports uniform root development [142]. Effective installations include filtration units to prevent emitter clogging, control valves for regulating flow, and fertigation systems for nutrient delivery. Automated scheduling and buried laterals help maintain optimal soil moisture around the root zone. An example of SDI layout is shown in Figure 2.19c.

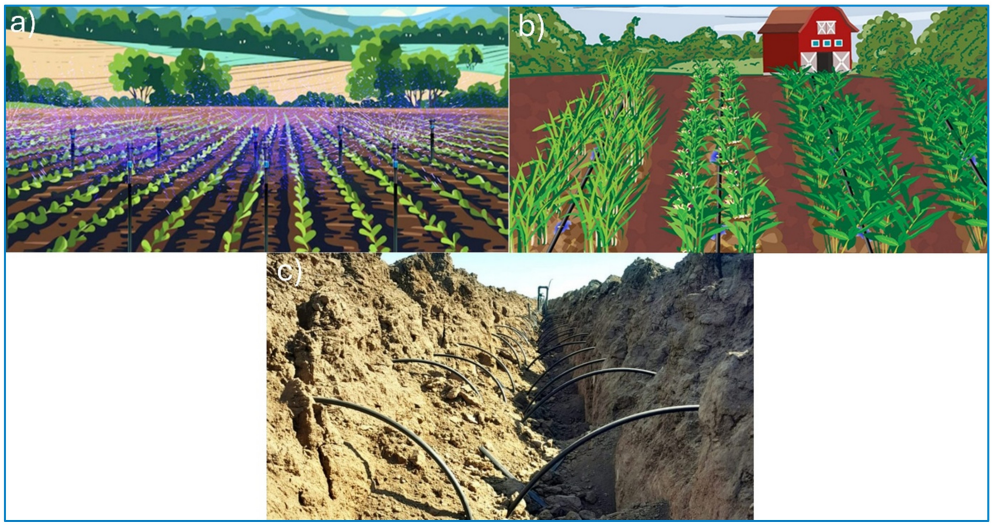

Figure 2.19: Modern irrigation systems: (a) sprinkler irrigation; (b) surface drip irrigation; (c) subsurface drip irrigation (SDI) [13].

2.5.2 Smart Irrigation Infrastructures

Among all the applications of precision agriculture, smart irrigation represents one of the most important areas, especially in the context of increasing water scarcity. It enables the optimized delivery of water to crops through automated, data-driven decision-making systems that ensure the right amount of water is applied at the right time and location [24, 141, 152].

The advantages of smart irrigation are significant from agronomic, economic, and environmental perspectives. Agronomically, it reduces water stress, improves plant vigor, and can enhance both yield and crop quality [153]. Economically, smart irrigation systems can reduce water use by 30% to 50% compared with traditional practices, lowering production costs and improving resilience during drought periods [154]. Environmentally, these systems help minimize runoff and leaching of fertilizers and pesticides into groundwater, preserve soil structure, and support more sustainable agricultural management.

Despite these benefits, widespread adoption of smart irrigation technologies remains limited. The high cost of sensors, probes, and automated control equipment continues to be a major barrier for many farmers [155]. Furthermore, the need for maintenance, including sensor cleaning and calibration, as well as the technical complexity of some systems, can discourage adoption, especially among less experienced users [123].

Smart irrigation relies on a cyber-physical architecture that integrates the In-

ternet of Things (IoT), wireless communication networks, and cloud computing capabilities [156]. Its operation follows a continuous feedback loop designed to monitor and optimize irrigation decisions.

The process begins at the field level, where a network of sensors is installed across the farm to measure key agronomic and environmental parameters such as soil moisture, rainfall, temperature, humidity, potential evapotranspiration, and light intensity. In some cases, drones equipped with thermal cameras are also employed to identify water-stress zones across large agricultural areas. All collected data are transmitted to a central control system [157].

At the control unit, intelligent algorithms, often based on artificial intelligence (AI), analyze the incoming data, taking into account crop type, water requirements, and phenological stage. Based on this analysis, the system sends commands to actuators, such as electro-valves, which start or stop irrigation, typically using drip systems to maximize water efficiency [158].

A key aspect of this process is the reliability and energy efficiency of data transmission. Traditional wireless technologies, including Wi-Fi and Bluetooth, are generally unsuitable for large agricultural fields because of their limited range and high power consumption. Similarly, cellular networks (3G, 4G, 5G), although offering wide coverage, tend to be costly and energy-demanding for large-scale sensor networks [159, 15].

To address these challenges, low-power wide-area networks (LPWAN) have emerged as the most suitable communication technology for smart irrigation IoT systems. LPWAN solutions provide long-range connectivity with minimal energy consumption and low operational cost, making them ideal for large-scale, distributed sensor infrastructures in agriculture.

2.5.2.1 Wireless Communication Technologies

LPWAN overview. Low-Power Wide-Area Network (LPWAN) technologies are specifically developed for applications requiring long-range communication, multi-year battery life, and low deployment cost. These characteristics are well aligned with the needs of precision agriculture [15]. LPWAN solutions are designed to provide reliable connectivity across large rural areas while minimizing energy consumption to extend device lifetime and reduce maintenance. As a result, they offer a practical and scalable approach for Internet of Things (IoT) deployments in agriculture.

Table 2.1 provides a comparison of the main LPWAN families: LoRaWAN, Sigfox, and NB-IoT. The table highlights key characteristics, including modulation schemes, frequency bands, data throughput, and network functionalities.

LoRaWAN has gained particular popularity in agricultural monitoring applications because it combines long communication range, low power consumption, and the flexibility to deploy private networks.

LoRaWAN Communication Protocols. LoRaWAN (Long Range Wide Area Network) is a protocol designed for low-power, long-range wireless communication, well suited for large-scale Internet of Things (IoT) deployments. It builds on LoRa, a proprietary physical layer technology developed by Cycleo (France) and later acquired by Semtech Corporation [160]. LoRa uses Chirp Spread Spectrum (CSS) modulation and operates in unlicensed ISM bands, such as the EU868 MHz band [161]. LoRaWAN defines the upper communication layers, including the network architecture, data transmission protocols, and device roles.

LoRaWAN networks adopt a *star-of-stars* topology. End devices transmit wirelessly to one or more gateways, which forward the messages to a centralized network server through an IP-based backhaul (e.g., Ethernet or cellular) [162, 163]. The network server handles device authentication and session management. Two activation methods are supported: Activation by Personalization (ABP) and Over-the-Air Activation (OTAA). The OTAA is generally preferred because it allows devices to dynamically generate session keys from long-term credentials, assign dynamic device addresses, and enable roaming and key updates, improving overall security [161].

The network server also manages end-to-end security using AES-128 encryption, which is implemented at several protocol layers [162]. Application data are encrypted with the Application Session Key (AppSKey), ensuring that payloads can remain private even from network operators in multi-user environments. Network session keys, on the other hand, secure message counters and control commands [161].

Table 2.1: Technical comparison between the main LPWAN technologies [15, 16].

Feature	**Sigfox**	**LoRaWAN**	**NB-IoT**
Modulation / Frequency Bands	BPSK; ISM bands (868 MHz in Europe, 915 MHz in North America, 433 MHz in Asia)	CSS; ISM bands (868 MHz in Europe, 915 MHz in North America, 433 MHz in Asia)	QPSK; licensed LTE bands
Bandwidth	100 Hz	125–250 kHz	200 kHz
Maximum Data Rate	100 bps	50 kbps	200 kbps
Messages per Day	140 uplink, 4 downlink	Unlimited	Unlimited
Payload Size	12 bytes (UL), 8 bytes (DL)	Up to 243 bytes	Up to 1600 bytes
Typical Range	10 km (urban), 40 km (rural)	5 km (urban), 20 km (rural)	1 km (urban), 10 km (rural)
Authentication and Encryption	Not supported	AES-128 encryption	LTE-standard encryption
Interference Immunity	Very high	Very high	Low*
Adaptive Data Rate	Not supported	Supported	Not supported
Private Network Support	Not supported	Supported	Not supported
Standardization Body	Sigfox and ETSI	LoRa Alliance	3GPP

* NB-IoT operates in licensed LTE frequency bands, which reduces susceptibility to external interference compared to unlicensed ISM-band technologies.

LoRaWAN supports three device classes designed to meet different communication and energy requirements [161, 162]. **Class A** devices, which represent the default and most energy-efficient mode, open two short downlink receive windows after each uplink transmission and then return to sleep mode. **Class B** devices include additional scheduled receive windows synchronized by periodic beacons, allowing more predictable downlink communication suitable for time-based con-

trol operations. **Class C** devices keep their receivers open nearly all the time and are intended for applications that require minimal downlink latency, although this comes at the cost of higher power consumption.

2.5.2.2 Cloud-Integrated LoRaWAN Platforms

Cloud computing provides a scalable and robust infrastructure for managing the large volumes of data generated by IoT sensors. It offers on-demand services that remove the need for investing in expensive physical infrastructure [156]. Cloud systems typically follow a layered architecture, including Infrastructure as a Service (IaaS), Platform as a Service (PaaS), and Software as a Service (SaaS), to ensure flexible and efficient allocation of computing resources [156].

In agricultural applications, cloud platforms significantly enhance the capabilities of LoRaWAN networks by providing more than basic data transmission. LoRaWAN systems, commonly built using platforms such as The Things Network (TTN) [164] or ChirpStack [165], transmit sensor data from gateways to the cloud through lightweight protocols like MQTT or HTTP.

Once transmitted, data are processed using cloud services from providers such as Amazon Web Services (AWS), Microsoft Azure, or Google Cloud Platform (GCP). These platforms allow secure and organized storage of both real-time and historical sensor data [166]. They also support machine learning algorithms and predictive models that convert raw measurements into actionable information for irrigation control and long-term analysis.

Middleware tools such as Node-RED simplify integration by enabling the design of custom data flows and linking cloud services with external APIs or databases. For visualization, InfluxDB (a time-series database) [167] and Grafana (a web dashboard platform) [168] are commonly used to display environmental and crop-related metrics in real time [**?**].

The integration of LoRaWAN with cloud computing enables the development of scalable and remotely operated irrigation systems. These solutions offer continuous feedback on field conditions and contribute to more efficient and sustainable water use.

2.6 Conclusion

A deep understanding of plant physiology, water stress responses, and sensing technologies is essential for the development of reliable tools to monitor plant water status. The literature reviewed in this chapter highlights that, while traditional

reference methods remain fundamental for calibration and validation, there is a growing emphasis on non-destructive, real-time, and plant-centered sensing approaches that can be deployed directly in the field and scaled to large agricultural systems.

This chapter has shown that different plant-based sensing modalities provide complementary information on plant water status across multiple spatial and temporal scales. Electrical impedance spectroscopy (EIS) enables the characterization of tissue hydration and cellular properties through frequency-dependent electrical responses, while near- and mid-infrared optical techniques capture water-related changes through structural scattering effects and wavelength-specific absorption features. In parallel, morphological indicators such as leaf and petiole orientation reflect integrated plant responses to water deficit, linking hydraulic status to adaptive movements associated with transpiration control and photosynthetic regulation.

Building on this state of the art, the present thesis adopts a multi-modal, plant-centric sensing strategy combining electrical impedance spectroscopy, infrared optical measurements, and inertial sensing of petiole movements. The use of inertial measurement units (IMUs) enables continuous, real-time monitoring of stress-induced leaf and petiole reorientation, providing a dynamic indicator of plant water status that complements electrical and optical measurements. Simplified and physiologically interpretable models are selected to ensure robustness, scalability, and suitability for long-term monitoring in controlled and semi-controlled environments.

This chapter therefore establishes the scientific and methodological foundation for the experimental work presented in the following chapters, which focus on the design, implementation, and validation of innovative sensor systems for plant-based water stress detection and integrated irrigation management.

3

Experimental Methods and Materials

3.1 Introduction

The investigation of plant water status can be approached using a wide range of techniques, from traditional destructive methods to advanced non-invasive sensing technologies. Accordingly, this chapter outlines the experimental framework, which is divided into three primary works.

- The first part describes the experimental setup and methodologies employed in the development of optical and electrical sensors for non-invasive monitoring of plant water status (as described in chapter 4), where two non-invasive techniques were developed to monitor the water status of six *Hydrangea macrophylla* plants under outdoor conditions.
- The second part details the experimental campaign conducted at KU Leuven (Belgium), which focused on optimizing and testing a novel wireless IMU-based sensor for real-time monitoring of plant movements. As described in chapter 5, these petiole-mounted sensors were deployed in two commercial greenhouses in collaboration with DRAMCO and other project partners.
- The final part outlines the implementation of the SPRITZ project carried out during my internship at Abinsula company. This section details the

materials and technologies used to deploy a smart irrigation system platform under real-world field conditions as outlined in chapter 6.

Each section highlights the relevant materials, hardware components, experimental designs, and data acquisition protocols specific to the corresponding phase of the research.

3.2 Development of Optical and Electrical Sensors for Monitoring of Plant Water Status

This section outlines the methodologies employed to evaluate plants' water status, integrating both conventional (as reference) and sensor-based techniques. It begins with an overview of the experimental setup and the standard destructive methods. The focus then shifts to the development and application of two non-destructive sensing techniques based on optical and electrical principles.

3.2.1 Experimental Setup

The experiment was conducted on six *Hydrangea macrophylla* plants (as shown in Figure 3.1), selected for their large leaf area, high leaf density, and significant water requirements. These characteristics make them ideal candidates for studying plant water status. All plants were potted in a uniform substrate with a diameter of 30 cm and a depth of 25 cm, filled with a consistent growing medium composed of 40% peat moss, 30% perlite, 20% compost, and 10% sand. This substrate is widely recommended for hydrangea cultivation.

The study took place over a 20-day period during the summer of 2024 on the outdoor terrace of the department of electrical and electronic engineering at the university of Cagliari, Italy (coordinates: 39°13'47.3"N, 9°06'31.3"E), under uncontrolled environmental conditions. The plants were divided into two groups subjected to different irrigation regimes to create varying levels of water stress:

- **Control group:** three well-irrigated plants (A_{well}, B_{well}, C_{well}), watered daily to maintain optimal hydration.
- **Test group:** three poorly-irrigated plants (A_{bad}, B_{bad}, C_{bad}), watered only once every three days, based on prior observations showing that this interval induces noticeable water stress in hydrangeas without causing permanent damage or leaf drop.

Before beginning data collection, all plants underwent a one-week pre-irrigation period to equalize their hydration levels. The experiment was then divided into two distinct phases:

1. **Phase I (Day 1–12):** Daily measurements were taken under the defined irrigation treatments.
2. **Interruption Period (10 days):** All plants received irregular irrigation without measurements. Then all plants underwent a one-week pre-irrigation period to standardize their hydration levels prior to measurement.
3. **Phase II (Day 13–20):** After the one-week pre-irrigation, the original treatment conditions were reinstated and daily measurements recommenced.

To maintain consistency across the monitoring period, a single healthy and well-exposed leaf was tagged on each plant and used for all measurements. Sensor recordings were performed daily in the late evening to minimize variability caused by solar radiation and temperature changes. Relative Water Content (RWC) measurements, which are destructive, were conducted every three days to reduce stress and damage to the plants.

Figure 3.1: Six *Hydrangea macrophylla* plants situated on the terrace of the department.

3.2.2 Destructive Methods for Assessing Water Status

3.2.2.1 Relative Water Content (RWC)

Relative Water Content (RWC) is a standard method for accurately assessing the water status of plant tissues. It represents the ratio between the actual water

content in the tissue and its maximum water-holding capacity. This technique is widely used due to its simplicity and low cost, as it does not require sophisticated instruments. However, it is relatively time-consuming, which is a notable limitation [86]. According to established protocols [86, 169, 82, 83, 84, 170], RWC values typically range from about 98% in fully hydrated leaves to around 30% in severely dehydrated ones. Wilting generally occurs when RWC% value is between 60% and 70%, depending on the plant species [170].

In this study, fully expanded and healthy leaves, well-exposed to sunlight, were selected and carefully cut from each plant. Immediately after harvesting, leaves were placed in aluminum foil bags to prevent loss of turgor. From each leaf, eight circular discs (diameter $\approx 16\,\text{mm}$) were punched using a cork borer, avoiding damaged or necrotic tissue. Each set of discs was placed into labeled glass Petri dishes, which had been pre-weighed.

The fresh weight (FW) of each sample was measured using a high-precision laboratory balance (accuracy: 0.1 mg) [171]. Next, distilled water was added to each dish, and the samples were placed in a cool environment for ($\approx 4\,\text{hours}$) to allow full hydration and reach turgidity. After soaking, the discs were gently blotted with absorbent paper and weighed again to obtain the turgid weight (TW). Finally, the samples were dried in an oven at 70 °C for ($\approx 10\,\text{minutes}$) and weighed once more to determine the dry weight (DW). These three weight values were then applied to calculate the RWC by using Equation 4.1.

3.2.2.2 The Pressure Chamber

The pressure chamber (also known as a pressure bomb) is an instrument used to measure leaf water potential (Ψ_{leaf}). It was originally developed by Scholander *et al.* [73] and is based on the cohesion–tension theory [172], which describes how water is maintained under tension in the xylem due to transpiration.

In this study, the use of this instrument was attempted but ultimately not successful because of a mechanical issue with the compression gland gasket, the component responsible for sealing and holding the leaf stem in place. The stem diameter of the tested plants was smaller than the opening of the gasket, creating a small gap that allowed air to escape and prevented the necessary pressure from building up inside the chamber (as illustrated in Figure 3.2). This specific chamber was originally purchased for use in field experiments on grapevines within the ACUADORI project [173], where stems are significantly thicker and the standard gasket fits properly. Several attempts were made to adapt or modify the gland to fit the thinner stems, but none of the solutions provided a satisfactory seal, making it impossible to perform the measurements in this experimental setup.

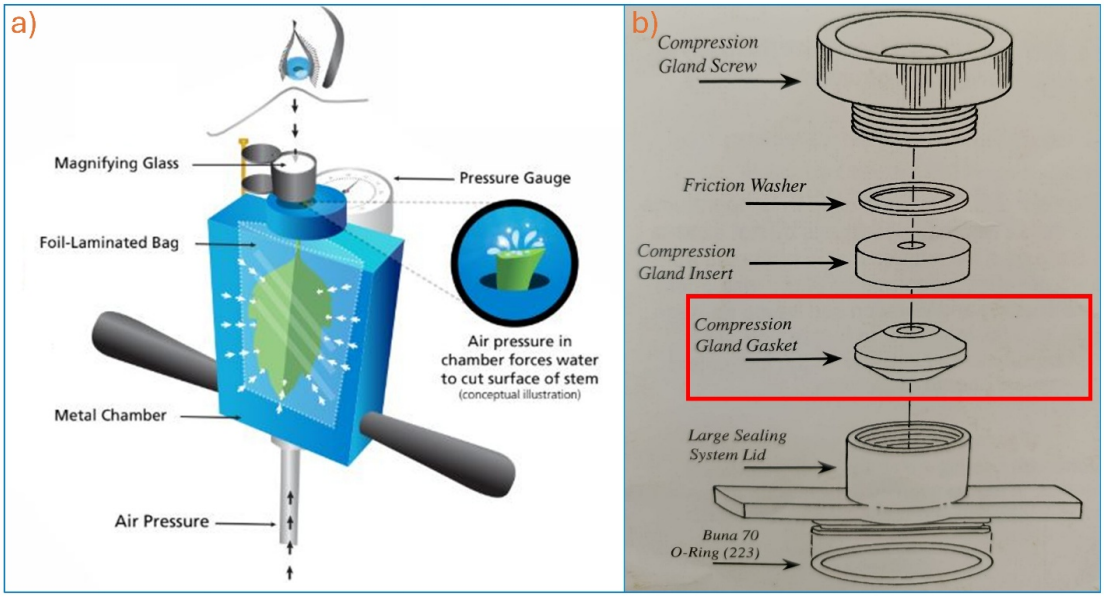

Figure 3.2: (a) Conceptual illustration of a pressure chamber used to measure leaf water potential (Ψ_{leaf}). The cut leaf is enclosed in a sealed metal chamber, and air pressure is gradually applied until xylem sap is forced out at the cut surface of the petiole, indicating the balancing pressure. (b) Exploded diagram of the sealing system components, with emphasis on the compression gland gasket, which is responsible for tightly fixing the leaf stem. In our study, the plant stems were too thin to seal properly, causing air leakage and preventing correct pressurization.

3.2.3 Non-Destructive Optical Method: Near-Infrared Spectroscopy (NIRS)

Infrared spectroscopy was employed in this study as a non-destructive method to assess the water status of plant leaves. As established in subsection 2.4.2, this technique exploits wavelength-dependent interactions between infrared (IR) light and leaf constituents, including water, pigments, and structural components [134, 135]. While strong water absorption features are located at longer wavelengths, the near-infrared (NIR) region provides indirect sensitivity to leaf water status through hydration-related changes in internal scattering and optical path length.

Among the various possible wavelengths, a wavelength of 940 nm was selected as a compromise between sensitivity to water-content-induced structural changes and compatibility with widely available, low-cost electronic components. Although water absorption at 940 nm is relatively weak compared to dominant absorption bands, variations in leaf water content still produce measurable changes in the

transmitted optical signal, making this wavelength suitable for compact, low-power sensing applications.

The experimental setup consisted of three main components: an infrared LED with a peak emission at 940 nm [174], which serves as the light source; a photodiode with a spectral response ranging from 400 nm to 1100 nm [175], which acts as a transducer and converts light into a current; and a transimpedance amplifier (TIA) used as a current-to-voltage converter [176].

The infrared LED was driven by a ramp-up voltage from 0 V to 5 V, generated by the Analog Discovery 2 (AD2) [177], driving an increasing light emission to obtain multiple data points across a range of light intensities, thereby improving signal resolution and data accuracy. A schematic diagram of the optical sensing circuit is given in Figure 3.3. The incident light penetrates through the leaf tissue, where part of it is absorbed by the water content in the leaf, while the transmitted portion is detected by the photodiode. Then, the output photocurrent was amplified and converted into a voltage signal (V_{out}) using a transimpedance amplifier (TIA) realized with a Texas Instruments OPA2137 [176] with a feedback resistor of 24 kΩ. The AD2 was used to simultaneously record both the input waveform and the amplified output signal.

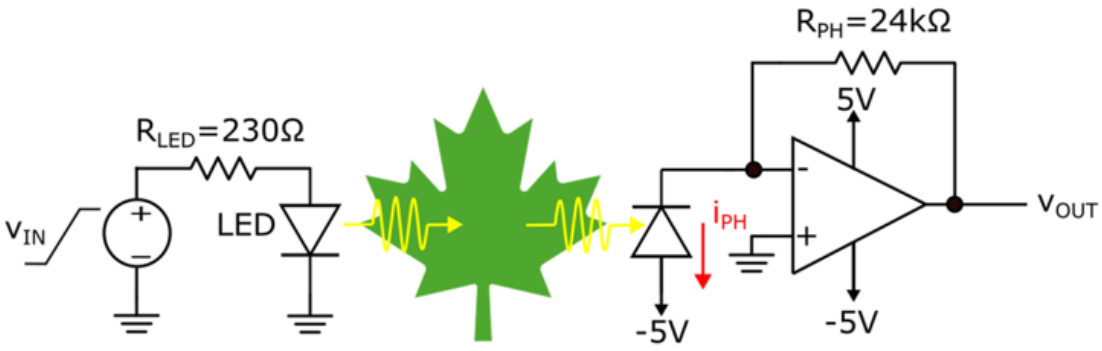

Figure 3.3: Schematic diagram of the optical sensing circuit based on infrared light transmission through a plant leaf.

For practical mounting, the LED and photodiode were fixed onto opposite faces of a custom 3D-printed clip. This clip used embedded magnets to ensure stable and reproducible positioning during the acquisition process, as shown in Figure 3.4.

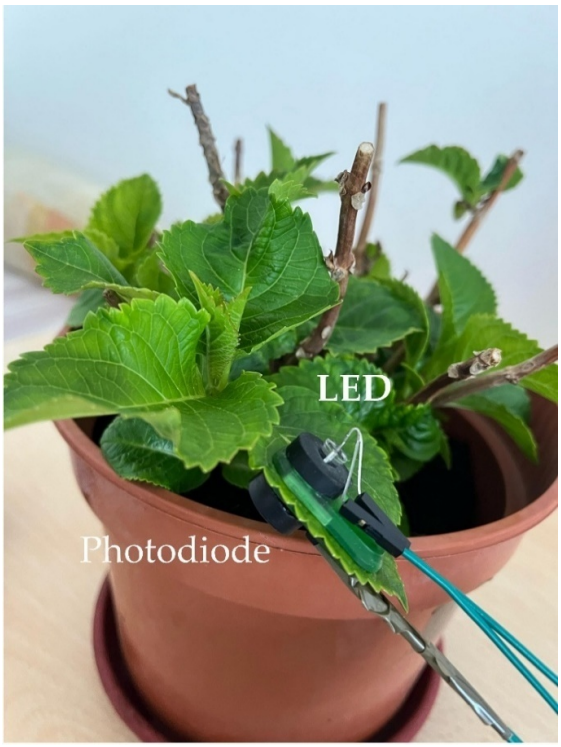

Figure 3.4: Photograph of the corresponding sensor prototype attached to a plant leaf, where the LED and photodiode are mounted on opposite faces of a custom 3D-printed clip, designed with embedded magnets for securing attachment to the leaf.

3.2.4 Non-Destructive Electrical Method: Impedance Spectroscopy (EIS)

Impedance spectroscopy was employed to characterize the electrical properties of the plant tissue, following the theoretical background discussed in subsection 2.4.1. Despite the known limitations of a two-electrode configuration, such as electrode polarization effects, this approach was selected in the present study for its simplicity and suitability for intact leaves, where precise and repeatable electrode placement is crucial to minimizing artefacts due to tissue heterogeneity [114, 117].

The measurement system consisted of the Analog Discovery 2 (AD2) device from Digilent, used in combination with its impedance analyzer adapter, as shown in Figure 3.5. The adapter integrates multiple precision reference resistors (R_{ref}) on its PCB, each connected through electronically controlled switching paths. During a measurement, a single reference resistor is selected via onboard relays based on the impedance range expected for the sample.

Prior to acquisition, the user selects—through the WaveForms software interface—the reference resistance that is expected to be of the same order of magnitude as the leaf impedance. This selection optimizes measurement accuracy by ensuring an appropriate voltage division between the leaf and the reference resistor. If the chosen R_{ref} is significantly larger or smaller than the measured leaf impedance, the software automatically issues a warning, prompting the user to select a more suitable reference resistance from the available set.

A sinusoidal AC excitation signal is generated by the AD2 waveform generator and applied to the leaf via two custom ECG electrodes placed on its upper and lower surfaces. The oscilloscope function of the AD2 is used to acquire two signals simultaneously: Channel 1 (CH1) measures the applied input voltage waveform (V_{input}), while Channel 2 (CH2) records the voltage drop across the leaf (V_{leaf}). The current (I) flowing through the tissue is then determined from the voltage across the selected reference resistor. Using Ohm's law, the complex impedance of the leaf is computed as:

$$Z_{\text{leaf}} = \frac{V_{\text{leaf}}}{I} \tag{3.1}$$

Then, the software measures the phase shift between V_{input} and V_{leaf}, enabling the calculation of both impedance magnitude and phase across a frequency spectrum. A logarithmic frequency sweep from 10 Hz to 1 MHz was performed, using 151 points, providing sufficient resolution for accurate spectral analysis and model fitting. This frequency range captures both the extracellular resistive behavior at low frequencies and the capacitive properties of cell membranes at higher frequencies.

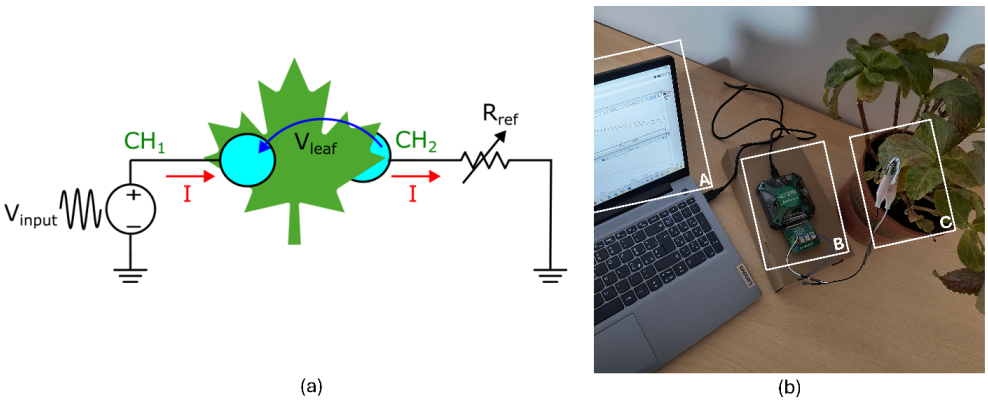

Figure 3.5: (a) Schematic representation of the impedance measurement. (b) Photograph of the impedance spectroscopy measurement setup.

During the experiment, it was observed that prolonged application of the custom commercial ECG electrodes on the leaf surface caused tissue damage, most likely due to the obstruction of stomatal pores responsible for transpiration. To prevent this, an alternative solution was tested using fabricated printable electrodes, produced with a conductive ink deposited through a specialized printing process as shown in Figure 3.6. These electrodes were designed to be more compatible with leaf tissues and intended to remain attached for the entire duration of the experiment. However, they proved to be mechanically fragile because of the thin conductive paths that were easily damaged or erased with even a light tissue contact, which often led to open circuits and loss of conductivity. For this reason, the printable electrodes were not employed, and the custom electrodes were instead used only during the measurement and removed immediately afterward to avoid damaging the leaves. As a result, new electrodes had to be reapplied for each daily measurement.

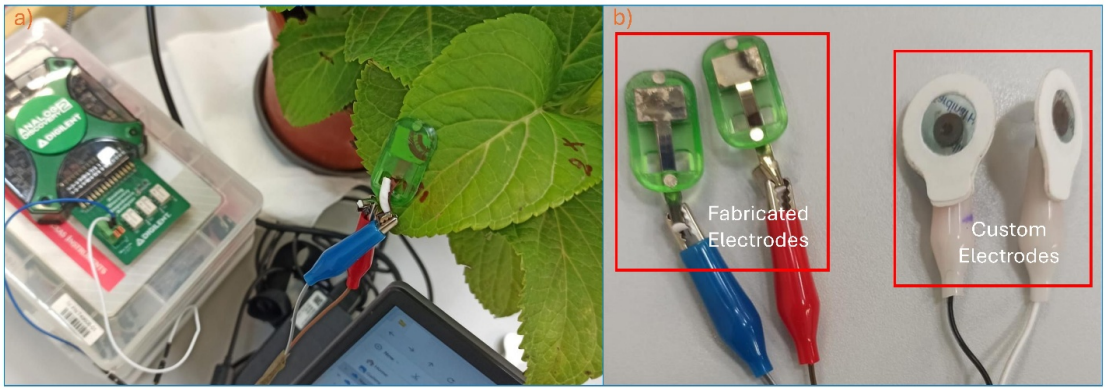

Figure 3.6: (a) A test of impedance measurement with the fabricated electrodes. (b) Photograph showing both the fabricated and custom electrodes.

3.3 IMU-Based Wireless Sensor System for Plant Movement Monitoring

In this part, the developed IMU-based petiole sensor by the DRAMCO group of KU Leuven University is discussed. Then, the experimental setup performed to optimize the power consumption of this sensor is presented, followed by the final deployment of numerous sensors in two different greenhouses of tomato plants subjected to different environmental conditions.

3.3.1 Overview on the IMU-Based Petiole Sensor (DRAMCO Research Group, KU Leuven)

The sensing system developed at KU Leuven is a compact, lightweight, and low-power device designed to be mounted directly on the petiole of the plant to monitor its movements in real time as shown in Figure 3.7. With dimensions of just 28.7 mm × 32 mm × 22.4 mm and a total weight of only 17.89 g (including the battery), the module achieves an autonomy of approximately 14 months [178].

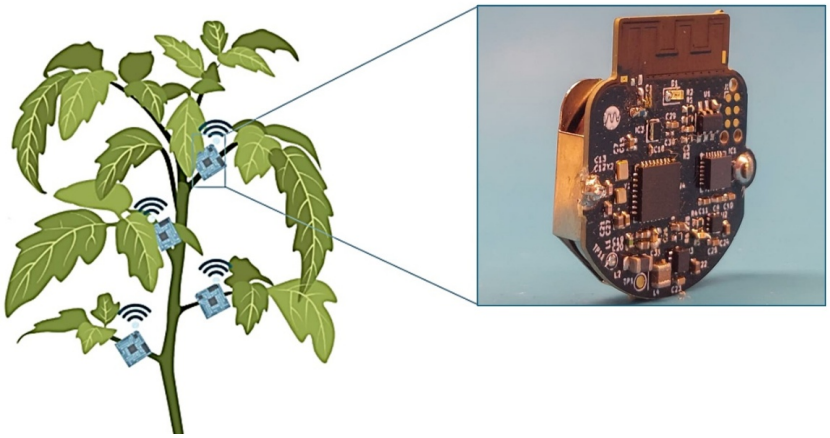

Figure 3.7: Overview of the petiole sensor module developed by the DRAMCO group at KU Leuven.

The device is based on the TDK InvenSense ICM-20948 Inertial Measurement Unit (IMU), a 9-axis sensor that combines a 3-axis gyroscope, 3-axis accelerometer, and 3-axis magnetometer to measure orientation changes in the form of quaternion data. The system is built around a low-power STM32WBA52CG microcontroller, synchronized by a PCF2131 real-time clock (RTC) to manage data collection and communication while operating in ultra-low-power sleep cycles with precise timing. The module transmits data wirelessly using a Semtech SX1280 LoRa 2.4 GHz transceiver, which offers a high data rate (up to 253 kbps) and low power consumption (8.2 mA in receive mode, 24 mA in transmit mode), achieving a communication range of over 1 km suitable for greenhouse deployment[178].

Each transmission consists of three aggregated IMU measurements (8 bytes each) and timestamps, bundled into a 32-byte packet sent every 15 minutes to reduce the energy cost of frequent wireless transmissions. The sensor is powered by a non-rechargeable 3.6 V Li–$SOCl_2$ battery (Saft LS14250), chosen for its high energy density and low self-discharge[178].

Figure 3.8 illustrates the current consumption profile of the plant-mounted

sensing system over a complete 15-minute operating cycle. To maximize battery life, the sensor operates primarily in an ultra-low-power sleep mode, drawing negligible current. It exits this state three times per 15-minute cycle. The first two wakeups are for intermediate IMU measurements, each causing a brief current spike as the microcontroller and sensor activate. The final wake-up near the cycle's end is for the third measurement, followed by supercapacitor charging and LoRa data transmission.

It should be noted that the supercapacitor provides the high current required for LoRa transmission, thereby protecting the main battery from damage. After the transmission, the system returns to its sleep mode, repeating the cycle with high energy efficiency.

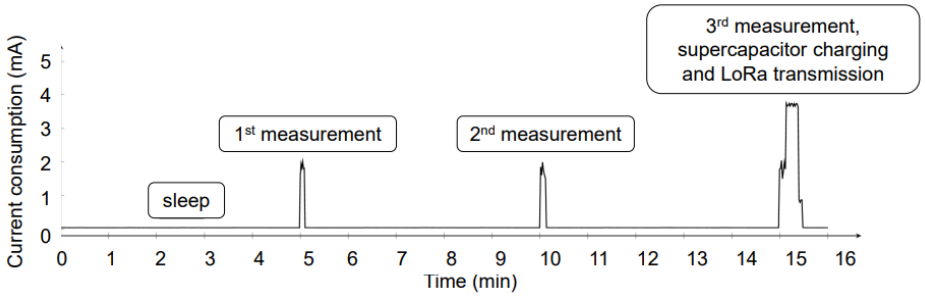

Figure 3.8: Current consumption over time for each measurement stage (adapted from the project presentation by the DRAMCO group).

3.3.2 Experimental Setup for Power Consumption Optimization

The first part of this study focused on reducing the energy consumption of the petiole movement sensor system by optimizing the number of events collected during each IMU measurement. The goal was to achieve a significant reduction in power consumption while maintaining the accuracy and reliability of orientation measures.

The standard measurement procedure (the original implementation) implemented in the sensor consisted of collecting 120 samples from the IMU, discarding the first 20 to avoid potential stabilization artifacts, and averaging the remaining 100 samples to obtain the final quaternion values (w, x, y, z).

The experimental setup was divided into main phases: starting firstly from fixing the sensor in one common position and secondly by reducing the number of raw IMU samples from the original implementation of 120 events down to 100, then

80, and finally 60 events. In each implementation, three successive measurements were done.

To achieve this, some modifications were applied to the sensor development project in STM32CubeIDE. The sensor was connected to the debugger via a specific extension for uploading the firmware to the processor. The Arduino IDE serial monitor was used to capture all the data events of the different measurements.

The sampling reduction logic is illustrated in Figure 3.9 and Figure 3.10, where the averaging window was reduced from 120 to 100 samples in order to save energy. As shown in these figures, modifications to the files `App_imu.c` and `App_gateway.c` were introduced to decrease the number of IMU measurement events from 120 in the original implementation to 100 in the reduced version.

```
// From App_imu.c
// ==== original implementation (120 samples, skip first 20) ====
if (measurementIndex == 0) {
    if ((imuMeasurementNr > 19) && (imuMeasurementNr <= 121)) {
        imuMeasQuatArray[imuMeasurementNr - 20].w = quat.w;
        imuMeasQuatArray[imuMeasurementNr - 20].x = quat.x;
        imuMeasQuatArray[imuMeasurementNr - 20].y = quat.y;
        imuMeasQuatArray[imuMeasurementNr - 20].z = quat.z;
    }

    if (imuMeasurementNr == 120) {
        quat64b.w = quat64b.w + 0;
        quat64b.x = quat64b.x + 0;
        quat64b.y = quat64b.y + 0;
        quat64b.z = quat64b.z + 0;

        for (int i = 0; i < 100; i++) {
            quat64b.w += imuMeasQuatArray[i].w;
            quat64b.x += imuMeasQuatArray[i].x;
            quat64b.y += imuMeasQuatArray[i].y;
            quat64b.z += imuMeasQuatArray[i].z;
        }

        quat.w = (int16_t)((quat64b.w + 50) / 100);
        quat.x = (int16_t)((quat64b.x + 50) / 100);
        quat.y = (int16_t)((quat64b.y + 50) / 100);
        quat.z = (int16_t)((quat64b.z + 50) / 100);
    }
}

// From App_gateway.c
while (imuMeasurementNr < 120) {     // make sure minimum 120 IMU
    measurements are done
    xTaskNotifyStateClear(gatewayThreadHandler);

    if (xTaskNotifyWait(0x00, 0xffffffff, &notificationValue,
                        pdMS_TO_TICKS(200))) {

        // notification from IMU interrupt
        if ((notificationValue & NOTIFICATION_FROM_IMU)
            == NOTIFICATION_FROM_IMU) {

            // poll IMU data
            PollImuDevice();
        }
    }
    else {
        // timeout branch ...
    }
}
```

Figure 3.9: Firmware logic for the original implementation using 120 IMU samples (skipping the first 20). Quaternions are accumulated over 100 samples and averaged using the `(+50)/100` scaling. The gateway loop waits until at least 120 measurements are collected before proceeding.

```
// From App_imu.c
// === reduced-sampling version (100 samples, skip first 20) ===
if (measurementIndex == 0) {
    if ((imuMeasurementNr > 19) && (imuMeasurementNr <= 101)) {
        imuMeasQuatArray[imuMeasurementNr - 20].w = quat.w;
        imuMeasQuatArray[imuMeasurementNr - 20].x = quat.x;
        imuMeasQuatArray[imuMeasurementNr - 20].y = quat.y;
        imuMeasQuatArray[imuMeasurementNr - 20].z = quat.z;
    }

    if (imuMeasurementNr == 100) {
        quat64b.w = 0;
        quat64b.x = 0;
        quat64b.y = 0;
        quat64b.z = 0;

        for (int i = 0; i < 80; i++) {
            quat64b.w += imuMeasQuatArray[i].w;
            quat64b.x += imuMeasQuatArray[i].x;
            quat64b.y += imuMeasQuatArray[i].y;
            quat64b.z += imuMeasQuatArray[i].z;
        }

        quat.w = (int16_t)((quat64b.w + 40) / 80);
        quat.x = (int16_t)((quat64b.x + 40) / 80);
        quat.y = (int16_t)((quat64b.y + 40) / 80);
        quat.z = (int16_t)((quat64b.z + 40) / 80);
    }
}

// From App_gateway.c
while (imuMeasurementNr < 100) {     // make sure minimum 100 IMU
    measurements are done
    xTaskNotifyStateClear(gatewayThreadHandler);

    if (xTaskNotifyWait(0x00, 0xffffffff, &notificationValue,
                        pdMS_TO_TICKS(200))) {

        if ((notificationValue & NOTIFICATION_FROM_IMU)
            == NOTIFICATION_FROM_IMU) {
            PollImuDevice();    // Poll device for data
        }
    }
    else {
        // timeout branch ...
    }
}
```

Figure 3.10: Firmware logic for the reduced-sampling implementation using 100 IMU samples. The averaging window and normalization factors are reduced (`(+40)/80` instead of `(+50)/100`), and the gateway only waits for 100 measurements instead of 120.

The same process was applied in two different initial positions: 90° and 0°. Figure 3.11 shows the sensor taking measurements in two fixed positions at 90° and at 0° relative to the ground level.

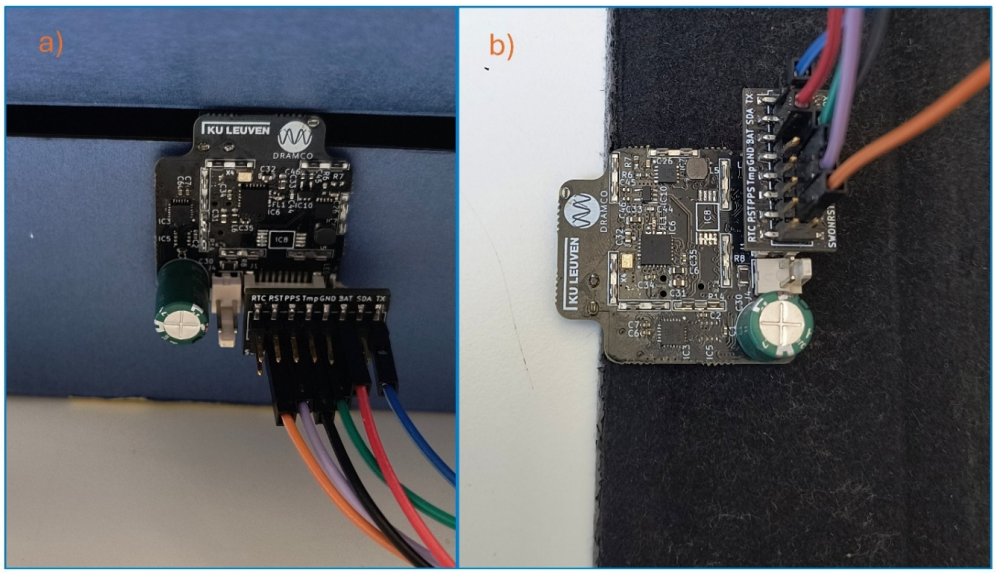

Figure 3.11: Sensor measurements in two fixed positions: (a) 90° and (b) 0° relative to ground level.

3.3.3 Experimental Setup in Greenhouses

Two distinct experimental groups were established, each housed in a separate greenhouse with different environmental conditions. The first group (Set1 in the first greenhouse and Set3 in the second greenhouse) comprised plants that grew under natural lighting and standard climate conditions (control group). The second group of plants (Set2 in the first greenhouse and Set4 in the second greenhouse) were exposed to supplemental artificial lighting provided by energy-efficient LED systems (test group). The two experiments were conducted in different periods: from 20 February to 19 March 2025 for the first greenhouse (Set1 and Set2), and from 10 March to 24 March 2025 for the second greenhouse (Set3 and Set4).

Petiole sensor modules were mounted directly onto the tomato plant petioles. To ensure stable fixation and minimize impact on plant growth, the sensors were enclosed in lightweight protective casings produced by a project partner. These casings were specifically designed to allow non-invasive attachment to the petiole while protecting the electronics from environmental factors. Figure 3.12 shows

photos captured during the experiments in the greenhouses, where sensors are attached to different petioles of tomato plants.

In Set1, which initially had 10 sensors (S1-01 to S1-10), sensors S1-01 and S1-10 were excluded due to physical damage when they fell. In Set2, also with 10 initial sensors (S2-01 to S2-10), sensor S2-07 was excluded for insufficient data and S2-10 was excluded due to physical damage. For Set3, which contained 12 sensors, S3-01, S3-02, S3-03, S3-05, and S3-06 were excluded because they were either damaged or provided insufficient data transmission. Similarly, from the 12 sensors in Set4, S4-01, S4-02, S4-03, S4-06, and S4-07 were excluded for the same reasons.

Figure 3.12: Deployment of IMU-based sensor modules in greenhouses under different environmental conditions.

3.4 Implementation of Smart Irrigation Platfrom

In this section, it will be discussed the experimental setup and the different components used for the implementation of smart irrigation platform on a farm of a project partner, while the operating principle will be explained in more detail in chapter 6. The project aims to achieve two operational objectives, firstly to reduce water and energy consumption, and secondly to improve crop productivity by giving the plants just the needed quantity of water at the right time by using multiple sensors and control systems.

3.4.1 Experimental Setup

The platform was implemented on the partner farm “Agriturismo Agave” located in Strada Statale 291 Della Nurra in Alghero, Sardegna as shown in Figure 3.13 a

photo of the site. The field was divided into four separate irrigation zones where each zone contains two rows of different crops of tomato plants. This system delivers water directly to the base of each plant using an efficient drip irrigation system. This approach minimizes water waste by reducing evaporation and helps prevent the spread of disease by keeping the leaves dry.

Across the field, a network of battery-powered sensors, including soil probes, a weather station, leaf wetness sensor, PAR sensor, LoRaWAN gateway, a water meter and a smart irrigation controller, which represent the core of the project. All sensors communicate wirelessly with the LoRaWAN protocol, which is perfect for agricultural applications. The different devices used in this deployment will be explained in the following section.

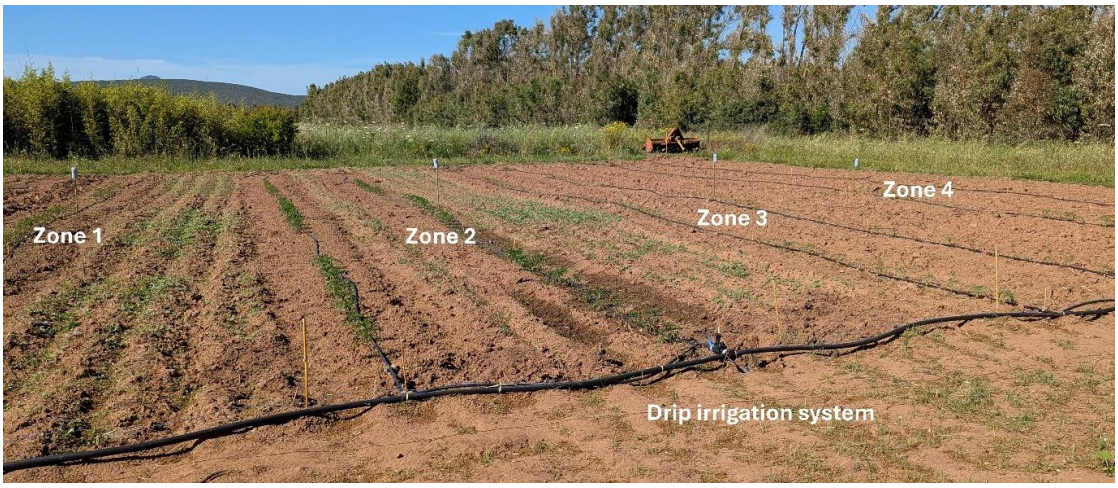

Figure 3.13: A photo of the site of the implementation of the irrigation system in the partner farm “Agriturismo Agave”.

3.4.2 The Different Components Used for the implementation

3.4.2.1 Soil probes SenseCAP S2105 (Seeed Technology, China)

SenseCAP S2105 is a stand-alone soil monitoring sensor characterized by two parts as shown in Figure 3.14. This structure includes a sensor head dedicated to measuring physical parameters (moisture, temperature, and electrical conductivity) and a modular controller/datalogger where both communicate via a robust RS-485 connection using the Modbus RTU protocol.

The sensing part S-Temp&VWC&EC-02A provides essential measurements for comprehensive soil analysis including the three sensors: Volumetric water content (VWC), with a range of 0 to 100%, determined by a capacitance/FDR method that estimates the electrical permittivity of the soil, the temperature is measured by an embedded thermistor/IC in the range of -40 to +80 °C with an uncertainty of ±0.5 °C and the electrical conductivity is measured via an AC excitation across the electrodes in a range of 0 to 10 mS/cm^{-1}, which indicates salinity or fertility, after thermal compensation to 25 °C thanks to the temperature sensor. The controller/ datalogger is housed in a weatherproof enclosure that provides communication and power management by hosting a low-power MCU and LoRaWAN radio (Wio-E5 STM32WLE chip) and a battery of type Li-SOCl2 D-cell (3.6 V, 19 Ah) giving (up to 10-year) battery life. It acts as a sensor node (LoRaWAN v1.0.3, Class A) in the LoRaWAN network where measurements are read via Modbus, assembled and packaged in a payload, and transmitted over the regional LoRaWAN band (e.g., EU868/US915). A built-in Bluetooth interface allows field technicians to set region, join method (OTAA), intervals of sending data, and view diagnostics via a mobile application.

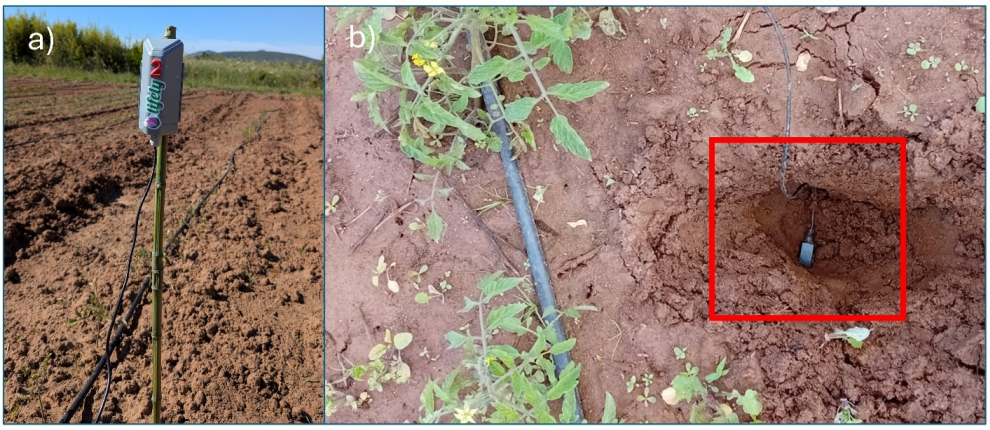

Figure 3.14: (a) An on-site photo of the soil probes (b) the soil sensors are deeply immersed in soil to accurately measure the physical parameters.

3.4.2.2 SenseCAP S2120 LoRaWAN 8-in-1 Weather Station (Seeed Technology, China)

The SenseCAP S2120 is compact in size, all-in-one weather monitoring station designed for outdoor environmental sensing and long-range data transmission [179]. It integrates eight key sensors into a single unit, capable of measuring air temper-

ature, relative humidity, barometric pressure, wind speed and direction, rainfall, light intensity, and UV index.A photo the installed weather station on the site is illustrated in Figure 3.15. The air temperature sensor operates across a wide range from 40 °C to 80 °C, with a resolution of 0.1 °C and an accuracy of ±0.5 °C in the range of 20 to 80 °C. Relative humidity is measured from 1 to 99 %RH, barometric pressure from 540 to 1100 hPa, and wind speed from 0 to 50 m/s, with fine resolution (0.01 m/s) and accuracy (±0.5 m/s for <5 m/s). Wind direction is detected over a full 360° range with 1° resolution, while rainfall is quantified from 0 to 450 mm/h. The light intensity sensor captures data up to 200,000 lux, and UV index measurements range from 0 to 16.

At the heart of the controller and datalogging subsystem is the WM-LR1110 module, which integrates a Semtech LR1110 LoRa transceiver with a Nordic nRF52840 microcontroller (MCU), enabling the station to operate as a LoRaWAN v1.0.3 Class A sensor node for long-range wireless communication (2 to 10 km, depending on environmental conditions). It is compatible with multiple LoRaWAN frequency plans (EU868/US915, etc.) and includes a customizable GPS option.

Power is supplied primarily by a 0.5 W solar panel, backed by three internal AA-sized 1.5 V lithium batteries. The dual power strategy allows the device to remain operational for up to two years. This design enables optimal environmental sensing in various field conditions, making it a suitable choice for precision agriculture.

3.4.2.3 SenseCAP S-YM-01 Leaf Wetness integrated with SenseCAP S2100 LoRaWAN Data logger (Seeed Technology, China)

The leaf witness sensor works on a biomimetic principle: its leaf-shaped design allows it to faithfully reproduce the properties of a real leaf, so condensation and evaporation occur at rates like natural leaves. It detects the presence of water (dew, rain, or ice) on its surface by measuring variations in an electric field and converts these changes into a 0–100 % wetness index proportional to the fraction of the surface covered by water [180]. This approach offers high sensitivity from the very first droplets and enables accurate detection of leaf wetness events that are crucial in agriculture, since leaves that are too wet strongly favor the development of fungal diseases such as mildew [181, 182]. For reliable measurements, the sensor is mounted on a station arm with the sensing surface facing upward and slightly inclined to mimic natural runoff and droplet behavior, as shown in Figure 3.16b.

The sensor transmits its readings via a MODBUS-RTU protocol over an RS-485 interface to a SenseCAP S2100 LoRaWAN Data Logger, designed to collect and transmit data from third-party industrial sensors [180]. Internally, it uses Seeed's Wio-E5 system-on-chip (STM32WLE), which combines an STM32 microcontroller

Figure 3.15: SenseCAP S2120 8-in-1 LoRaWAN Weather Station installed on the site.

with a LoRa transceiver and runs LoRaWAN v1.0.3 Class A. The logger is optimized for low power: its firmware keeps the MCU in deep sleep, periodically wakes to power and poll the measurement, packages data into a compact LoRaWAN uplink, transmits it using multiple LoRaWAN frequency plans (EU868/US915, etc.), and then returns to sleep. Power is provided by an internal battery for long field autonomy but can also be supplied by an external 12 V DC source when available, as shown in Figure 3.16a.

This architecture enables the leaf witness to operate for extended periods with minimal maintenance and to transmit data remotely to LoRaWAN gateways for agricultural monitoring and disease-risk assessment.

3.4.2.4 SenseCAP S-ZFS-02 solar-radiation sensor integrated with SenseCAP S2100 LoRaWAN Data logger (Seeed Technology, China)

The S-ZFS-02 is an industrial pyranometer that measures global solar radiation in the wavelength range of 300 to 1100 nm with an accuracy of ±3 % and a measurement range of 0–2000 $W \cdot m^{-2}$ [183]. It operates on the principle of a silicon

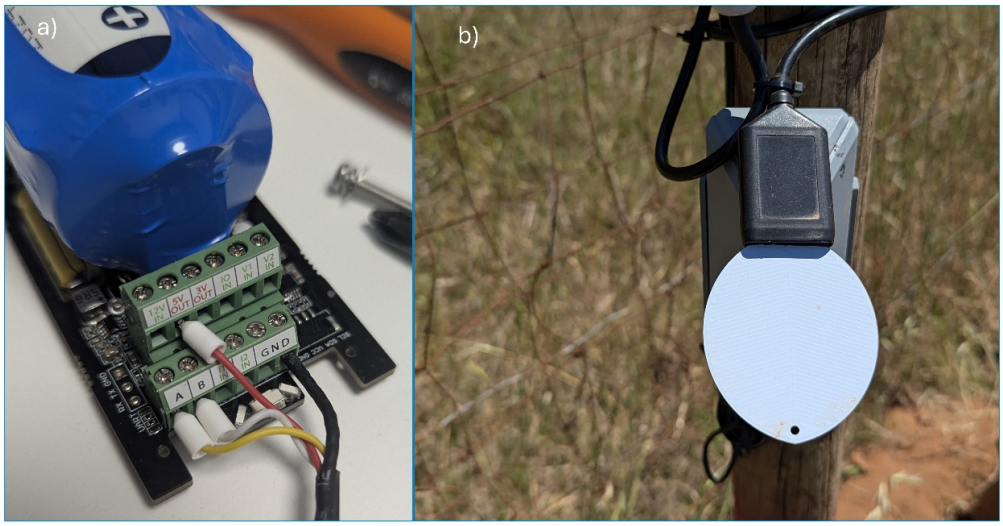

Figure 3.16: (a) A photo of the SenseCAP S2100 LoRaWAN Data controller/logger connected with leaf witness sensor outputs via MODBUS-RTU interface. (b) A photo of the leaf witness sensor installed on the site.

photodiode combined with an optical diffuser that complies with the cosine law, ensuring accurate measurement of incident irradiance regardless of the sun's angle. Monitoring solar radiation is important in agriculture because it directly influences photosynthesis, plant growth and water demand. The Sensor was connected to the SenseCAP S2100 LoRaWAN Data Logger using the same MODBUS-RTU (RS-485) interface and communication setup described previously for the leaf witness sensor. This configuration allows the pyranometer to be powered and polled by the logger, which then packages the measurements into LoRaWAN uplinks for remote transmission. Figure 3.17 shows the installation of this combination on the site at an arm. This setup enables long-term, low-maintenance monitoring of solar radiation in the field and reliable integration into precision agriculture.

3.4.2.5 RAK7249 WisGate Edge Max LoRaWAN gatway (RAKwireless Technology Limited, China)

The RAK7249 WisGate Edge Max is a robust LoRaWAN® gateway designed for use in wide-area agricultural and environmental monitoring networks [184]. It is built with a durable weather-resistant aluminum case that protects it from rain, dust, and temperature changes, making it suitable for long-term outdoor installation. The gateway includes a processing module based on a MediaTek MT7628 processor running OpenWRT Linux, together with one SX1301 LoRa concentra-

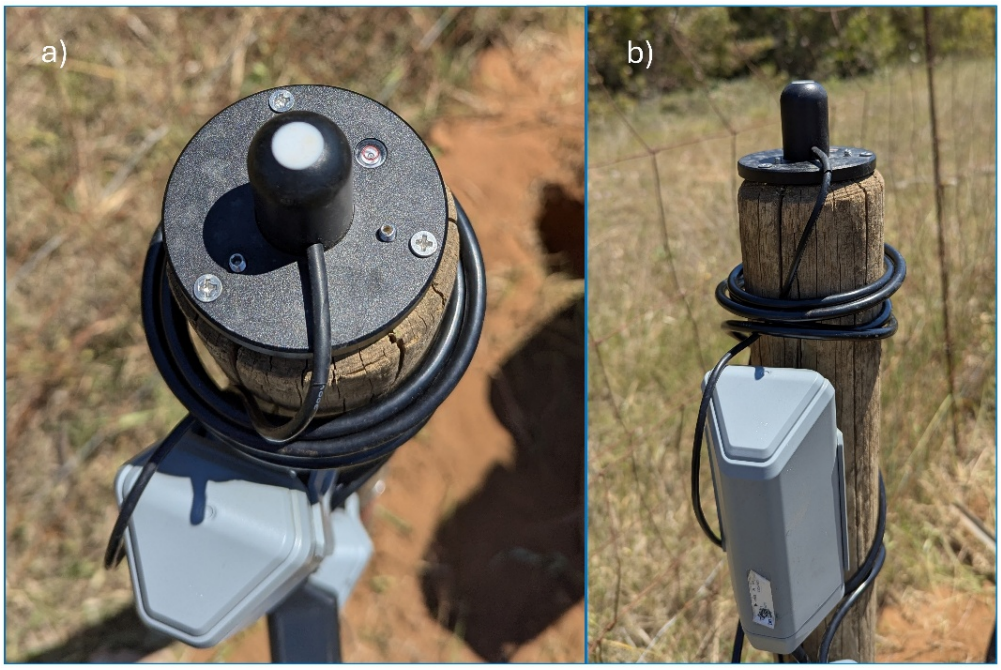

Figure 3.17: (a) A horizontal photo of the PAR sensor implemented on the site. (b) A transversal photo of the PAR sensor integrated with SenseCAP S2100 installed on the site.

tor card supporting 8 channels that allow it to receive data from multiple sensors at the same time. It can maintain stable communication over several kilometers thanks to its high transmit power of up to 27 dBm and its receiver sensitivity down to 139 dBm. The device supports Ethernet, Wi-Fi, and 4G/LTE connections for data transmission and includes built-in GPS for accurate time and location. It can be powered via Power-over-Ethernet (PoE 802.3af/at) or by an external 12 V source. Its software provides a simple web interface for configuration and includes features for secure communication through encryption and basic network functions such as data forwarding and firewall protection. It can function either as a packet forwarder to external servers such as AWS IoT Core for LoRaWAN, or as a local LoRa network server, managing connected sensors directly. During operation, the gateway demodulates incoming signals from LoRaWAN end devices timestamps them using GPS, and forwards data securely to the network server, and if the internet connection is lost, it stores the data temporarily and forwards it automatically once the connection is restored. The RAK7249 offers a reliable backbone for smart irrigation and precision agriculture systems that need continuous data collection in outdoor environments. Figure 3.18 shows the LoRaWAN

gateway installed on the site.

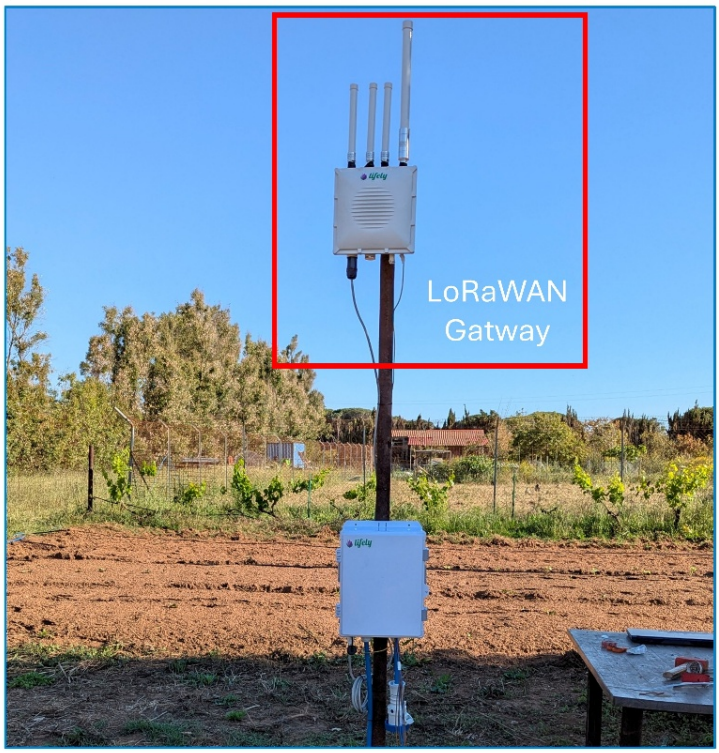

Figure 3.18: A photo of the installation of a LoRaWAN gateway on the site.

3.4.2.6 ESP32-S3 Irrigation Controller (Lifely, Italy)

At the heart of the automated irrigation system is the custom SPRITZ board (rev. 2.1), developed by "Lifely" company. This compact board acts as the intelligent "brain" that manages valve actuation. It built around a powerful and efficient ESP32-S3 chip, which is characterized by its good compute, low-power operation, and its mineable connectivity (Wi-Fi + Bluetooth). The hardware is composed of different components as shown in Figure 3.19. While the description of each component is mentioned in the following section.

Legend (matching callouts):

1. **ESP32-S3-WROOM-1 (U2)** — Main MCU with Wi-Fi/BLE. Runs the irrigation firmware: valve scheduling, MQTT/HTTP client, LED status, and button handling.
2. **Power header (H3)** — Breaks out board rails: 5V, 3.3V, and GND.

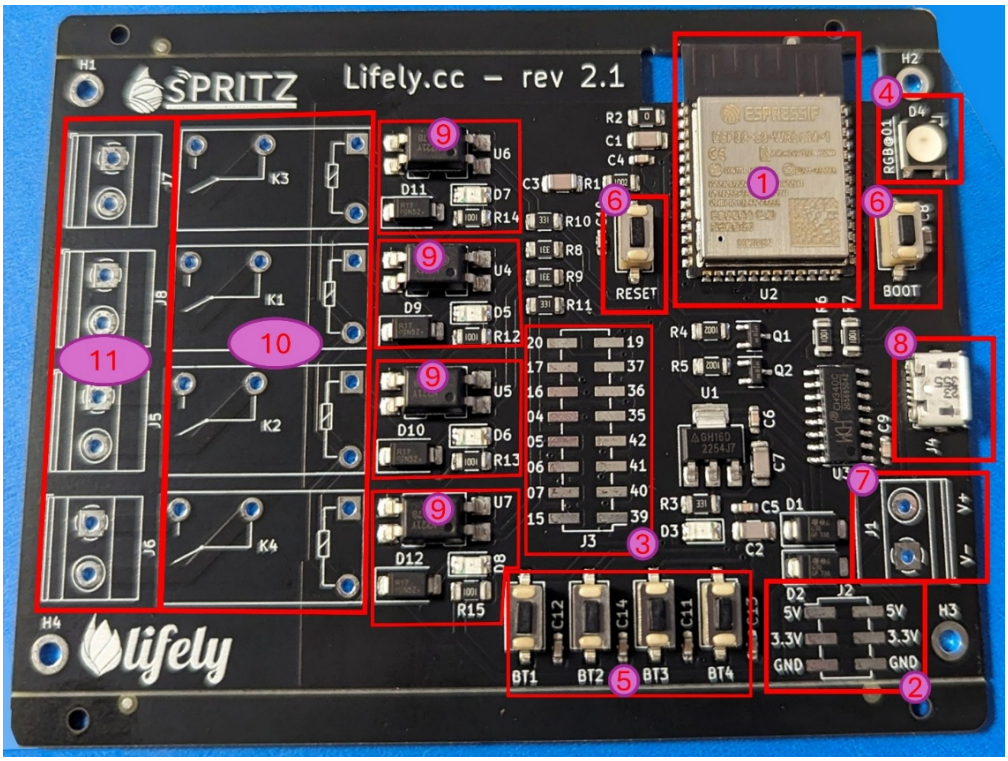

Figure 3.19: A photo of the irrigation controller “the SPRITZ board”.

3. **Expansion header (J3)** — Extra ESP32 GPIOs for add-on sensors/IO.

4. **RGB status LED (D4 / RGB001)** — Multi-color indicator for power-on, Wi-Fi pairing/connected, valve activity, and fault codes (blink patterns).

5. **Manual override buttons (BT1–BT4)** — Per-zone test/override for quick field checks.

6. **RESET & BOOT (SW [Reset], SW [Boot])** — Hardware controls for entering bootloader and resetting the MCU (used during flashing/recovery).

7. **Field power input (J1, V^+/V)** — 24V input for solenoid valves.

8. **Micro-USB (J4) + USB-to-UART (U3, CH340C)** — Programming and console: connect to a PC to flash via UART and read serial logs.

9. **Per-zone driver & protection (U4–U7, D9–D12, R/C)** — Interface between ESP32 and relay/solenoid loads: transistor/driver stages for level shifting/current drive; flyback diodes clamp inductive spikes; R/C parts shape signals and protect the MCU.

10. **Relay bank (K1–K4)** — Four relays (one per zone) switching the 24V field supply to solenoid valves; each zone controlled by the ESP32.

11. **Screw terminals (H1–H4)** — Field connections for the four valve outputs; sized for typical irrigation wiring.

In the field setup, the control unit was installed inside a protective cage to ensure durability against outdoor conditions. The cage was firmly fixed to a metallic pole using clamps, as illustrated in Figure 3.20. Inside the enclosure, the SPRITZ board was mounted and connected to the 24 V DC power supply, which provides the necessary energy to drive the irrigation valves.

The electrical wiring was carefully routed. The output terminals of the relays were connected to the valve cables, allowing each valve to be independently actuated according to the control signals sent by the ESP32-S3 microcontroller. The power adapter highlighted in the red square in Figure 3.20b converts the AC input into a stable 24 V DC supply, ensuring safe operation of the electronic components and the field actuators.

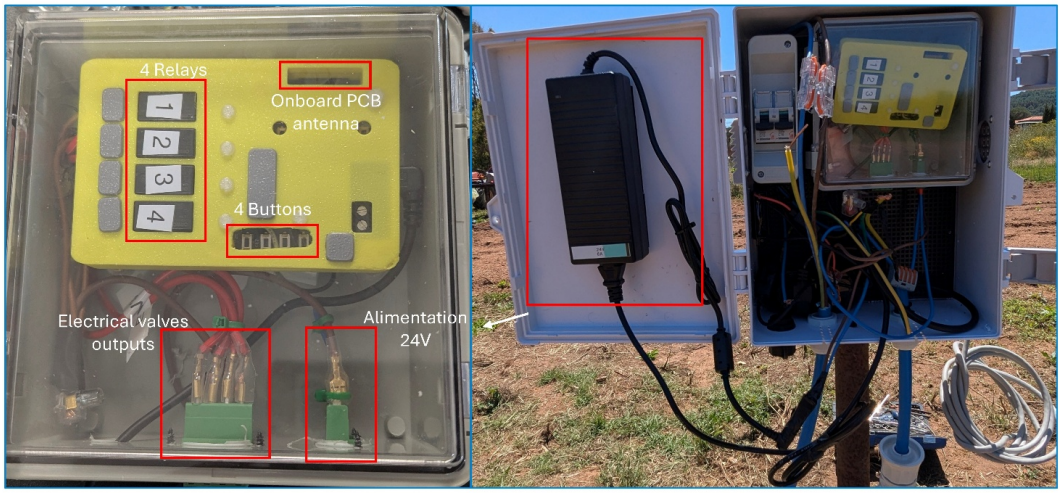

Figure 3.20: (a) The SPRITZ irrigation controller unit installed inside a protective cage showing its different components (b) A weather-proof enclosure with AC–DC power supply.

3.4.2.7 Ultrasonic LoRaWAN Water Meter (GAO Tek Inc, USA)

The LoRaWAN ultrasonic water meter, with a nominal diameter of DN40 (40 mm), operates based on the transit-time principle, which measures the time difference

between ultrasonic pulses traveling with and against the flow of water to determine the flow rate with high accuracy without any moving parts, minimizing mechanical wear and maintenance. Its performance is defined across a wide range of flow rates: from a minimum flow rate (Q1) of 0.064 m3/h essential for detecting small leaks, up to a nominal continuous flow rate (Q3) of 16 m3/h suitable for normal operation. It can even temporarily withstand an overload flow rate (Q4) of approximately 20 m3/h without damage. The meter incorporates a LoRaWAN transmitter that periodically transmits data on the totalized volume, instantaneous flow rate and alarms, guaranteeing remote monitoring for several years.

For accurate readings, the meter should be installed in a straight pipe section following the U5/D3 rule, meaning at least five pipe diameters upstream and three diameters downstream of straight pipe to ensure a stable flow profile. This installation rule helps avoid turbulence or flow distortion caused by nearby bends or valves, ensuring that the water passes smoothly through the measurement zone for precise flow detection.

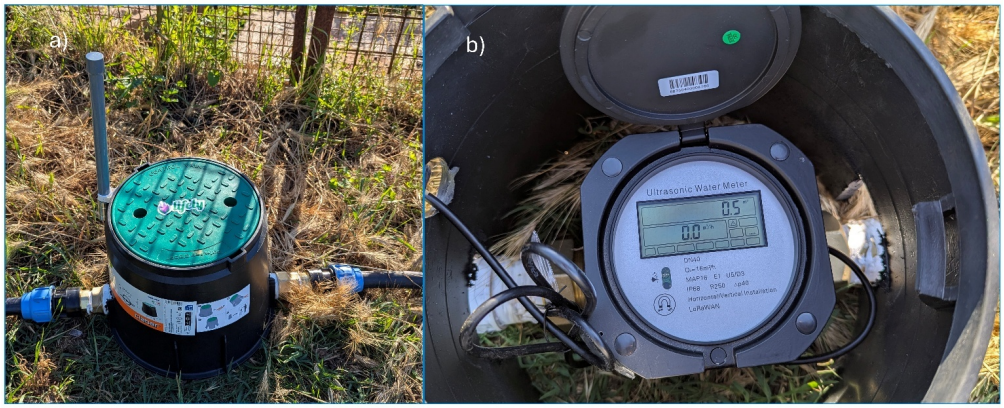

Figure 3.21: (a) Installation of the LoRaWAN ultrasonic water meter within a protective housing connected to the irrigation line (b) An internal view of the ultrasonic flow sensor and the display unit with LoRaWAN communication module.

3.5 Conclusion

This chapter presented the experimental methods, tools, and materials employed throughout the research work. The study was structured around three main experimental activities: the development and testing of two non-invasive leaf-based sensing techniques (infrared spectroscopy and electrical impedance spectroscopy)

on Hydrangea macrophylla plants under outdoor conditions, the deployment of long-term monitoring custom IMU-based petiole sensors developed by KU Leuven in commercial greenhouses, and the practical implementation of the smart irrigation platform within the SPRITZ project at Abinsula company.

The methodologies described here lay the foundation for the subsequent analysis and interpretation of the data, which will be explored in the following chapters.

4

Development of Optical and Electrical Sensors for Non-Invasive Monitoring of Plant Water Status

4.1 Introduction

Building on the physiological background and sensing principles reviewed in chapter 2, as well as the experimental tools and protocols described in chapter 3, this chapter focuses on the application of optical and electrical leaf-based sensing techniques for the non-invasive assessment of plant water status.

In particular, this chapter presents the experimental evaluation of near-infrared spectroscopy (NIRS) and electrical impedance spectroscopy (EIS) as low-cost, leaf-level methods for detecting variations in plant hydration. Both techniques rely on changes in the optical and electrical properties of leaf tissues that are indirectly linked to plant water status, making them suitable for non-destructive and repeated measurements over time.

The experiments were conducted in outdoors under uncontrolled environmental conditions, with plants subjected to different irrigation regimes. The main objective is to assess the capability of NIRS and EIS measurements to discriminate between water treatments and to evaluate the relationship between sensor-derived

parameters and a standard destructive reference method, namely the relative water content (RWC).

This chapter therefore serves as a transition from the theoretical and methodological framework established in the previous chapters to the experimental validation of plant-centric sensing approaches, providing the foundation for the subsequent developments presented in this thesis.

4.2 Methodology and Data Analysis

4.2.1 Relative Water Content (RWC)

The protocols used for this method were described in subsubsection 3.2.2.1. For each measurement, the following parameters were recorded: fresh weight (FW), turgid weight (TW), and dry weight (DW). The relative water content (RWC, %) was then calculated using the standard formula [83] shown in Equation 4.1:

$$\text{RWC } (\%) = \frac{\text{FW} - \text{DW}}{\text{TW} - \text{DW}} \times 100 \tag{4.1}$$

This method was applied to all plants of Figure 3.1 from both treatment groups at three-day intervals throughout the experiment. For each group, the results were expressed as the mean ± standard deviation (SD), summarizing the RWC distribution and variability between well-irrigated and poorly irrigated plants.

4.2.2 Infrared Spectroscopy

During each infrared measurement, the ramp waveform driving the LED increased linearly from 0 V to approximately 5 V, followed by a brief return to 0 V to reset the cycle. As the LED voltage rose, the amount of IR light transmitted through the leaf increased, leading to a corresponding rise in the output voltage from the photodiode. Then, a CSV file was exported from the Analog Discovery 2 (AD2) containing the variation of the photodiode output voltage (V_{pd}), the input generator voltage (V_{gen}), and the cycling time.

The data collected from each daily measurement were organized as a set for each plant. These files were then uploaded to a Google Colab environment for processing.

To calculate the final daily measurement output representing the transmitted light through the leaf, the average photodiode voltage was computed over the active LED range, which is the useful portion of the signal in one cycle (approximately

from 1.25 V to $V_{\max}$). Outside this range, either the LED is not emitting enough light or the signal is saturated. This output, referred to as V_{ph}, was calculated as the Equation 4.2.

$$V_{\text{ph}} = \frac{1}{N} \sum_{i:V_{\text{gen},i} \in [1.25\,\text{V},\, V_{\max}]} V_{\text{pd},i} \tag{4.2}$$

where V_{gen} is the generator voltage driving the LED, V_{pd} is the output of the photodiode, and N is the number of valid samples within the selected range.

To calibrate all the daily measurements, a reference baseline reading (V_{baseline}) was recorded, representing an infrared measurement without a leaf sample (the LED light directly captured by the photodiode, indicating 100% light transmittance). The baseline voltage was calculated similarly to the Equation 4.3.

$$V_{\text{baseline}} = \frac{1}{N} \sum_{i:V_{\text{gen},i} \in [1.25\,\text{V},\, V_{\max}]} V_{\text{pd},i} \tag{4.3}$$

Then, the daily transmitted infrared measurement for each plant was calculated using the Equation 4.4.

$$T_i(\%) = \left(\frac{V_{\text{out},i}}{V_{\text{baseline}}} \right) \times 100 \tag{4.4}$$

Finally, the daily absorption coefficient of each plant was calculated as the complementary portion of the transmitted signal follwing Equation 4.5.

$$A_i(\%) = 100(\%) - T_i(\%) \tag{4.5}$$

All daily absorption coefficients were collected for all plants. Measurements were organized under the well- and poorly-irrigated groups for both experimental phases and normalized by period. A Welch's t-test was conducted to assess the overall difference in normalized absorption coefficients between the well-irrigated and poorly irrigated groups, considering all plants and measurement days. The analysis was performed on flattened data vectors to capture the full distribution of each group.

The relationship between RWC and normalized absorption coefficients was evaluated separately for the two phases of the experiment using multiple regression models. The best-fitting model was selected based on the highest R^2 value.

4.2.3 Modeling of the Electrical Impedance Spectroscopy

For each daily impedance measurement, data including magnitude, phase, and their corresponding frequency columns were recorded in `.csv` files for each plant.

The data were then processed and fitted to a proposed equivalent circuit model (ECM) used to fit the impedance spectra of leaf tissues.

The proposed model is represented in Figure 4.1. It is derived from the Cole-type models reviewed in subsubsection 2.4.1.1, which are widely used to represent the frequency-dependent electrical behavior of biological tissues. In particular, the selected model can be interpreted as a practical adaptation of the Cole model that explicitly accounts for the electrode–leaf interface, which is especially relevant in two-terminal (2T) impedance measurements.

Unlike more complex models such as the double-shell or Hayden models, the present ECM was intentionally chosen as a simplified yet physiologically meaningful representation, suitable for robust parameter estimation under experimental constraints such as limited frequency range, measurement noise, and repeated daily acquisitions.

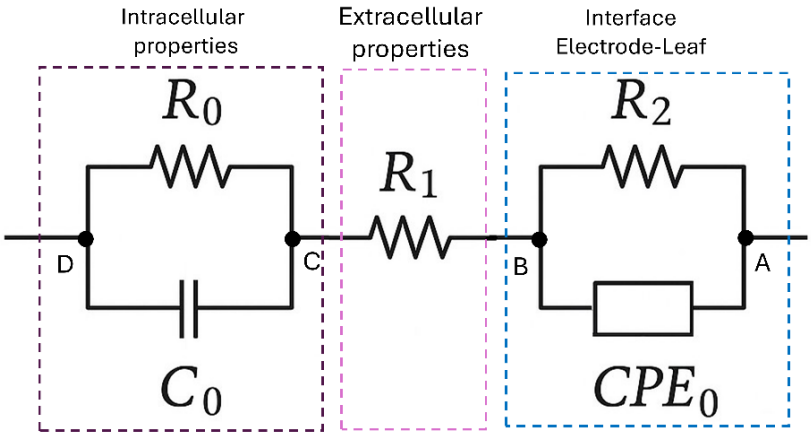

Figure 4.1: Schematic representation of the proposed equivalent circuit model (ECM) used to fit the impedance spectra of leaf tissues. The model consists of two parallel branches (R_0, C_0) and (R_2, CPE_0) separated by a series resistance R_1.

This model was selected based on established bioimpedance literature, including both plant and biomedical applications, where electrical components are commonly associated with biological structures [127, 185, 186, 187, 188]. Each component represents the electrophysiological properties of leaf tissues.

The model consisted of a resistance in series between two parallel branches. The series resistance R_1 is associated with extracellular ionic pathways, capturing conductivity through apoplastic spaces, while the parallel branch (R_0, C_0) captures intracellular properties, with R_0 representing the intracellular resistance and C_0 modeling the cell membrane capacitance. The other branch $(R_2 \parallel \mathrm{CPE}_0)$ was

designed to represent the contact interface between the electrode and the leaf, where R_2 reflects interfacial resistance and CPE_0 accounts for non-ideal capacitive behavior as shown in Equation 4.6 due to surface irregularities, with the phase factor n indicating the degree of non-ideality [127].

$$Z_{\mathrm{CPE}} = \frac{1}{\mathrm{CPE}_0(j\omega)^n} \tag{4.6}$$

Where Z_{CPE} is the impedance of the constant phase element (CPE), CPE_0 is the pseudo-capacitance, ω is the angular frequency, j is the imaginary unit, and n is the phase factor ($0 \leq n \leq 1$).

The daily measured impedance data were exported to Python, and the magnitude $|Z|$ and the phase angle were first converted into complex form following the Equation 4.7 and then fitted to the selected ECM using the `impedance.py` library [189].

$$Z(\omega) = |Z|\Big[\cos\theta + j\sin\theta\Big] \tag{4.7}$$

where $\omega = 2\pi f$ is the angular frequency ($\mathrm{rad\,s^{-1}}$), $|Z|$ is the impedance magnitude, θ is the phase angle, and $j^2 = -1$ is the imaginary unit.

The goal of this analysis was to determine the circuit parameters that best reproduce the measured impedance response of the system across the full frequency range. The fitting procedure sought to minimize the difference between the experimental impedance Z_k and the model-predicted impedance $\hat{Z}_k(\theta)$ over all frequency points k. This was achieved by minimizing the following objective function in Equation 4.8

$$\min_{\theta} \sum_{k} \left[\Big(\Re\{Z_k - \hat{Z}_k(\theta)\}\Big)^2 + \Big(\Im\{Z_k - \hat{Z}_k(\theta)\}\Big)^2\right] \tag{4.8}$$

where $\Re\{\cdot\}$ and $\Im\{\cdot\}$ denote the real and imaginary components of impedance, and $\theta = (R_0, C_0, R_1, R_2, Q, n)$ are the estimated model parameters.

This function calculates the total squared difference between the measured and modeled data in both the resistive and reactive domains. For each frequency, the algorithm evaluates how far the model is from the experimental data, it squares these deviations, and sums them across all frequencies. Minimizing this cost ensures that the optimized parameters accurately reproduce both the magnitude and the phase of the measured impedance spectrum.

To achieve accurate and efficient parameter estimation, a hybrid optimization strategy was implemented. First, a global optimization algorithm was employed using the `SciPy.optimize` library [190] to explore the parameter space broadly

and identify an optimal set of initial guesses, improving convergence speed and avoiding local minima. Subsequently, these global results were refined through a nonlinear least-squares (NLLS) fitting based on the Levenberg–Marquardt (LM) algorithm [191], which iteratively adjusts the parameters to minimize the objective function defined above. The LM algorithm combines the advantages of the Gauss–Newton and gradient-descent methods, allowing rapid convergence near the optimal solution while maintaining stability when far from it.

After convergence, the fitted parameters $(R_0, C_0, R_1, R_2, Q, n)$ were used to simulate the expected impedance response (called the theoretical spectrum) and compared directly with the experimental data to verify how well the model represented the real behavior of the system. Performance of the fit was evaluated visually through Nyquist and Bode plots and quantitatively confirmed using the coefficient of determination (R^2), computed separately for the real and imaginary components of the impedance.

All circuit parameters were extracted for all impedance measurements of all plants. The parameter values were organized under well-irrigated and poorly irrigated groups for both experimental periods and were normalized by period. A Welch's t-test was conducted to assess the overall difference in the normalized impedance parameters between the well-irrigated and poorly irrigated groups, considering all plants and measurement days. The analysis was performed on flattened parameter vectors to capture the full distribution of each group.

Finally, the relationship between leaf water status (RWC) and the fitted circuit parameters was examined separately for the two phases of the experiment using multiple regression models. The best-fitting model was selected based on the highest R^2 value.

4.3 Results and Discussions

4.3.1 RWC Results

The Relative Water Content (RWC) values measured throughout the experiment confirmed the effectiveness of the irrigation treatments in inducing a substantial variation in hydration level between the two plant groups. As shown in Table 4.1, the average RWC values were computed for well-irrigated and poorly irrigated groups every three days during both phases of the experiment (Days 1, 4, 7, 10 before interruption, and Days 13, 16, 19 after interruption). These values are expressed as mean ± standard deviation (SD) and serve to summarize the hydration status of the six *Hydrangea macrophylla* plants over the 20-day period.

In the first phase, plants under well irrigation treatment (Awell, Bwell, and Cwell) maintained high RWC values, consistently above 89%, with only a slight decreasing trend observed over time. In contrast, the poorly irrigated plants (Abad, Bbad, and Cbad) began the first phase with relatively high hydration (average ∼95% on Day 1) but exhibited a noticeable decline, reaching ∼67% by Day 10. This indicates that the effects of water deficit began to manifest, though the impact was still moderate.

In the second phase, following the intentional irrigation interruption, the separation between the two groups became more pronounced. While the well-irrigated group showed a slight reduction in RWC (remaining above ∼81%), the poorly irrigated group experienced a sharp decline, with average RWC values dropping to ∼66% on Day 13 and continuing to fall to ∼33% by Day 19. These values highlight the progressive development of water stress symptoms in the poorly irrigated group as the experiment progressed.

These results confirm that the irrigation strategy effectively induced controlled stress conditions, which offers a solid reference baseline for evaluating the performance and validating the comparisons with the non-destructive sensing methods such as infrared spectroscopy and electrical impedance spectroscopy.

Table 4.1: Summary of the average RWC values on scheduled measuring days for well- and poorly-irrigated groups during both phases. Values are expressed as mean ± standard deviation (%).

Phase	**Day**	**Well-Irrigated (Mean ± SD)**	**Poorly Irrigated (Mean ± SD)**
First phase	1	96.72% ± 1.93%	94.78% ± 2.28%
	4	92.90% ± 2.13%	88.97% ± 1.44%
	7	93.78% ± 0.65%	76.44% ± 3.39%
	10	89.10% ± 3.16%	67.39% ± 15.72%
Second phase	13	82.01% ± 5.51%	66.57% ± 13.23%
	16	84.85% ± 5.80%	45.38% ± 10.57%
	19	81.47% ± 4.78%	33.12% ± 11.54%

4.3.2 Infrared Spectroscopy Results

The temporal evolution of the normalized absorption coefficient for the control and test groups is shown in Figure 4.2. The blue and red curves refer to the average normalized absorption coefficient for the well-irrigated and poorly irrigated plant groups, respectively.

In the initial phase (Days 1–12), the control group exhibited relatively stable normalized absorption values, showing a slight decrease over time but remaining consistently higher than those of the test group. In the second phase (Days 13–20), the normalized absorption values in the poorly irrigated group demonstrated increased variability and continued to decline, reaching the lowest levels by Day 20. Conversely, the well-irrigated group exhibited a decline in the initial days, followed by a modest recovery at the end of the period. It is noteworthy that the ups in the response of the test group correspond to the measures implemented the day after watering the plants, thereby confirming the high sensitivity of this kind of measurement to irrigation events.

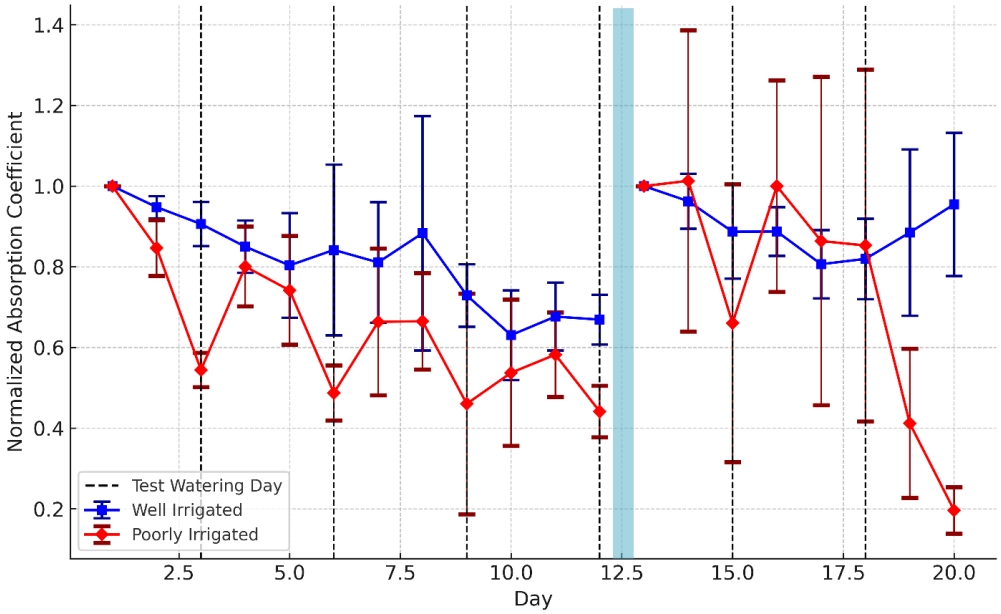

Figure 4.2: Normalized absorption coefficient trends for well-irrigated (blue) and poorly irrigated (red) plant groups over a 20-day experimental period. The standard deviation is also included. Dashed black lines indicate test watering days. A visible gap between Days 12 and 13 indicates a 10-day interruption and a one-week pre-irrigation period to restore initial conditions. Error bars represent standard deviation.

As illustrated in Figure 4.3, the boxplot analysis demonstrates the divergence in absorption responses on the selected Days 2, 7, 12, 14, and 19. Each box represents the interquartile range (IQR), with whiskers indicating variability outside the upper and lower quartiles. Median values are indicated by horizontal lines. The selection of these days is not arbitrary; it is intended to facilitate the analysis

of periods where the gap between the curves for the well- and poorly-irrigated plants was most pronounced.

In the initial phase (Days 2, 7, and 12), the well-irrigated plants exhibited higher and more consistent normalized absorption values, while the poorly irrigated plants demonstrated a decline and greater variability between plant samples. In the subsequent phase, the discrepancy became even more pronounced. By Day 19, the plants in the poorly irrigated group exhibited the lowest values of the entire experiment. This outcome is indicative of the extremely high water stress experienced by these plants. In contrast, the well-irrigated plants demonstrated greater stability, maintaining high normalized absorption values.

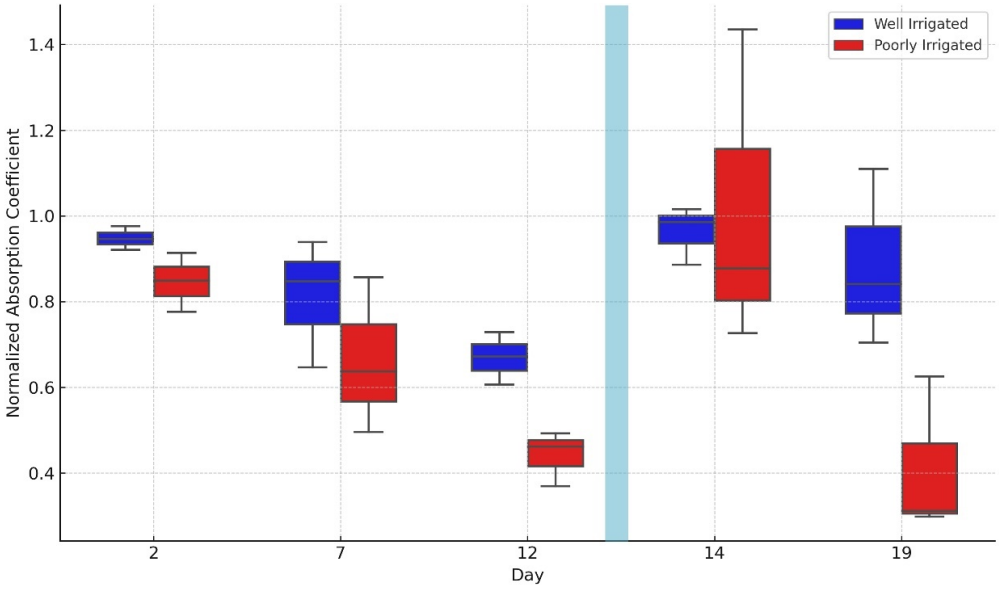

Figure 4.3: Boxplots of normalized absorption coefficients for well-irrigated (blue) and poorly irrigated (red) plants on selected days (2, 7, 12, 14, 19). The shaded region marks the experimental time gap between the two measurement phases. Each box represents the interquartile range (IQR), with whiskers indicating variability outside the upper and lower quartiles. Median values are shown as horizontal lines.

The observed decline in normalized absorption coefficients in water-stressed plants during both phases can be explained by structural changes in leaf tissues during the process of dehydration. A decrease in water content has been shown to reduce leaf thickness and turgor pressure, which in turn leads to a decrease in optical path length and a change in absorption behavior. The quantification of such results is often accomplished by researchers using an Equivalent Water Thickness (EWT) measurement in millimeters. The correlation between the thickness of the

water layer in the leaf and the depth of the absorption features has been well documented [192]. These findings are consistent with previous studies demonstrating that leaf internal structure and moisture content affect optical properties in the near-infrared regions [11, 193]. In addition, the study reported in [194] found that well-hydrated plants exhibited higher values of absorption in the NIR spectrum than plants experiencing water stress. This trend was also observed in the control group during the experiment's initial phase, where the normalized absorption values remained relatively stable and consistently higher than those of the test group.

In the second phase, the normalized absorption coefficients showed unexpected behavior. Between Days 16 and 18, the poorly irrigated plants exhibited high values, followed by a sharp drop, while the well-irrigated group showed lower values with slight recovery at the end. This may be explained with the physiological adaptation response of the plants [195, 196]. The poorly irrigated plants, having already faced two stress periods, may have developed stress memory and temporarily improved tolerance after the one-week irrigation. However, when stress resumed, their sensitivity declined, leading to a reduced response. On the other hand, the well-irrigated plants were not used to stress, so they had a harder time recovering after the interruption. That may explain their initially low IR response and the slight recovery by the end.

A further noteworthy observation in this study was that increases in the normalized absorption coefficients of water-stressed plants frequently occurred on the day following irrigation rather than on the same day. Even though measurements were taken approximately 10 hours after watering, no immediate change was detected. This protracted reaction may indicate that the physiological recovery mechanisms of plants do not occur instantaneously but rather evolve over time. As demonstrated in [197], research findings indicate that xylem embolism significantly reduces stem-specific conductivity in maize plants during daylight hours. However, the plant can recover overnight if sufficient soil moisture is available.

To further develop the study, Welch's t-test was conducted to assess the overall difference in normalized absorption coefficients between the well-irrigated and poorly irrigated groups, considering all plants and measurement days. The analysis was performed on flattened data vectors to capture the full distribution of each group. The selection of this test over the standard Student's t-test was made on the basis that it does not assume equal variances between the two groups and it is more robust when dealing with small sample sizes [198]. The findings demonstrated a statistically significant discrepancy between the two irrigation treatments ($t = 3.79$, $p = 2.69 \times 10^{-4}$), indicating that irrigation level exerts a substantial influence on the optical properties of plant leaves.

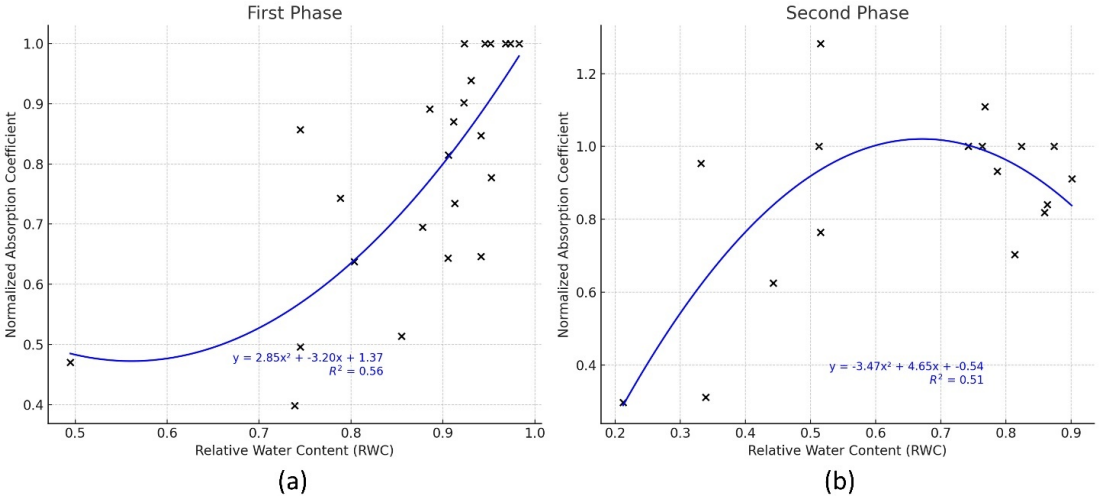

Figure 4.4: Correlation between RWC and normalized absorption coefficient during the two experimental phases. A quadratic model was used to fit the data in both phases. The left panel shows the first phase with a coefficient of determination of $R^2 = 0.56$, and the right panel displays the second phase with $R^2 = 0.51$. Each subplot includes the corresponding regression equation and R^2 value.

The relationship between RWC and the normalized absorption coefficient was assessed separately for the two phases of the experiment using multiple regression models. The best-fitting model in each case was selected based on the highest coefficient of determination (R^2). The infrared spectroscopy method showed a good correlation with the RWC values when a quadratic regression model was applied, yielding R^2 values of 0.56 and 0.51 for the first and second phases, respectively as shown in Figure 4.4.

These results confirm the potential of this non-destructive technique to monitor plant hydration levels. While these R^2 values may appear lower compared to those reported in other studies, for example, the work in [199] achieved a coefficient of determination equal to 0.9899 for the correlation between leaf water content and diffuse reflectance spectra in *Miscanthus*. It is important to highlight that our measurements were conducted in uncontrolled outdoor conditions, where plants were exposed to natural environmental variability. In contrast, the above-mentioned studies were typically performed in controlled environments, which naturally lead to more stable and higher correlations.

4.3.3 Electrical Impedance Spectroscopy (EIS) Results

As illustrated the Bode plots of magnitude and phase in Figure 4.5 and the Nyquist plot in Figure 4.6, the model demonstrates excellent agreement with the experimental data across the full frequency spectrum. This strong fit confirms the model's ability to accurately capture both resistive and capacitive behaviors of the leaf–electrode system. These results support the suitability of the proposed circuit for characterizing leaf tissue impedance under different hydration states, providing a reliable tool for monitoring plant water status through non-invasive electrical measurements.

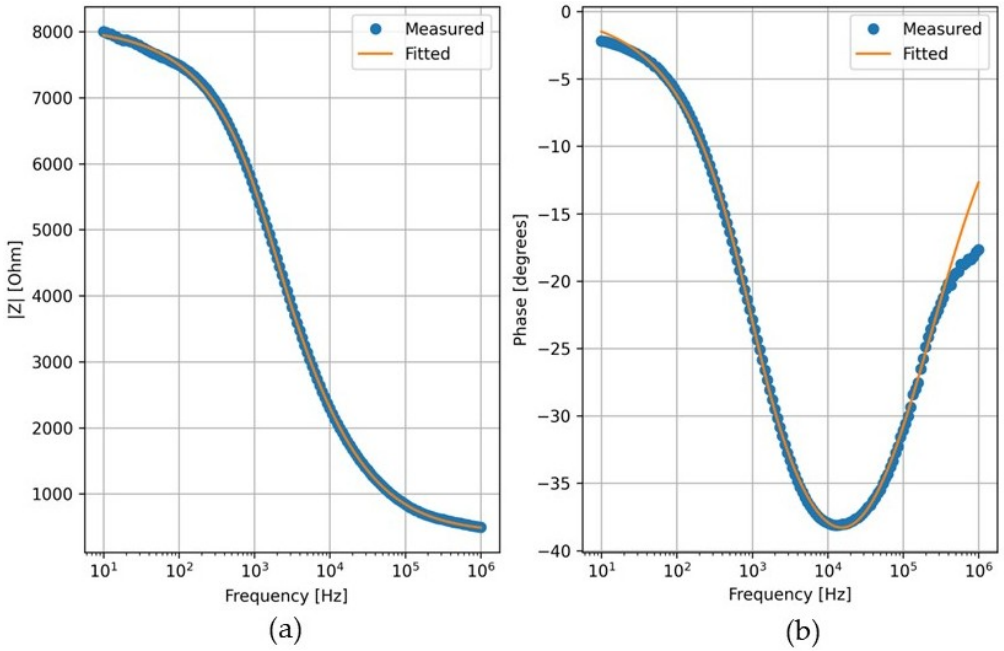

Figure 4.5: Bode plots showing the measured (blue dots) and fitted (orange line) impedance data from a representative leaf sample: (a) magnitude of impedance ($|Z|$) versus frequency; (b) phase angle (degrees) versus frequency. The good fitting quality demonstrates the suitability of the equivalent circuit model across the measured frequency range.

The extracted normalized electrical parameters from the fitted equivalent circuit model are presented in Figure 4.7, showing distinct trends in response to the irrigation treatments over the 20-day monitoring period.

In particular, the normalized R_0 in Figure 4.7d demonstrated a progressive increase in the poorly irrigated group, starting around Day 6 and peaking around Day 12, followed by a decline during the second phase. This rise in R_0 is likely

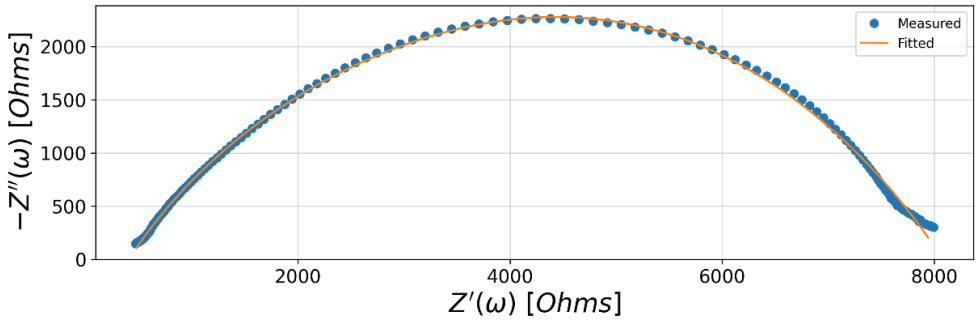

Figure 4.6: Nyquist plot ($-Z''(\omega)$ vs. $Z'(\omega)$) of the complex impedance spectra from a representative leaf, comparing measured (blue dots) and fitted (orange line) data. The close overlap between measured and modeled data confirms the fitting accuracy of the proposed circuit.

related to reduced ionic mobility within plant tissues due to water stress [131]. As water is the primary medium for ion transport, its reduction increases tissue resistance and hinders current flow [200].

Similarly, the normalized C_0 parameter in Figure 4.7e, which reflects the capacitive behavior of cell membranes, showed a clear and immediate increase in the well-irrigated plants at the beginning of both phases, while remaining consistently lower in the poorly irrigated group. This trend may be attributed to turgor pressure differences, where water loss can impair membrane integrity and reduce their capacity to store charge. This observation aligns with studies on chili pepper and tomato leaves, where higher leaf moisture was associated with higher dielectric constant values and, consequently, higher capacitance readings [201].

In contrast, the normalized R_1 parameter in Figure 4.7c showed moderate variations across both groups, without a clear separation during the first phase. However, a decreasing trend was observed in the poorly irrigated group during the second phase. For the remaining parameters, R_2 and CPE_0, no substantial group separation was observed in the first phase in Figure 4.7a and Figure 4.7b. In the second phase, while CPE_0 remaining variable with no clear difference between groups, R_2 showed some separation, with lower values in the poorly irrigated plants.

Overall, these findings highlight the sensitivity of impedance-derived parameters, especially R_0 and C_0, to changes in plant water status, confirming their potential as reliable indicators of leaf hydration.

Welch's t-test was performed to statistically compare the normalized impedance parameters between well-irrigated and poorly irrigated plant groups across all mea-

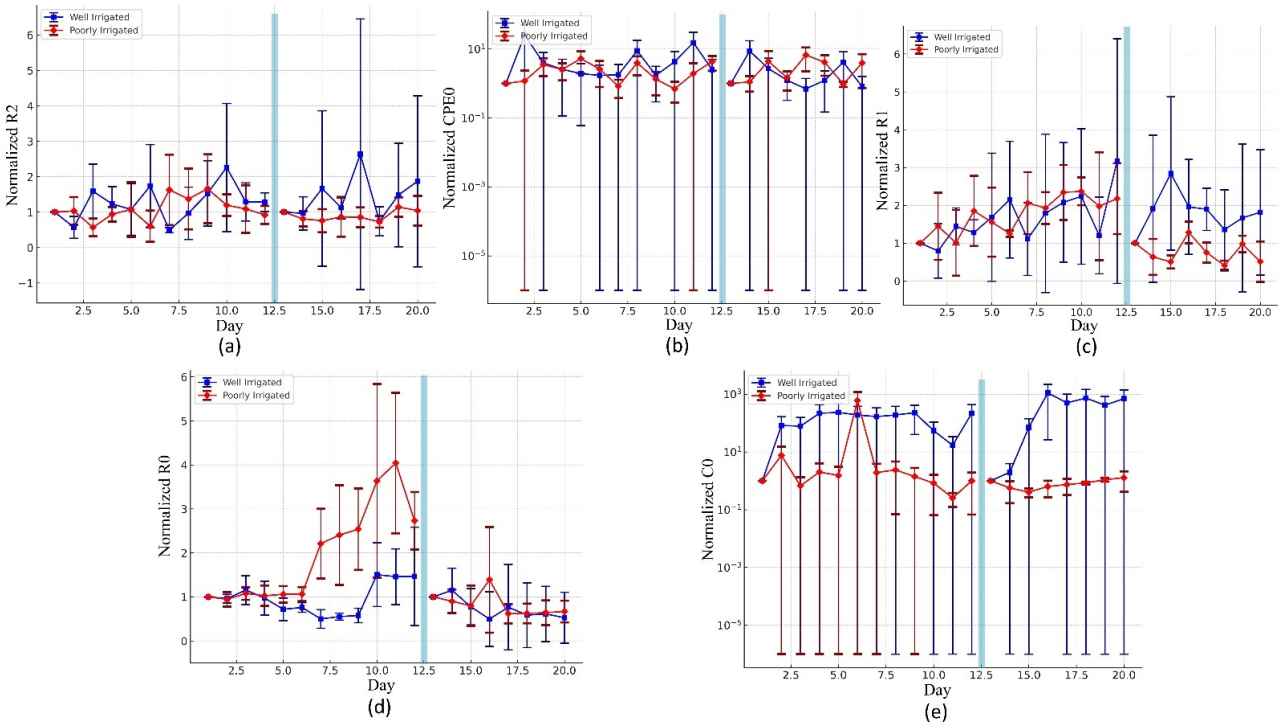

Figure 4.7: Temporal evolution of the normalized parameters extracted from the equivalent electrical circuit over the 20-day experimental period for well-irrigated (blue) and poorly irrigated (red) plant groups: (a) R_2; (b) CPE_0; (c) R_1; (d) R_0; (e) C_0. A visible gap between Days 12 and 13 indicates a 10-day interruption and a one-week pre-irrigation period to restore initial conditions. Data points represent group means, and error bars indicate standard deviations. Among all parameters, R_0 and C_0 revealed distinct separation between the treatments in both phases.

surement days. Each impedance parameter (R_0, C_0, R_1, R_2, and CPE_0) was analyzed independently using a two-tailed test to assess whether significant differences existed in the mean values between the two irrigation treatments.

The results, summarized in Table 4.2, revealed that only R_0 and C_0 exhibited statistically significant differences between the two groups at a threshold of $p < 0.001$. Specifically, R_0 showed a strong negative t-statistic ($t = -3.7437$, $p = 0.0003$), while C_0 displayed a positive t-statistic ($t = 3.4003$, $p = 0.0010$), suggesting that both parameters respond sensitively to changes in plant water status. On the other hand, the parameters R_1, R_2, and CPE_0 did not reach statistical significance ($p > 0.05$), which could be attributed to lower sensitivity to water stress conditions in these specific components.

To assess the relationship between RWC and the most promising impedance-

Table 4.2: Summary of Welch's t-test results conducted between well-irrigated and poorly irrigated plants for each normalized parameter. Significance threshold set at $p < 0.001$.

Normalized Parameter	**T-statistic**	**P-value**	**Significant ($p < 0.001$)**
R_0	-3.7437	0.0003	Yes
C_0	3.4003	0.0010	Yes
R_1	1.7628	0.0810	No
R_2	1.8273	0.0714	No
CPE_0	1.2747	0.2069	No

derived parameters (R_0 and C_0), several regression models were tested. However, the resulting determination coefficients (R^2) were too low to indicate any meaningful statistical correlation. This suggests that, under the current experimental conditions, the relationship between impedance parameters and RWC may not be linear or have a direct functional correlation. It is likely influenced by additional factors such as leaf structure and electrode contact variability.

Although the results are promising, there are still some issues that need to be addressed to improve the system's performance.

For impedance spectroscopy, using a two-electrode setup may have reduced the accuracy of the measurements because of the contact resistance between the leaf and the electrodes. To solve this, a four-electrode configuration, as used in [173], is recommended. This approach can reduce errors caused by contact impedance and improve the reliability of the data. It was also noticed that keeping the custom electrodes attached to the leaf for a long time could damage the tissue. Because of this, new electrodes had to be applied each day, which may have introduced variability, particularly affecting the stability of fitted parameters such as CPE_0 and C_0, and contributed to the large standard deviations observed in these normalized values. Developing bioelectrodes that are more compatible with the leaf's surface structure could offer a promising solution, as suggested in [188, 202].

4.3.4 Discussions

For infrared spectroscopy, one of the main challenges was the influence of ambient light, especially in outdoor conditions. Background light can interfere with the readings, so improving light shielding or applying correction methods to reduce this interference would help make the measurements more accurate.

To further improve the study, it is important to increase the number of samples

in each group and take multiple measurements per plant, possibly at different points on the same leaf. This would help reduce variability and better represent the overall water status of the plant.

The study should also be extended to various crop types, such as tomatoes and grapevines, to verify whether the approach works well in other contexts. Finally, continuous monitoring of in-field environmental parameters such as temperature, humidity, and light intensity should be incorporated to improve data interpretation and quantify the impact of these factors on plant responses.

4.4 Conclusion

The present study aimed to develop and evaluate two non-invasive sensor systems, infrared (IR) spectroscopy and electrical impedance spectroscopy (EIS), for directly assessing plant water status from leaf tissues. Both sensors successfully differentiated between well-irrigated and poorly irrigated *Hydrangea macrophylla* plants under uncontrolled outdoor conditions, validating their performance against the traditional reference method of relative water content (RWC).

Among the parameters obtained from impedance measurements, the normalized intracellular resistance (R_0), the cell membrane capacitance (C_0), and the normalized absorption coefficient demonstrated significant differences between the two irrigation treatments, as confirmed by Welch's test. The IR sensor demonstrated a good correlation with RWC, yielding determination coefficients of $R^2 = 0.57$ and $R^2 = 0.51$ for the first and second phases of the experiment, respectively. In contrast, the impedance sensor did not exhibit a clear functional correlation with RWC, likely due to measurement complexity and confounding factors such as contact impedance and tissue heterogeneity.

Despite these promising results, several limitations were identified. The main challenges include the limited conformity of the custom electrodes with the leaf surface and the strong influence of ambient sunlight on IR measurements. These findings highlight the need for further refinement of both sensing systems to improve their precision and reliability. Future work should focus on enhancing electrode design, minimizing optical interference, and validating the sensors under a wider range of environmental conditions to enable their effective application in real-world plant monitoring and irrigation management.

5

Optimization and Testing of an Innovative Wireless IMU-Based Sensor for Real-Time Monitoring of Plant Movements

5.1 Introduction

Plant movement has been identified as a significant indicator of physiological responses to environmental conditions. Changes in the orientation of leaves or petioles have been shown to reveal early signs of abiotic stress, such as drought, heat, or suboptimal lighting [140]. However, traditional observation techniques are constrained by limitations related to occlusion, cost, and data processing complexity.

Recently, digital sensors such as inertial measurement units (IMUs) have emerged as a reliable tool for detecting stress-induced leaf movements in real time. These movements include epinasty (downward bending) in tomato plants and hyponasty (upward bending) in other species [14]. Such sensors, designed to be attached directly to leaves or petioles, enable continuous and non-invasive monitoring of plant movements under real greenhouse conditions.

This chapter presents the work conducted during my research stay at KU Leuven University within the DRAMCO research group. The main objectives were to reduce the energy consumption of their developed IMU-based petiole sensor and to analyze the experimental data collected from two partner greenhouses cultivating tomato plants. The study aimed to investigate whether petiole movements could be used to predict artificial lighting conditions and, more broadly, to understand how tomato plants respond to different environmental treatments.

5.2 Methodology and Data Analysis

5.2.1 Optimization of Energy Consumption of the IMU-Based Sensor

The power optimization strategy was fundamentally guided by a quantitative error analysis, which assessed the impact of progressively reducing the number of raw IMU samples from the original 120 down to 100, then 80, and finally 60 samples. As explained in subsection 3.3.2, each step of the process was repeated three times (first, second, and third measurement) and was reapplied on two different initial positions for validation: a 90° inclined position and a flat position.

The quaternion data (w, x, y, z) of each event were collected in Excel files together with their timestamps using the serial monitor. A global orientation error was computed directly in quaternion space for the first, second, and third measurement (obtained with the reference implementation of the sensor), using the Euclidean distance between the mean quaternions of the reduced-sample sets (each time 10 samples were reduced) and the reference dataset (120 samples):

$$\text{Error} = \sqrt{(w_n - w_{\text{ref}})^2 + (x_n - x_{\text{ref}})^2 + (y_n - y_{\text{ref}})^2 + (z_n - z_{\text{ref}})^2} \tag{5.1}$$

This formulation provides a comprehensive measure of the orientation deviation in four-dimensional quaternion space, ensuring that all rotational components are considered simultaneously.

All datasets were imported into Python, and the quaternions were converted to Euler angles (roll, pitch, and yaw) using the `SciPy.spatial.transform.Rotation.from_quat()` function, which expresses three-dimensional orientation in degrees. For each measurement file, the mean quaternion was computed to obtain a representative orientation, and this average was then transformed into Euler angles for subsequent comparison.

Within each trial, the dataset with 120 samples was used as the reference orientation, representing the baseline accuracy. The reduced-sample datasets (100, 80, and 60 samples) were compared to this reference to quantify the deviation introduced by sample reduction. The orientation error for each Euler component was calculated as the absolute difference between the reference and the reduced-sample values as shown in Equation 5.2.

$$\Delta\text{Euler} = |\text{Euler}_n - \text{Euler}_{\text{ref}}| \tag{5.2}$$

The resulting angular errors (ΔRoll, ΔPitch, ΔYaw) were analyzed and plotted as functions of the number of samples for each measurement repetition. These plots enabled the identification of the sampling threshold at which the error becomes negligible relative to the reference.

5.2.2 In-depth Analysis of The Two Greenhouse Experiments

As discussed before in subsection 3.3.3, the experiments were deployed in two different greenhouse partners. In this section, it will be explained how data was collected from sensors and environmental parameters of both greenhouses and then processed to visualize and discuss results in the next section. Finally, the data analysis with the integration of machine learning was mentioned to predict the plant petiole movement across the variation of lighting exposure.

The environmental data were provided separately by the greenhouse partners in the form of CSV files. For the first experiment, the environmental dataset contained the timestamps of 5-minute intervals for the PAR (Photosynthetically Active Radiation) values, temperature, and relative humidity for both Set 1 and Set 2. However, the environmental data for the second experiment was less structured, requiring more organization and data conversions to obtain ready meaningful parameters. The data provided were taken at 5-minute intervals and included different parameters such as percentage of artificial LED lighting intensity applied to Set 4, instantaneous natural solar radiation ($\text{W} \cdot \text{m}^{-2}$), accumulated solar radiation energy over time ($\text{J} \cdot \text{cm}^{-2}$), and additional data related to substrate weight and daily drainage percentages.

At this point, the analysis focused on converting the raw light measurements into biologically relevant photosynthetic active radiation (PAR) values to align with the provided data of the first experiment (Set 1 and Set 2). This conversion was a two-step process: first, the conversion of global solar radiation ($\text{W} \cdot \text{m}^{-2}$) to PAR ($\mu\text{mol} \cdot \text{m}^{-2} \cdot \text{s}^{-1}$) was performed using a conversion factor of

4.6 μmol $\cdot$ s^{-1} $\cdot$ W^{-1}, a standard value recommended for clear-sky conditions [103]. The definition of PAR in terms of photon flux density (μmol $\cdot$ m^{-2} $\cdot$ s^{-1}) is far more relevant than its definition in terms of irradiance (W $\cdot$ m^{-2}), as it induces a lower systematic error ($\pm$6% versus $\pm$16%) when the spectral composition of the light varies (sun, blue sky, artificial lamps). Therefore, to accurately quantify the effect of PAR on a plant's photosynthetic activity, the measurement of incident quantum flux is the preferred choice, as it provides a better approximation of the true potential of light to stimulate photochemical reactions [203]. Second, for the Energy-Controlled Lighting group (Set 4), the LED intensity (given as a percentage) was also converted to PAR by scaling the system's maximum output of 169 μmol $\cdot$ m^{-2} $\cdot$ s^{-1}.

The total PAR for Set 4 was then calculated as the sum of the sunlight and LED components, whereas for the Control group (Set 3), the total PAR was derived only from the sunlight source.

Daily water uptake calculation

For additional investigations about the effect of photosynthetically active radiation on water consumption, the daily water uptake values were calculated for Set 3 and Set 4, since the provided data contained the substrate weights (recorded every 5 minutes) and the daily drainage percentages. The idea is to measure water loss and added water due to irrigation by assessing the weight changes of the substrate at each timestamp.

Water loss calculation. Only negative weight changes (indicating water loss) were summed daily as follows in Equation 5.3.

$$\Delta W_i = W_i - W_{i-1}, \qquad \text{where } \Delta W_i < 0 \tag{5.3}$$

Irrigation calculation. Similarly, only the positive weight changes (indicating irrigation events) were summed daily as follows in Equation 5.4.

$$\Delta W_i = W_i - W_{i-1}, \qquad \text{where } \Delta W_i > 0 \tag{5.4}$$

Daily plant water uptake estimation. Finally, the daily plant water uptake for Set 3 and Set 4 was calculated using the Equation 5.5 and Equation 5.6,

respectively.

$$\text{Uptake}_{\text{Set3}} = \text{WaterLost}_{\text{Set3}} - \left(\frac{\text{Irrigation}_{\text{Set3}} \times \text{Drainage}\%_{\text{Set3}}}{100}\right) - (\text{Irrigation}_{\text{Set3}} \times 0.10) \tag{5.5}$$

$$\text{Uptake}_{\text{Set4}} = \text{WaterLost}_{\text{Set4}} - \left(\frac{\text{Irrigation}_{\text{Set4}} \times \text{Drainage}\%_{\text{Set4}}}{100}\right) - (\text{Irrigation}_{\text{Set4}} \times 0.15) \tag{5.6}$$

The last term in each formula accounts for estimated plant evapotranspiration based on each experimental assumptions. The estimated plant evapotranspiration for Set 3 corresponds to 10% of the daily available water, while for Set 4 it is estimated by 15%. This difference is attributable to greater light exposure in Set 4, which increased evaporation.

IMU data acquisition and preprocessing

The experiments were deployed in two different greenhouse partners. Each petiole sensor module (for more details, see subsection 3.3.1) was attached to a tomato plant and recorded plant movement data in the form of quaternion measurements. The sensor operates in duty-cycled mode by performing and recording three consecutive measurements approximately every 15 minutes, followed by a LoRa 2.4 GHz data transmission to a local gateway installed within the greenhouse. This gateway acts as a bridge between the wireless sensor network and the cloud infrastructure, *The Things Network* (TTN). TTN provides reliable data transmission and initial storage, enabling real-time access to sensor measurements for authorized project partners. In parallel, all raw sensor data are securely archived on a private database server maintained by the DRAMCO research group. The storage system enables authorized users to retrieve complete datasets by specifying the sensor ID and desired date range. The downloads are provided in CSV format.

The raw sensor data for each set were extracted from the recorded database with the period adjusted to correspond precisely to the two experimental campaigns. The downloaded datasets included: quaternion measurements (w, x, y, z) capturing plant movement dynamics, timestamps synchronized with the sensor acquisition times, and sensor identification information.

To convert these quaternion measurements into interpretable angular movement data, a custom Python script was applied, utilizing the SciPy spatial transformation library (`Rotation.from_quat`). The function accurately transforms the quaternion data into Euler angles representing the Pitch (X-axis rotation), Roll (Y-axis rotation), and Yaw (Z-axis rotation). The Euler angles obtained were

used to investigate petiole orientation and evaluate plant movement patterns. An illustration of the petiole's Euler angle orientations in Figure 5.1.

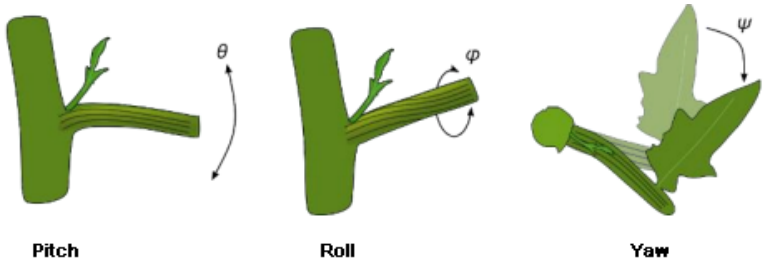

Figure 5.1: Schematic showing the Euler angle orientations (roll, pitch, yaw) of a plant petiole [14].

The data analysis for each set was conducted independently in the Google Colab environment, establishing a robust pipeline for processing, synchronizing, and modeling the orientation signals collected from the IMU-based petiole sensors. The main objective was to investigate the relationship between plant petiole movement and environmental light conditions by linking the sensor-derived orientation data with photosynthetically active radiation (PAR) measurements.

The first day of IMU data acquisition was excluded to eliminate initialization artifacts. To ensure that the measurements did not contain unnatural jumps or discontinuities, a signal correction procedure was implemented. This procedure aimed to eliminate artifacts while preserving the natural circadian patterns of petiole orientation. A customized stepwise correction function was applied to each series of Euler angles. Its role was to identify and remove abrupt jumps in the signal exceeding a defined threshold of 5 degrees. The function operated iteratively; it detectes sudden variations above the threshold, applies a cumulative offset to correct the signal, and thus preserves continuous and realistic movement patterns over time.

Because the raw datasets were recorded using internal transmission delays, the actual timestamps were reconstructed based on the recorded delay field. Each group of three consecutive measurements (with delays of 0, 5, and 10 minutes) was reassigned corrected timestamps, ensuring that the final time series followed a uniform sampling interval. Incomplete or inconsistent batches were discarded.

To associate orientation data with environmental conditions, the processed IMU datasets of each set were merged with the corresponding PAR measurements recorded in $\mu\text{mol} \cdot \text{s}^{-1} \cdot \text{m}^{-2}$. Other environmental parameters (such as temperature or humidity) were intentionally excluded to concentrate the analysis on light-induced petiole responses. A nearest-neighbor temporal merger was performed

to synchronize each IMU record with the closest PAR reading. In addition to PAR, temporal features were extracted from each timestamp to capture diurnal patterns: the time of day was expressed as a continuous hour value and further encoded using its sine and cosine components (*sin_time*, *cos_time*) to represent the cyclic nature of daily light variation.

Subsequently, a machine-learning analysis was performed to evaluate the predictability of petiole orientation from environmental inputs. Three regression algorithms with complementary approaches were used: Random Forest (a robust tree-based model), XGBoost (a high-performance boosted model for structured data), and SVR (a model suited to non-linear relationships on small datasets). Each model was trained independently for each sensor data and for each Euler component (roll, pitch, yaw). The feature set consisted of *PAR_Set*, *sin_time*, and *cos_time*, while the target variable corresponded to one of the Euler angles to be predicted. The datasets were randomly split into a training set (70%) and a testing set (30%). Each model was trained with its default parameters, and its performance was quantified using two metrics: the coefficient of determination (R^2), measuring the proportion of variance explained, and the mean absolute error (MAE, in degrees).

5.3 Results and discussions

Results of the Energy-Consumption Optimization

The initial evaluation, summarized in Figure 5.2, presents the variation of quaternion mean error in % as a function of the number of IMU samples considered for averaging, under two distinct orientations of the sensor module: flat position (left) and 90° position (right).

In both configurations, the error was computed as the Euclidean distance between the mean quaternion obtained using a reduced number of samples and the reference mean quaternion calculated from the complete 100-sample dataset with the exclusion of the first 20 samples. Each curve represents a different measurement repetition (first, second, and third measurement).

For both orientations, a clear decreasing trend of error with the increase in sample number can be observed. This confirms that the accuracy of the estimated mean orientation improves as more samples are included in the averaging process. When only a few samples were used (below 20–30), the deviation from the reference mean was significantly larger, especially for Measurement 1. As the sample

count increased beyond approximately 80, the error approached zero, demonstrating convergence of the mean quaternion toward a stable orientation estimate.

The overall magnitude of the error was slightly higher in the 90° position (approximately 30% for the first 20 samples) compared with the flat orientation (approximately 20% for the first 20 samples) for the first measurement, suggesting that this configuration was more affected by sensor bias or alignment uncertainties. whereas subsequent measures remained stable even with fewer samples, highlighting the influence of the IMU's internal stability period. This established that for a stabilized sensor, sample reduction was a viable path to energy savings.

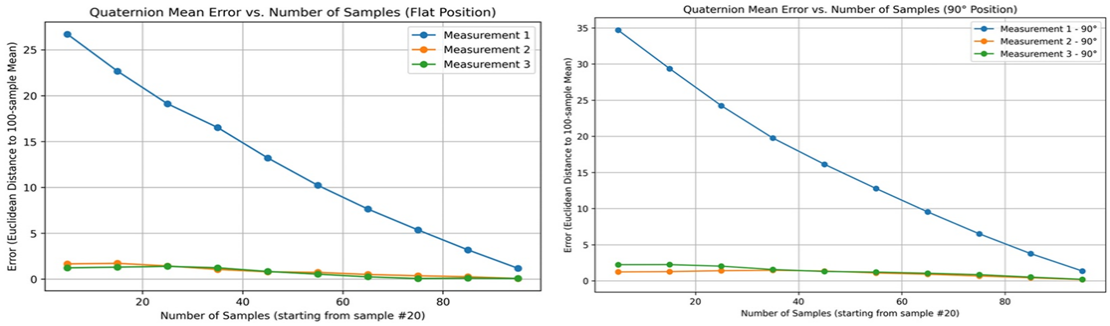

Figure 5.2: Euclidean error between quaternion averages with reduced samples and the 120-sample reference for flat (left) and 90° (right) sensor positions. Measurements 2 and 3 demonstrate low error even with reduced samples, while Measurement 1 shows larger error

Figure 5.3 and Figure 5.4 illustrate the evolution of the Euler angles Roll (X), Pitch (Y), and Yaw (Z) over time for the three repeated measurements with the original implementation (120 samples) when it is positioned respectively at 0° (flat configuration, Figure 5.3) and 90° (vertical configuration, Figure 5.4). Each subplot shows the evolution of a specific Euler angle as a function of elapsed time (measurement duration) for a single measurement repetition, enabling direct comparison of sensor-response stability and noise levels across trials.

In Figure 5.3 of the flat position, the roll angle exhibits a gradual and smooth decreasing trend across time, particularly evident in Measurement 1, indicating a slight drift or slow mechanical relaxation during the acquisition period. The pitch and yaw angles remain nearly constant, with minimal variations, confirming high short-term stability of the IMU under static conditions. The small discrete jumps observed in some measurements are likely due to the sensor's finite digital resolution and quantization of the data stream.

In Figure 5.4 of the 90° position, the roll component remains close to −93°,

consistent with the expected orientation shift of approximately 90° compared with the flat case. The pitch and yaw signals show small oscillations, with slightly higher variability than in the flat configuration, suggesting that the vertical orientation is more sensitive to external perturbations such as magnetic field interference or residual sensor noise. Nevertheless, the mean values remain stable over time, confirming that the module accurately preserves its orientation during the measurement sequence.

Overall, these results demonstrate that the quaternion-to-Euler conversion yields stable and repeatable angle estimations in both configurations. However, a pronounced phenomenon was observed: a large difference in elapsed time between the first measurement and the subsequent measurements, with the first measurement taking 9 s and the subsequent measurements only 2.5 s, when taken in the flat position. Similarly, in the 90-degree position, the elapsed time for the first measurement equals to 15 s while for the subsequent measurements it's equal to only 2.5 s. These results suggest that the IMU requires a longer period of time when affecting measurements directly after powering on, to stabilize its internal filtering and sensor fusion processes. Once stabilized, the subsequent measurements deliver more consistent orientation measurements with shorter time, and even with fewer samples as shown in next section.

Figure 5.5 illustrates the angular error calculated for the three Euler components Roll (X-axis), Pitch (Y-axis), and Yaw (Z-axis) as a function of the number of IMU samples considered (60, 80, and 100) for three measurement repetitions. In each case, the angular error is the absolute difference between the orientation estimated with a reduced number of samples and the reference orientation obtained from the full 120-sample dataset.

For all axes, the general trend indicates that the angular error decreases as the number of samples increases, confirming that a higher sampling count improves orientation stability and accuracy. The most pronounced variations are observed in the Roll and Pitch components of the first measurement, where the error reaches up to approximately 4° and 0.4°, respectively, when only 60 samples are used. These errors decrease significantly as the sample count approaches 100, showing convergence toward the baseline value. In contrast, the second and third measurements maintain consistently low error levels ($< 0.5°$) across all sampling configurations, demonstrating better repeatability and less sensitivity to sample reduction.

For the Yaw component, all trials show very small deviations (below 0.3°), confirming that this axis is less affected by sampling reduction under static conditions. The minor fluctuations observed may be attributed to the residual noise produced from the magnetometer or from the environmental magnetic disturbances.

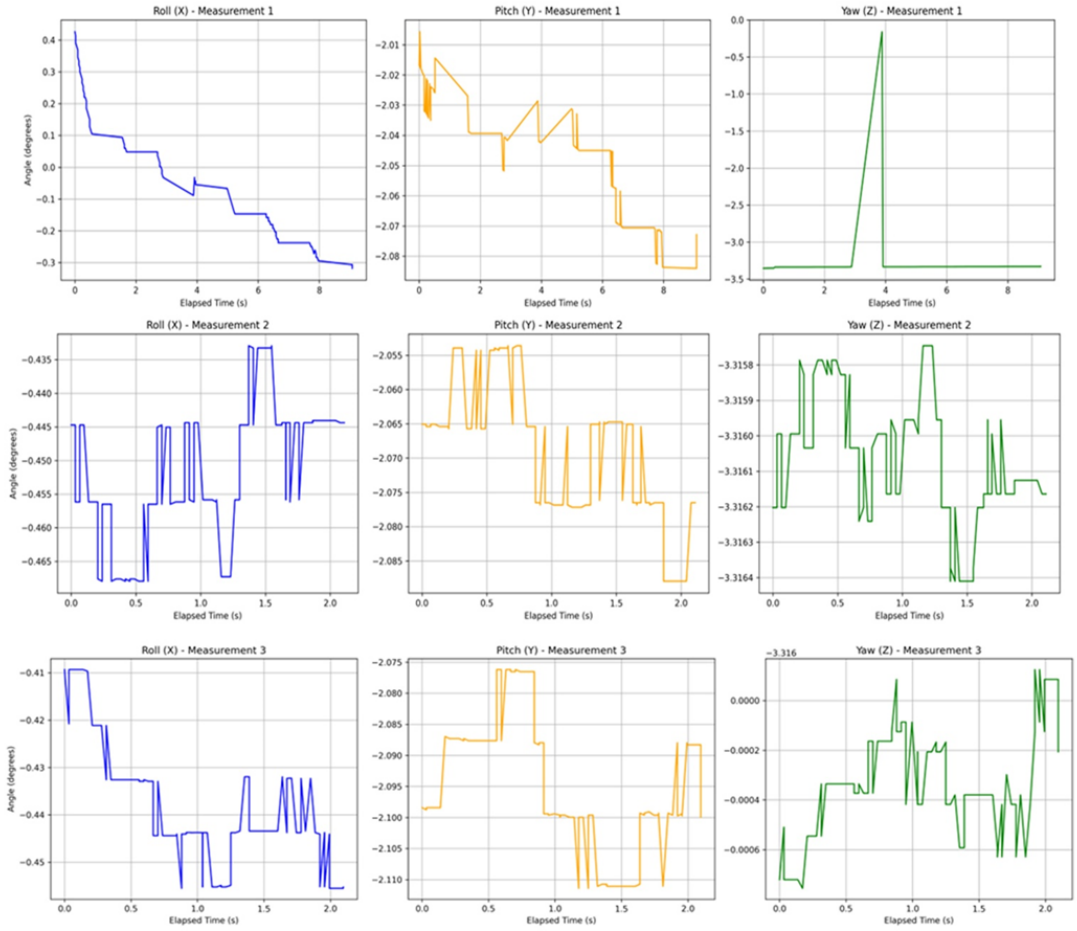

Figure 5.3: Evolution of Roll, Pitch, and Yaw angles during the three consecutive measurements of the IMU taken with the original implementation when the sensor is positioned at flat position.

This direct comparison clearly demonstrates that while the error was unacceptably high for the 60-sample case, particularly for the roll axis, it became acceptably low and stable when 80 samples were used across all axes. The root cause of the initial instability observed in the first measurement was visually confirmed and explained in Figure 5.3 and Figure 5.4, which highlighted the pronounced drift and extended duration of the first acquisition compared to the subsequent ones.

Taken together, this comprehensive analysis, from quantitative error evaluation to axis-specific and temporal behavior, provides a solid empirical basis for selecting the 80-sample configuration as the optimal trade-off. This setting offers substantial energy savings while maintaining angular errors within an acceptable range for

accurate and stable orientation estimation.

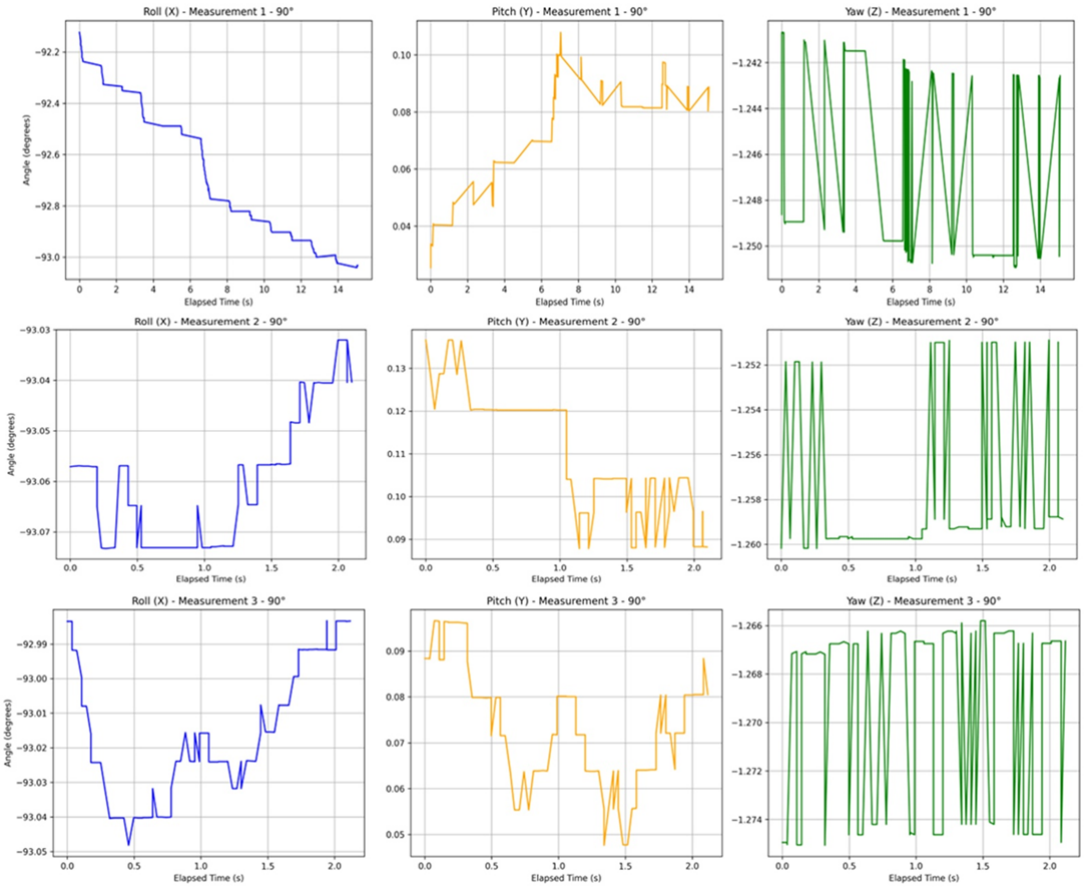

Figure 5.4: Evolution of Roll, Pitch, and Yaw angles for the three consecutive IMU measurements taken with the original implementation when the sensor is positioned at 90°.

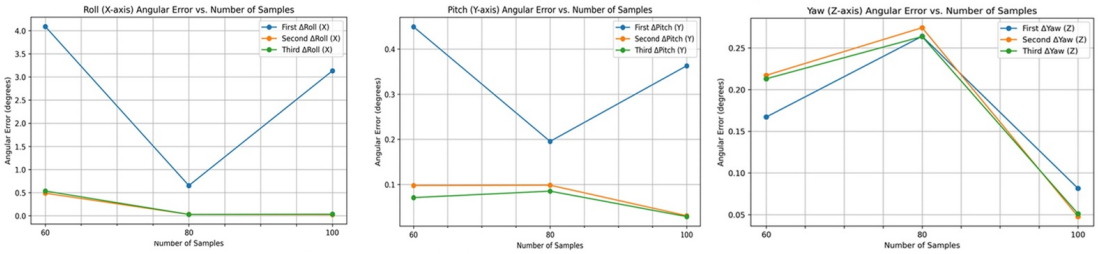

Figure 5.5: Angular errors in (Roll, Pitch, Yaw) relative to the 120-sample reference measurement for different sample reductions at a 90° sensor position.

Table 5.1 summarizes the average energy consumption per operational cycle of the IMU-based sensor, highlighting the contribution of each process before and after the sampling optimization (reducing the sample count from 120 to 80). This optimization maintained acceptable angular accuracy and yielded a clear reduction in overall energy usage.

The energy required for a single IMU measurement dropped from 4.16 μWh to 2.91 μWh, while the combined measurement, supercapacitor charging, and LoRa transmission phase was reduced from 37.48 μWh to 36.23 μWh. The sleep phase remained constant at 13.80 μWh, as it was unaffected by the sampling adjustment. Consequently, the total average energy per complete operating cycle decreased from 87.20 μWh to 83.45 μWh, corresponding to an energy saving of approximately 4.3%.

Although this gain may seem modest in relative terms, its impact on the sensor's autonomy is significant. As demonstrated in Table 5.1, the theoretical autonomy of the sensor, powered by a 1.2 Ah lithium-thionyl chloride (LTC) battery at 3.6 V battery, increases from 1.4 years to 1.48 years, extending its operational duration from 515 days to 539 days, providing an additional 24 days of autonomous operation. This increase is crucial for long-term greenhouse deployments, where maintenance for battery replacement is costly and disruptive.

Table 5.1: Average energy consumption per process before and after sampling optimization.

Process	**Average energy consumption (μWh)**	**Average energy consumption (optimized) (μWh)**
Single IMU measurement	4.16	2.91
Sleep between IMU measurements	13.80	13.80
Single IMU measurement + supercap charging + LoRa transmission	37.48	36.23
Total per cycle	**87.20**	**83.45**

The choice of 80 samples thus stands as the optimal compromise between metrological precision and energy efficiency, ensuring the system's viability for continuous crop monitoring over complete growth cycles.

Results of the Analysis Conducted in Greenhouses

Figure 5.6 illustrates the daily evolution of photosynthetically active radiation (PAR) measured for Set 1 (blue curve) and Set 2 (red curve) within the greenhouse environment during the first experiment. The PAR values, expressed in (μmol s^{-1} m^{-2}), represent the instantaneous intensity of light available for photosynthesis as a function of time expressed in hour.

A distinct difference in light exposure can be observed between the two sets. Set 2 shows consistently higher PAR values throughout the photoperiod, reaching peak levels of approximately 800 μmol s^{-1} m^{-2} around midday, whereas Set 1 peaks near 500 μmol s^{-1} m^{-2} during the same interval. This indicates that Set 2 was positioned under a more intense lighting regime corresponding to supplemental lighting from LED lamps while Set 1 operated just under natural light conditions.

The temporal pattern of both curves follows the expected diurnal course, with light intensity increasing after dawn, reaching its maximum near solar noon, and gradually decreasing toward evening. The extended plateau of Set 2 during early morning and late afternoon further confirms the contribution of artificial lighting, which prolongs the effective illumination period to more than 8 hours compared to Set 1.

These results validate the environmental differentiation imposed during the experiment and confirm that the two sensor sets were exposed to clearly distinct light regimes. Such variation in PAR is essential for interpreting subsequent analyses of plant responses.

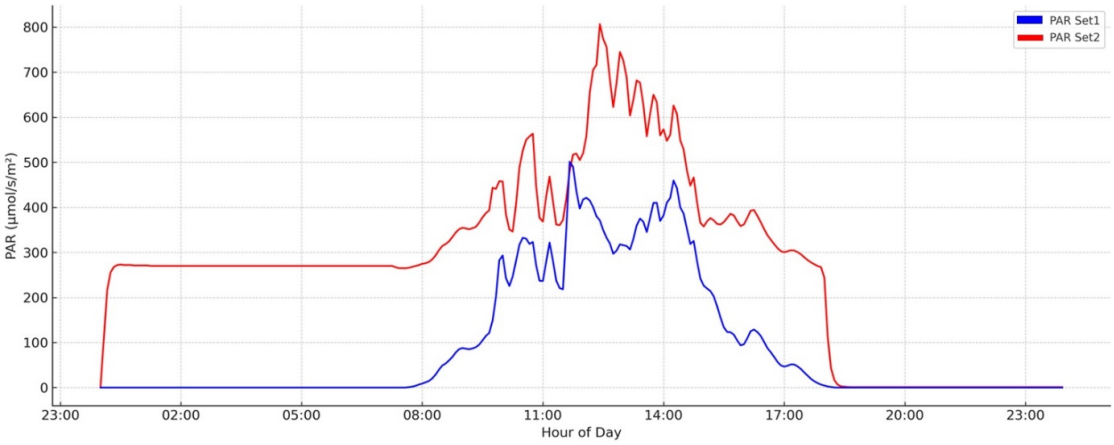

Figure 5.6: Daily PAR exposure comparison between Set1 and Set2.

Figure 5.7 shows the diurnal course of photosynthetically active radiation (PAR) data measured for Set 3 (red curve) and Set 4 (blue curve) from the second

experiment. There is a dramatic increase in PAR intensity, with values reaching nearly four times those recorded in the first experiment. Such a quantitative jump suggests a change in environmental conditions between the two greenhouses. The recorded data reveal that Set 4 experienced markedly higher peak illumination, reaching values above 3000 μmol s^{-1} m^{-2} , whereas Set 3 reached slightly lower maxima of around 2500 μmol s^{-1} m^{-2}. Despite these amplitude differences, the overall temporal profiles remain consistent, indicating that both sets were subjected to the same general light cycle.

These intense PAR values should theoretically greatly enhance the photosynthetic capacity of plants, potentially allowing them to reach photosynthetic saturation and accelerate growth.

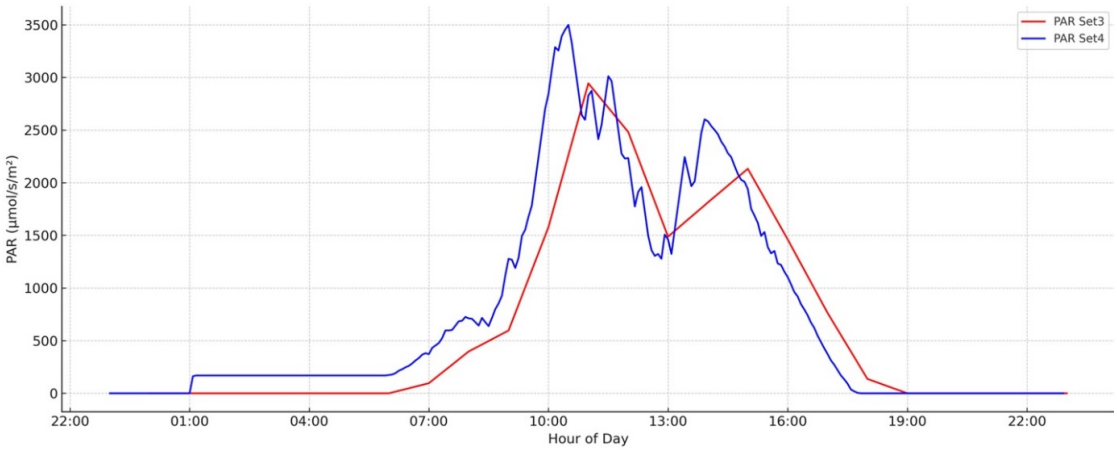

Figure 5.7: Daily PAR exposure comparison between Set3 and Set4, including artificial lighting contribution for Set4.

Indeed, the effect of photosynthetically active radiation (PAR) on plants is fundamentally quantum and not energetic [203]. The process of photosynthesis is initiated by the absorption of photons by leaf pigments. Therefore, the efficiency of light in driving photosynthesis in an "average plant" does not depend on the total incident energy, but on the number of photons in the 400-700 nm band and their suitability for the photosynthetic action spectrum [203]. This photochemical process is not an isolated event; it lies at the heart of a chain of events that directly governs the plants' water consumption where the main link is the stomatal regulation.

Figure 5.8 presents the daily evolution of plant water uptake for Set 3 (red curve) and Set 4 (blue curve) during the second experiment. The values were derived from irrigation and drainage measurements, representing the total amount of water absorbed by the plants each day, expressed in kg.

Both sets exhibit a similar temporal pattern, characterized by an initial increase in water uptake followed by day-to-day fluctuations. The general trend indicates that Set 4 consistently absorbed more water than Set 3, with daily values ranging between approximately 6 kg and 10 kg for Set 4 and 4 kg to 8 kg for Set 3. The results show that Set 4, which received supplemental lighting, exhibited consistently higher daily water uptake, reflecting increased water demand associated with elevated light exposure and potentially enhanced photosynthetic activity.

After March 17, both sets show a stabilization of water uptake with slight oscillations, suggesting that plants had reached a steady physiological state under stable greenhouse conditions. The sharp decreases at the end of the period correspond to the reductions in irrigation.

Overall, these results confirm that light availability strongly influences daily plant water uptake. This relationship supports the use of concurrent PAR and water-uptake monitoring as complementary indicators of plant water status and environmental response.

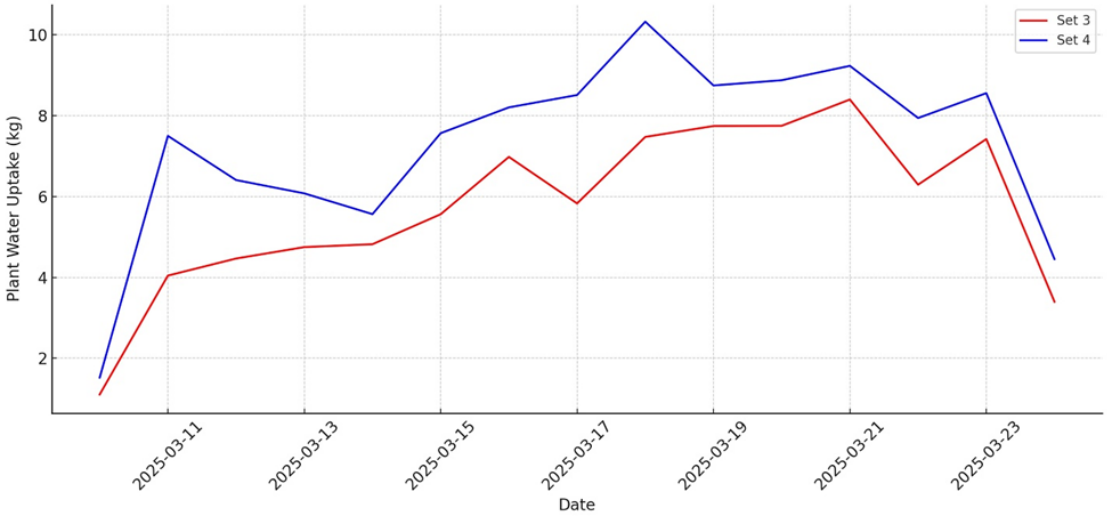

Figure 5.8: Daily plant water uptake comparison between Set3 and Set4.

To analyse the dynamic movements of petioles, it was mandatory to assess the real patterns by carefully preprocessing the IMU data to distinguish true plant responses from simple artifacts such as mechanical disturbances, whether from accidental contact during greenhouse maintenance or even from obstruction by insects. Figure 5.9 shows some examples of the Euler angles before and after signal filtering and corrections of certain sensors.

As shown in Figure 5.9, the plant moves its petiole according to a predictable

daily rhythm. This allows it to adapt to light in advance and better capture the sun's energy for growth.

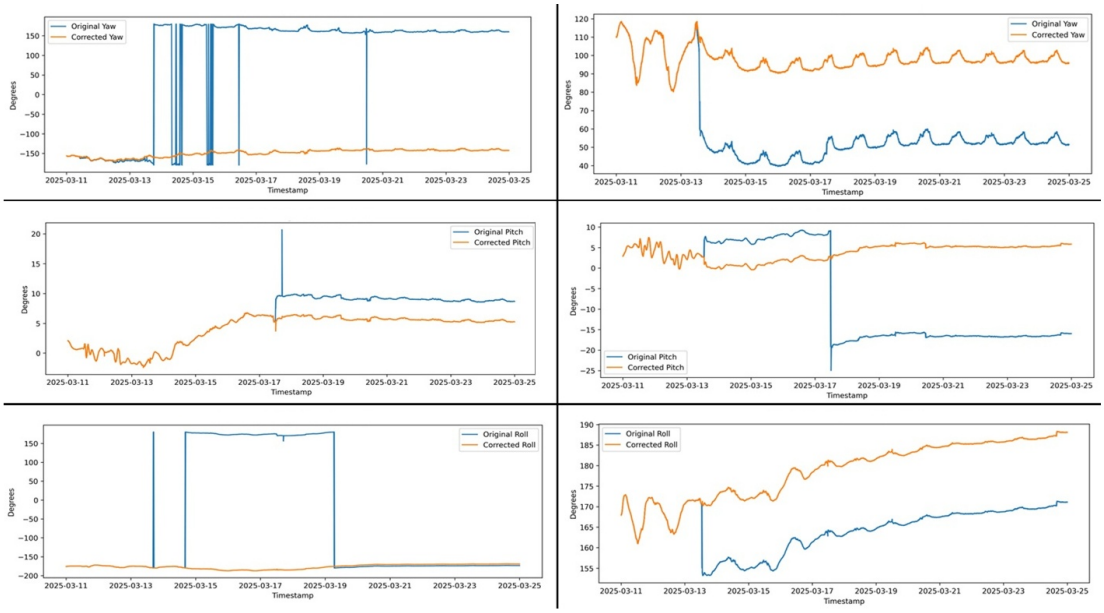

Figure 5.9: Comparison between the original and corrected Euler angle signals (yaw, pitch, and roll) for two representative sensors, S4-04 and S4-10, over the experimental period.

Then, a machine learning analysis was applied to evaluate the predictability of petiole orientation from each set as discussed before in subsection 5.2.2. The best-performing model of each sensor was then selected based on their metrics. The results for the first and second experiments are gathered respectively in Table 5.2 and Table 5.3.

Table 5.2: Best Model Performance for Petiole Movements Prediction – Set 1 (Control) vs Set 2 (Energy-Controlled Lighting = Test).

Sensor	**Target Angle**	**Best Model**	R^2 **Score**	**MAE (°)**	**Treatment**
S1-08	Pitch	XGBoost	0.448	0.072	Set1 – Control
S1-08	Roll	Random Forest	0.631	0.057	Set1 – Control
S1-08	Yaw	Random Forest	0.483	0.578	Set1 – Control
S2-06	Pitch	Random Forest	0.166	2.667	Set2 – Test
S2-06	Roll	Random Forest	0.253	3.263	Set2 – Test
S2-06	Yaw	XGBoost	0.334	2.141	Set2 – Test

Table 5.3: Best Model Performance for Petiole Movements Prediction – Set 3 (Control) vs Set 4 (Energy-Controlled Lighting = Test).

Sensor	**Target Angle**	**Best Model**	R^2 **Score**	**MAE (°)**	**Treatment**
S3-12	Pitch	Random Forest	0.113	0.961	Set3 – Control
S3-10	Roll	SVR	0.021	11.584	Set3 – Control
S3-12	Yaw	Random Forest	0.269	4.314	Set3 – Control
S4-04	Pitch	Random Forest	0.110	3.091	Set4 – Test
S4-05	Roll	Random Forest	0.126	3.067	Set4 – Test
S4-05	Yaw	XGBoost	0.524	2.254	Set4 – Test

To clarify the complexity of the machine learning models reported in Table 5.2 and Table 5.3, all models were trained using a limited and controlled size. In this context, model size refers to the number of trees and their depth for tree-based algorithms. For Random Forest models, a small number of trees was used, with the maximum tree depth restricted to avoid overly complex decision rules. Similarly, XGBoost models were trained with a limited number of boosting iterations and shallow trees. These choices were made intentionally to reduce the risk of overfitting and to keep the models lightweight and interpretable.

The modelling results revealed variable predictive performances depending on growth conditions. The most accurate prediction was obtained for the roll angle of sensor S1-08 in Set 1 (Figure 5.10, left), with the Random Forest model achieving an exceptionally high R^2 score of 0.63 and a very low mean absolute error (MAE) of 0.057°. This performance indicates that the roll movement under natural lighting conditions follows a pattern that is sufficiently stable and reproducible to be reliably captured by the algorithm. Conversely, the models applied to the plants in Set 2, which were subjected to supplemental lighting, and showed consistently lower performance. For example, the yaw prediction for sensor S2-06 using the XGBoost model only achieved an R^2 score of 0.33, with a significantly greater dispersion of errors around the ideal prediction line (Figure 5.10, right). This divergence in results suggests that supplemental lighting, while inducing more intense physiological activity as evidenced by increased water consumption, simultaneously introduced greater variability and complexity in petiole movements.

However, a notable improvement in prediction performance was observed for the yaw angle in plants in the Set 4 group, which were subjected to controlled artificial lighting. Under these conditions, the XGBoost model achieved an R^2 score of 0.52 for sensor S4-05, a significant increase compared to the performance obtained in Set 3 ($R^2 = 0.27$ for sensor S3-12). This improvement was accom-

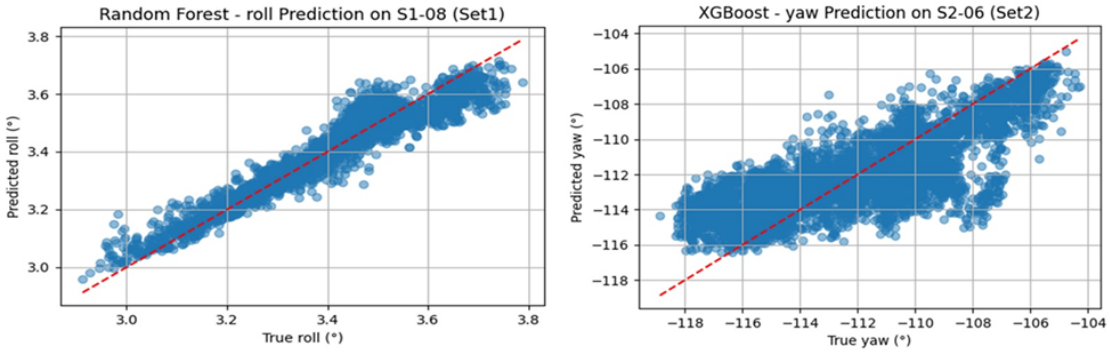

Figure 5.10: Best model predictions for Set1 and Set2.

panied by a significant reduction in the mean absolute error (MAE), indicating greater predictive accuracy. Figure 5.11 confirmed this trend by showing a tighter gathering of points around the ideal prediction line for Set 4, in contrast to the greater dispersion observed for Set 3. These results suggest that the extensive light exposure of Set 4 induced more stereotypical and regular yaw movements, probably related to an optimization of leaf orientation to capture additional light energy. Conversely, the greater variability of movements under just natural light of Set 3 possibly reflects a more dynamic and complex adaptation to natural fluctuations in light intensity and direction, making these patterns less predictable by the model.

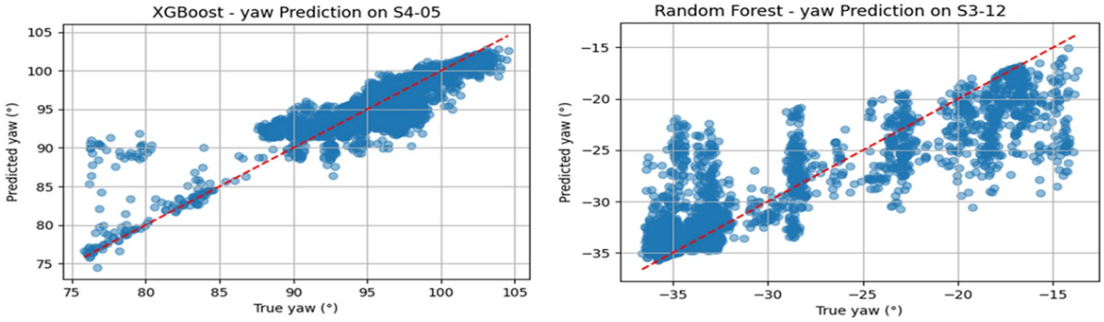

Figure 5.11: Best model predictions for Set3 and Set4.

However, these results suggest that the observed petiole movements are part of a strategy to optimize the plant's capture and use of light energy. Several factors confirm this interpretation. First, the circadian nature of the movement signals, preserved after correction, indicates rhythmic and potentially anticipatory behavior in response to light cycles, rather than a simple passive reaction. This is consistent with an evolutionary adaptation mechanism to maximize pho-

tosynthesis during the day. Second, the greater predictability of yaw movement under supplemental lighting of Set4 indicates that the plant adjusts its posture in a more stereotypical and probably more efficient manner when light resources are abundant but must be managed. At the same time, the significant increase in water consumption in the same set forms a logical causal chain: increased lighting stimulates potential photosynthesis, leading to increased transpiration and therefore a greater requirement of water. The movements of the petioles could thus be adjusted accordingly to support and regulate this amplified physiological activity. Finally, the sensitivity of the roll angle, often associated with parheliotropism (protective movement against excess light), emphasizes that the objective is optimization rather than maximization of exposure. The plant actively modulates the orientation of its leaves to find a compromise between capturing light energy and avoiding photooxidative damage.

5.4 Conclusion

This work successfully demonstrated the development, validation, and optimization of an innovative wireless sensor system for real-time monitoring of tomato petiole movements. The results confirm the technical feasibility of accurate, non-invasive tracking of plant physiological responses to environmental conditions, particularly under varying light regimes. From an analytical perspective, the application of machine learning models revealed that petiole movement patterns, especially yaw, are strongly correlated with light exposure (PAR) and circadian rhythm, although their predictability varies with growth conditions. Plants grown under supplemental artificial lighting exhibited more stereotyped and predictable movement patterns, in contrast to those exposed exclusively to natural light, where greater variability reflected a dynamic adaptation to natural fluctuations. From a technical standpoint, reducing the IMU samples from 120 to 80 was decisive. It maintained acceptable metrological accuracy, especially for pitch and yaw, reduced energy consumption by 4.3%, and extended sensor autonomy by 24 days. This improvement supports long-term deployments with minimal maintenance.

Taken together, these findings highlight the potential of plant-based sensors for resilient precision agriculture. The ability to detect early signs of abiotic stress through plant movements paves the way for proactive crop management, optimizing resource use while enhancing the sustainability of greenhouse production systems.

6

IoT-Based Irrigation Management Platform (Spritz Project)

6.1 Introduction

Water scarcity is regarded as one of the most pressing challenges confronting the planet, particularly within the agricultural sector, which accounts for the largest share of global freshwater consumption. Conventional irrigation techniques frequently result in considerable wastage of this valuable resource, thereby exacerbating pressure on limited reserves and adversely affecting crop health and productivity. Research has demonstrated that over-irrigation can be as detrimental as under-irrigation, resulting in root diseases, nutrient leaching, and diminished plant resilience. In response to the challenges identified, Agriculture 4.0 has been proposed as a transformative solution. This initiative utilizes cutting-edge technologies with the aim of modernizing conventional agricultural practices. As emphasized by Choudhary [156], the Internet of Things (IoT) facilitates real-time crop monitoring and control through wireless sensor networks, connected devices, and web services, thereby engendering more efficient, sustainable, and resilient agricultural systems.

The SPRITZ project is positioned precisely within this perspective. This multidisciplinary research and development initiative addresses the critical challenge

of modern agriculture by improving productivity and sustainability of farming systems through data-driven resource management. Specifically, SPRITZ aims to design an intelligent, modular irrigation platform tailored to the needs of small and medium-sized farms, an audience that is often overlooked by standardized industrial solutions.

This chapter presents the work conducted during my PhD in collaboration with Abinsula, co-funder of my scholarship under Italy's National Recovery and Resilience Plan (PNRR). The project focuses on the development of a sensing and control system for automated, adaptive irrigation. The chapter outlines the system's objectives, architecture, and experimental outcomes.

6.2 Context of the Project

SPRITZ project (**S**ensorized **P**latform for the **R**econfiguration of **I**rriga**T**ion based on **Z**one Measurements) is a regional research and development initiative that seeks to improve irrigation efficiency in small and medium-sized farms using smart, connected technologies. The project was conceived to address the specific needs of Sardinian agricultural enterprises, especially agritourism and organic farms, which typically operate with limited resources but require reliable and adaptive irrigation strategies to sustain high-quality production.
The project is composed of three key partners, each contributing distinct expertise and responsibilities:

- **Lifely (R&D division of Abinsula)** coordinates the project and leads the design of the SPRITZ platform, including the implementation of field sensors, network connectivity, and cloud computing [204, 205].
- **CNR-IBE** (Institute for BioEconomy, National Research Council of Italy) is a research institute that contributes scientific expertise in Life Cycle Assessment (LCA) to evaluate the system's impact in terms of water footprint, energy use, and carbon emissions [206].
- **Agriturismo Agave** is a certified organic farm and agritourism in Alghero (north-west Sardinia). The farm grows vegetables, olives, almonds, and grapes, and regularly hosts visitors for educational activities. As a project partner, it served as the pilot deployment site for the SPRITZ system, where it was carried out the implementation of the platform under real operating conditions [207].

6.3 System Architecture and Implementation

This section details the end-to-end implementation of the irrigation system architecture, building on the elements introduced in subsection 3.4.2.

An overview of the smart irrigation system

In the SPRITZ setup, battery-powered field sensors send measurements over LoRaWAN to a nearby gateway. The gateway forwards these data to AWS IoT Core for LoRaWAN, where an IoT Rule invokes a Lambda function that decodes the payloads, adds timestamps and zone IDs, and stores the clean records in Amazon DynamoDB. The same function shares the decoded JSON to Akenza via a secure HTTPS endpoint, so the updates appear on website dashboards in real time.

For irrigation control, the cloud sends the latest soil moisture readings via MQTT to the SPRITZ irrigation controller, a Wi-Fi device based on the ESP32-S3. The controller compares each reading with the predefined threshold for its zone. If the value is below the threshold, it activates the corresponding solenoid valve for a set duration and reports the valve status back to AWS. A LoRaWAN water meter measures the actual water flow and total volume, sending this data to AWS. This completes the loop of sensing, decision-making, actuation, and verification. An overview of the smart irrigation system implementation is shown in Figure 6.1.

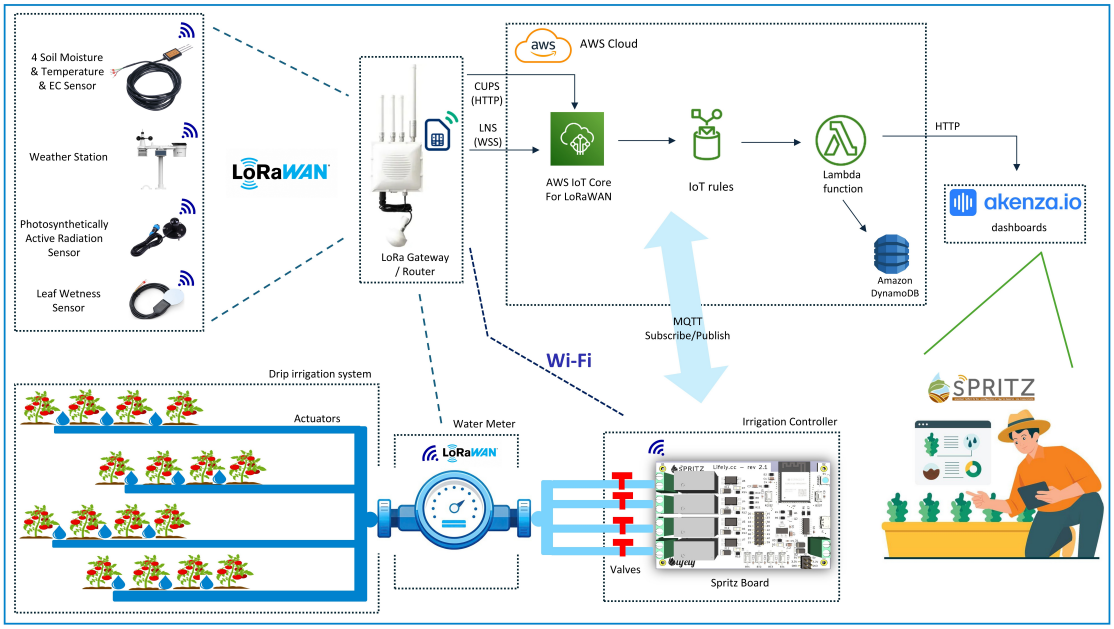

Figure 6.1: Overview of the smart irrigation system.

Field Sensor Layer: LoRaWAN Nodes and Gateway

The system employs a variety of field sensors to capture key agricultural parameters, such as soil moisture probes to gauge water content in soil, ambient temperature and humidity sensors, a weather station to monitor the environment's parameters, a leaf wetness sensor to detect moisture on crop canopies, and a solar radiation sensor to measure sunlight intensity. Each sensing node is built around a LoRaWAN Data Logger, which is an industrial-grade module that can connect to multiple sensor types and encapsulate their readings into LoRaWAN uplink packets [208], transmitting them over the ISM sub-GHz band (EU868) via LoRa radio to the nearest gateway. This approach allows long-range wireless data transmission over several kilometers and long-life operation for years, which makes it ideal for agricultural deployment.

In this system, all sensor nodes communicate in a star-of-stars LoRaWAN topology. They send their uplinks to a central LoRaWAN gateway (the RAK7249 WisGate, Figure 3.18) installed on-site on a pole for maximum coverage range, which serves as the collector for all sensor data. It contains a multi-channel LoRa concentrator (Semtech SX130x) capable of receiving multiple LoRa signals from different sensor nodes in parallel, ensuring reliable coverage of the entire field, and forwarding them to a LoRaWAN network server over the internet. The gateway has an integrated cellular backhaul and uses a 4G IoT SIM to forward data to the internet, with Ethernet/Wi-Fi as failover options for connectivity.

LoRaWAN Gateway and Connectivity to AWS

The gateway serves as a bridge between the field sensors and the cloud through AWS IoT Core for LoRaWAN. It runs standard software that maintains a secure, encrypted connection to the AWS platform. This connection performs two main functions: it links to the *LoRaWAN Network Server* (LNS), which authenticates devices, manages data flow, and routes messages correctly; and it connects to a *Configuration and Update Server*, enabling remote software and settings updates essential for system maintenance.

Once the gateway's EUI (Extended Unique Identifier) and AWS credentials are registered, it automatically forwards sensor data to the cloud in near real time, without requiring a local network server.

AWS-Based Network and Cloud Communication

On the cloud side, AWS IoT Core for LoRaWAN performs two key functions: it manages the wireless network connections and routes incoming data using both

the LoRaWAN Network Server (LNS) and the IoT message broker. When the RAK7249 gateway sends a packet, AWS first verifies the device identity using the `DevEUI` and session keys. Then, it checks the message integrity by validating the LoRaWAN Message Integrity Code (MIC) to ensure the packet has not been altered during transmission. Finally, it decrypts the payload.

Once validated, the data is published as a standard IoT message on a device-specific MQTT topic. This topic is a unique channel named using the device's ID or path, ensuring that only authorized subscribers can access messages from that device.

Furthermore, an AWS IoT Rule (called a "Destination" in IoT Wireless) is attached to each incoming message and triggers an AWS Lambda function. Lambda is a serverless compute service that automatically runs code in response to events, scaling as needed without the need to manage servers.

In this project, the Lambda function decodes the sensor payload, which is encoded in Base64 format as a binary string received from the LoRaWAN message. For example, a soil moisture sensor may send a two-byte value. The Lambda function applies the appropriate scaling and calibration to convert this into a readable measurement, such as 27.4 VWC. The decoded data is then enriched with metadata (device ID, sensor type, timestamp, and zone) and formatted as a structured JSON object for downstream use as follows:

```
{
  "device": "Zone1_sensor",
  "soil_moisture": 27.4,
  "unit": "%",
  "timestamp": "2025-09-20T10:15:00Z"
}
```

Once the data is processed, the Lambda function saves it to a cloud database. In this system, Amazon DynamoDB is used. It is a NoSQL database optimized for handling IoT data streams. Each record is indexed by device ID and timestamp (e.g., *partition key* = sensor node ID, *sort key* = timestamp), with additional indexes to query data by zone or sensor type. This structure supports continuous data streams with high throughput and enables fast read access (on the order of milliseconds), making it well-suited for real-time dashboard visualization.

Firmware Implementation of the Irrigation Controller (Wi-Fi Connectivity)

The ESP32-S3 microcontroller begins by connecting to the Wi-Fi network using stored credentials. Once connected, it establishes a secure MQTT connection to

Amazon AWS IoT using a digital certificate and private key stored on the device. The controller then subscribes to MQTT topics associated with soil moisture readings for each monitored zone and receives real-time sensor data.

The firmware implements threshold-based automation. For every soil moisture value received, the controller compares it to the predefined threshold for that zone. If the value is below the threshold (indicating dry soil), the ESP32-S3 activates the corresponding relay to open the solenoid valve for that zone and start irrigation. When the `startValve(index)` function is called, the relay GPIO is set high to open the valve, and a timer starts using the Arduino `Ticker` library. Each zone has a preconfigured irrigation time based on agronomic parameters such as soil type and crop needs (e.g., Zone 1 = 15 min, Zone 2 = 20 min, Zone 3 = 45 min, Zone 4 = 30 min). Once the set time elapses, the ticker automatically calls the `stopValve` routine to deactivate the relay and close the valve. This ensures that irrigation runs for the intended duration, even if new sensor data is delayed, preventing over-watering.

Figure 6.2 illustrates the logic flows implemented in the SPRITZ firmware, where Figure 6.2a shows the startup sequence executed on device boot, and Figure 6.2b represents the threshold-based decision logic applied when new soil-moisture data is received.

When the controller starts or stops a valve, it also publishes the valve status to AWS IoT. Each relay or valve has its own MQTT topic (e.g., `"Relay1"` for Zone 1). The controller sends `"1"` when a valve opens and `"0"` when it closes, allowing the cloud platform to track valve states in real time.

The controller includes a **Maintenance Mode**, a safety feature that temporarily disables automation to prevent unintended watering during servicing. When a JSON message with `"maintenance mode: true"` is received on the topic `"Spritz/maintenance/Start"`, the controller immediately enters maintenance mode. In this state, all active valves are stopped, and new commands are ignored. The controller also disconnects from Wi-Fi and AWS IoT for the duration of the maintenance period, ensuring no automatic actions occur while technicians are working. By default, maintenance mode lasts 30 minutes, monitored by an internal timer. When the timer expires, the controller automatically reconnects to Wi-Fi and AWS and publishes a `"maintenance-complete"` message on the `"Spritz/maintenance/End"` topic, indicating that normal operation has resumed.

For convenience, the SPRITZ controller provides local manual controls. Pressing a button toggles the corresponding valve, bypassing the automation logic. This feature is especially useful during installation or troubleshooting, allowing direct control of the valves without using the cloud interface.

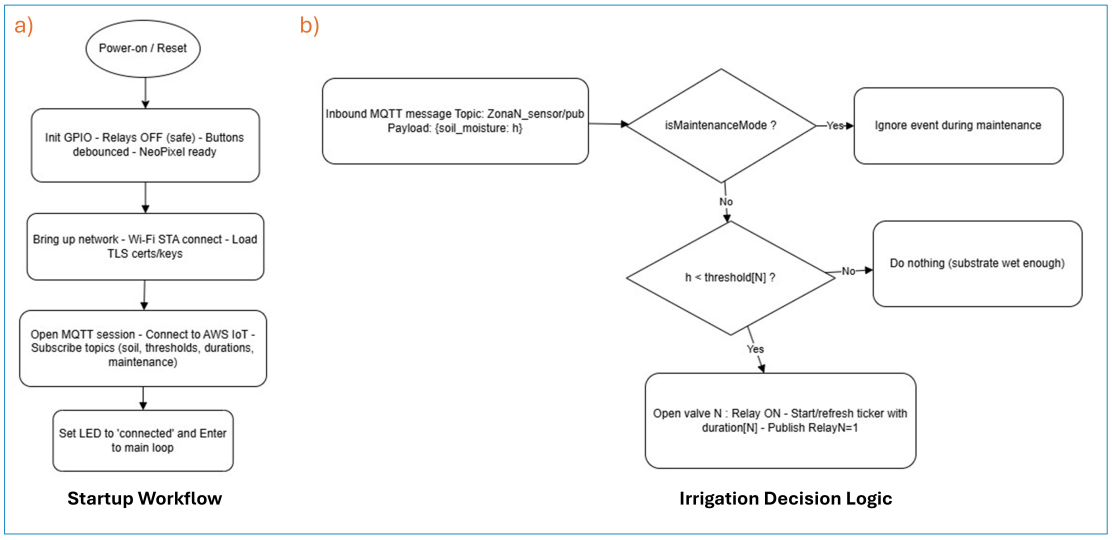

Figure 6.2: System logic flows: (a) startup sequence of the SPRITZ controller; (b) decision-making process for soil-moisture-based irrigation.

The controller also supports **dynamic configuration updates** via MQTT. It subscribes to parameter-specific topics (one per zone) that allow remote updates to irrigation settings. These include changes to valve duration, maintenance time, or soil moisture thresholds. When a new message arrives, the ESP32-S3 validates the input and updates the configuration, enabling flexible, remote adjustments without firmware modification.

The complete control logic, including communication checks, valve timing, and maintenance handling, is executed continuously in the controller's main loop, as shown in Figure 6.3.

Water Usage Monitoring: LoRaWAN Water Meter

To track exactly how much water is used for irrigation, the system integrates a LoRaWAN-enabled water meter on the main irrigation line. This setup consists of an ultrasonic flow meter integrated with a LoRaWAN pulse counter transmitter.

The meter is installed upstream of the valve manifold, which measures the total water used across all four zones and reports the cumulative volume in cubic meters (m^3). Using the transit-time ultrasonic principle, it accurately measures the flow by timing ultrasonic pulses sent through the water. Each time a specific volume of water passes through, the meter generates a pulse and increments an internal counter.

The transmitter periodically sends the total pulse count via a RAK7249 gate-

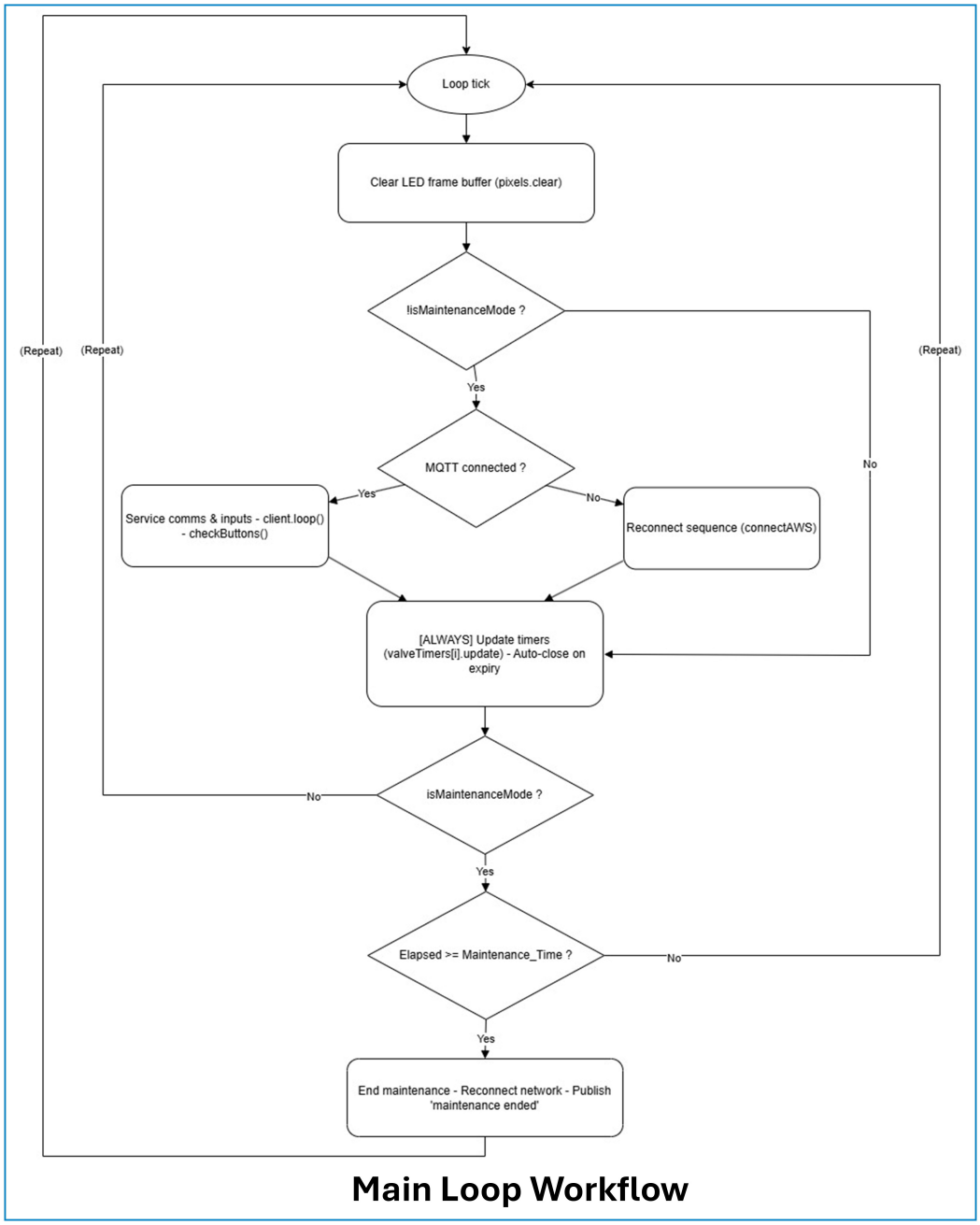

Figure 6.3: Workflow diagram of the main operational loop implemented in the SPRITZ irrigation controller, handling MQTT communication, valve timing updates, and maintenance mode management.

way to AWS IoT Core. There, a Lambda function decodes the payload and converts the pulse count into a meaningful volume reading using the meter's calibration factor. The data is then stored in a DynamoDB table alongside the other sensor data.

This process provides a time-stamped log of all irrigation water consumption, enabling the system to generate reports on the water used per irrigation cycle and verify whether the automated system is indeed achieving water savings.

User-Friendly Visualization with Akenza.io Dashboard

To provide operators and stakeholders an intuitive way to manage the system, all data is visualized on a web dashboard powered by *Akenza.io*. This IoT platform allows building dashboards without developing a custom frontend from the beginning.

As previously outlined, the data flow begins when a sensor reading reaches AWS IoT Core. An AWS IoT Rule then triggers a Lambda function, which decodes the raw payload into readable measurements, validates the data, and formats it into a structured JSON document.

Next, the Lambda function securely transmits the JSON document to *Akenza.io* using a TLS-encrypted HTTPS `POST` request to Akenza's HTTP ingest endpoint. Authentication is handled via an API token stored in AWS Secrets Manager. Once received, Akenza directly stores the message and updates the associated dashboard widgets in near real-time, without requiring additional parsing. If the `POST` request fails, the Lambda function automatically retries and, if necessary, places the record in a dead-letter queue for future re-submission.

The dashboard is accessible at `https://spritzpro.com/dashboard/` [209], where users can view real-time updates from the field. Key features of the dashboard, as shown in Figure 6.4, include:

(1) Site context (map and device selector): A map view and device selector at the top allow users to choose the farm or field of interest. The dashboard shows the last contact time and provides quick access to different device groups.

(2) Weather station panel (environmental context): Live and historical environmental data are presented in separate cards for each parameter, including air humidity, temperature, wind speed/direction, UV index, ambient light (lux), rainfall, and barometric pressure. Each card displays the current value, a color-coded qualitative range, and a mini time-series graph for visual trend analysis over the past hour, day, or month.

(3) Soil panel (per field zone): Displays the crop type, soil moisture (VWC, %), temperature (°C), and electrical conductivity (mS/cm) for each monitored zone. Each card uses a color-coded scale to indicate status (normal or critical) and includes a sparkline to show recent trends. These readings are used by the controller for automated irrigation decisions.

(4) Canopy wetness and solar radiation: Cards show leaf wetness status/temperature and solar irradiance (W/m^2) from the PAR sensor. These help distinguish between dew and rainfall, detect fungal risk, and estimate plant water demand.

(5) Water meter and device health: Summarizes water usage (m^3), flow activity, and meter diagnostics such as battery status and temperature. It links irrigation activity to actual water consumption and verifies system performance.

Additionally, the Akenza dashboard includes interactive time-series charts for historical data analysis. Users can select any sensor or zone to visualize trends such as soil moisture variation over the past month or daily water usage. The platform also supports configurable alerts: for example, if soil moisture in a zone remains below a critical threshold for too long, or if unusually high flow rates suggest a leak, the system notifies users via on-screen alerts.

The dashboard represents the final stage of the system's end-to-end integration. From sensing and cloud-based processing to field actuation and visualization, all components work together seamlessly, providing clear insight and precise control for efficient irrigation management.

6.4 Discussions

The SPRITZ smart irrigation platform demonstrates several key strengths arising from its modern IoT architecture. Firstly, its LoRaWAN-based wireless sensors provide reliable, long-range coverage across the farm, operating over distances of several kilometers with very low power consumption. Secondly, the cloud-native backend, built on AWS IoT Core, Lambda functions, and DynamoDB, handles processing and data storage in the cloud, ensuring high scalability and reliability. Third, the choice of a Wi-Fi-based ESP32-S3 microcontroller for the irrigation controller, instead of a LoRaWAN node, improves responsiveness by enabling low-latency command execution. Finally, the platform includes a real-time dashboard

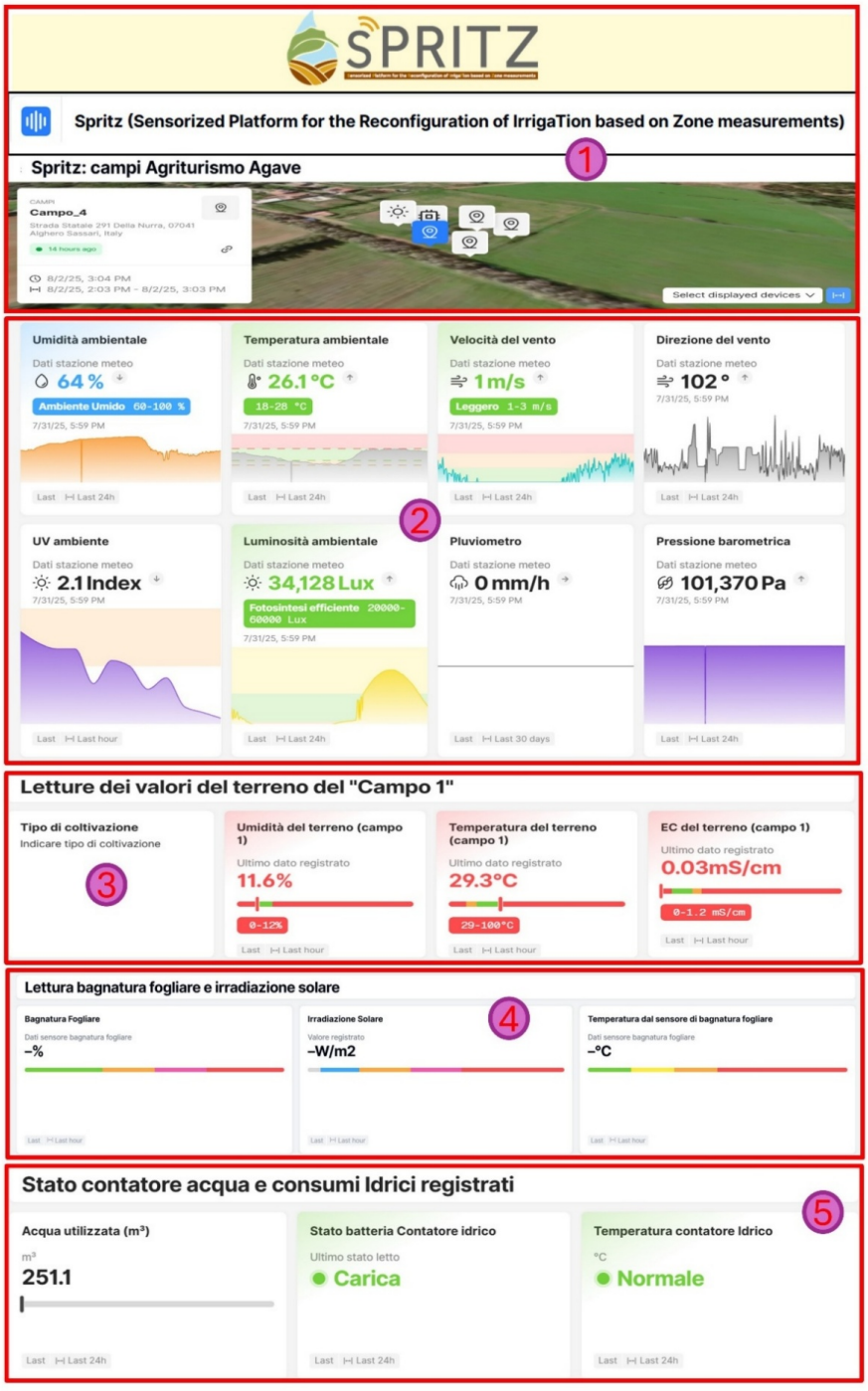

Figure 6.4: Interactive dashboard of the SPRITZ system, developed on the Akenza platform, showing the main sections for monitoring and control.

on Akenza.io, integrated into the SPRITZ web portal, where users can visualize live sensor readings, historical trends, and system status. This architecture enables precise, demand-driven irrigation based on crop needs, improving water-use efficiency on the Sardinian tomato farms. Overall, this architecture enables demand-driven irrigation based on field conditions, aiming to improve water-use efficiency in contexts where water is a scarce resource. Similar IoT-based irrigation systems reported in the literature have shown meaningful reductions in water consumption compared to traditional scheduling approaches [210]. By watering only when and where needed, the system reduces waste and supports more efficient irrigation management.

Deployment status and practical evaluation

To evaluate practical applicability, the SPRITZ platform was fully deployed in a real agricultural setting and operated continuously for at least 40 days. The deployment included field sensors communicating via LoRaWAN to a gateway, cloud-based data ingestion and storage, a web dashboard for monitoring, and an irrigation controller capable of executing valve commands. This operational period allowed an initial assessment of the end-to-end workflow (sensor → network → cloud → dashboard/controller) under real outdoor conditions and day-to-day farm constraints.

During the deployment, the LoRaWAN communication link provided robust long-range coverage for distributed sensing, while the cloud infrastructure enabled remote access to live measurements and historical trends. From a user perspective, the dashboard facilitated quick inspection of system status and sensor readings without requiring manual measurements in the field. At the same time, routine maintenance remained necessary in practice, for instance related to sensor power management and occasional gateway or network-related interventions.

After the end of this deployment period, the longer-term operational status of the system could not be verified within the scope of this thesis, as the author was no longer directly involved in the project activities. Nevertheless, the field operation achieved in this work demonstrates the feasibility of the proposed architecture and highlights practical aspects that are critical for long-term deployments.

Earlier IoT irrigation systems commonly relied on Zigbee, Wi-Fi, or GSM/GPRS communication technologies. While these were effective for small-scale or greenhouse environments, they showed limitations in large open fields due to reduced network capacity, higher power consumption, and recurring operational costs [211].

In the SPRITZ system, adopting LoRaWAN connectivity addresses these chal-

lenges by providing long-range, low-power communication suitable for distributed field sensors, using license-free ISM bands available in different regions of the world. Similarly, Enock et al. (2025) [159] proposed a LoRa-based irrigation system that transmitted sensor data to the cloud using a combination of Blynk and ThingSpeak platforms for visualization and storage. Actuator nodes received cloud-based commands to control pumps and valves.

Their solution follows a similar LoRa-to-cloud approach but depends on open-source services, which may increase system complexity, time-to-market, and maintenance overhead. In contrast, the SPRITZ platform leverages AWS-managed infrastructure in combination with Akenza.io, offering better scalability and reliability, although with higher implementation costs and stronger reliance on stable internet connectivity.

Another comparable project by Artetxe et al. (2024) [212] combined LoRa communication with a cloud-based fuzzy logic controller that integrates weather forecast data from online services to optimize irrigation decisions. The system anticipates rainfall and adjusts irrigation schedules accordingly, achieving a 23% reduction in water usage compared to conventional methods [212]. This highlights the advantage of combining real-time sensor feedback with external data sources such as weather forecasts.

Although the current SPRITZ system does not yet implement predictive or weather-aware control, it shares the same LoRa-to-cloud architecture and relies on soil-moisture thresholds to trigger irrigation events. The field deployment performed in this work therefore provides a robust basis for future integration of forecast-based optimization.

Despite its advantages, the system also presents certain limitations. It relies on cloud connectivity, making it vulnerable to internet outages or service downtime. If the internet or cloud service becomes unavailable, automated decisions and remote monitoring are interrupted, which can reduce reliability during backhaul disruptions. In this case, the controller includes manual override buttons for each valve as a safety fallback. However, it lacks an autonomous offline mode, which means that on-site intervention is required until connectivity is restored. This was identified as a key requirement to improve robustness in future deployments.

Furthermore, the current system architecture is relatively complex. It integrates multiple components, including field hardware, a LoRaWAN gateway, and several cloud services such as AWS IoT Core, Lambda, DynamoDB, and the Akenza dashboard. Each layer requires configuration, monitoring, and periodic updates. When issues arise, they may originate from different points in the chain, including the sensor hardware, the gateway, the network connection, the cloud logic, or the user dashboard. This complexity is a common drawback of IoT-based

irrigation systems and highlights the importance of having local personnel trained to perform basic maintenance tasks, such as resetting devices or gateways and replacing sensor batteries, or alternatively, having a support agreement with the system developers.

There are several potential improvements to enhance the SPRITZ system. First, a prediction layer based on machine learning could be added to estimate crop water requirements and optimize irrigation timing by learning from historical soil sensor data and other monitoring inputs. This would enable the system to act proactively, rather than responding solely to real-time sensor feedback.

Second, scheduling could be made weather-aware by integrating a weather forecast API into the AWS Lambda decision workflow, allowing the controller to adapt automatically. For instance, if rainfall is predicted within the next 24 hours, irrigation could be skipped or reduced. Conversely, if high temperatures are predicted for some days, the watering duration could be increased slightly.

These behaviors could be implemented as explicit rules in the SPRITZ controller firmware, combined with the machine learning layer for more refined control. This approach would make the system more context-aware and better aligned with precision agriculture practices.

6.5 Conclusion

This chapter has presented the design and implementation of the SPRITZ smart irrigation platform, a result of collaboration between industry and academia. The project demonstrates a fully integrated IoT-based solution for precision agriculture, combining LoRaWAN field sensors, a cloud-native data pipeline, and an intuitive user dashboard. The system's main achievement lies in establishing a closed-loop, data-driven irrigation process: soil moisture is measured, analyzed in the cloud, and used to trigger precise watering through the ESP32-S3 controller, with water usage independently verified by a LoRaWAN flow meter.

The platform was fully deployed in a real agricultural setting and operated continuously for at least 40 days, demonstrating the feasibility of the proposed architecture under outdoor conditions.

This end-to-end architecture addresses the challenge of water scarcity by enabling irrigation based on the principle of "only what is needed, when it is needed." It also provides a scalable and reliable framework suitable for small to medium-sized farms. Although the cloud-centric design introduces challenges related to system complexity and network dependence, the foundation built by the SPRITZ

project is solid. It offers a strong basis for future developments, such as integrating machine learning and weather-aware forecasting, to further enhance sustainability and precision in agricultural water management.

7 General Conclusion

This thesis presents a comprehensive approach that spans from the fundamental principles governing the relationship between plants and water to the development of advanced technological solutions for sustainable water management in agriculture. The growing challenges of water scarcity and climate change underline the urgent need for intelligent irrigation systems. These challenges also reveal significant gaps, including the limited availability of accurate, real-time physiological monitoring and the lack of integrated ecological data frameworks.

The experimental chapters that follow aim to address these gaps through the design, validation, and systematic deployment of a new generation of sensor technologies.

chapter 3 outlined the experimental methods, tools, and materials that supported the entire research activity. This chapter provided the methodological foundation for the subsequent experimental studies and enabled the development and validation of the sensing systems presented in the following chapters.

chapter 4 demonstrated the effectiveness of infrared and electrical impedance spectroscopy when applied at the leaf level for assessing plant water status, with validation against the relative water content standard. Despite challenges related to sunlight interference and electrode design, the study confirmed that indirect and non-invasive assessmet of plant hydration is feasible.

Building on these results, **chapter 5** extended the focus from static hydration

assessment to dynamic physiological monitoring. An IoT-based sensor system was used to track petiole movements, which were correlated with environmental factors. The successful optimization of energy consumption and reliable long-term operation highlighted the potential of the Internet of Things (IoT) for continuous and non-destructive plant monitoring.

Finally, **chapter 6** integrated the developed technologies into a unified and practical framework. The design and implementation of the SPRITZ smart irrigation system represented the culmination of this research. The system combines soil moisture sensing, cloud-based data processing, and automated irrigation control within a closed-loop architecture. The transition from laboratory validation to field deployment demonstrated the feasibility of a scalable and data-driven approach to efficient water management in small and medium-sized farms.

In summary, this thesis supports the vision that the future of sustainable agriculture depends on multi-sensor and data-centric strategies. It shows that irrigation management can move beyond soil-based measurements and subjective assessments toward approaches that rely directly on plant physiological signals, including hydration level and dynamic movement responses.

Looking ahead, future research should focus on the fusion of multiple sensor data streams that integrate direct plant water status, continuous movement monitoring, and contextual environmental information. The goal is to develop a robust and multi-layered decision-support system for predictive agriculture, capable of anticipating stress conditions before they become critical. Parallel efforts should aim at improving hardware robustness and adaptability, enabling the next generation of sensors to operate effectively across different plant structures and environmental conditions.

Bibliography

[1] D. Or, M. Tuller, and J. M. Wraith, "Soil water potential," in *Encyclopedia of Soils in the Environment*, D. Hillel, Ed. Oxford: Elsevier Academic Press, 2005, vol. 3, pp. 270–277. [Online]. Available: https://www.sciencedirect.com/referencework/9780123485304/encyclopedia-of-soils-in-the-environment (Cited on pages viii, 11, and 12)

[2] A. N. Lakso, M. Santiago, and A. D. Stroock, "Monitoring stem water potential with an embedded microtensiometer to inform irrigation scheduling in fruit crops," *Horticulturae*, vol. 8, no. 12, p. 1207, Dec. 2022. [Online]. Available: http://dx.doi.org/10.3390/horticulturae8121207 (Cited on pages viii, 11, 13, and 14)

[3] J. E. Fernández Luque, C. M. Rodríguez-Domínguez, J. M. Torres Ruiz, A. Pérez Martín, M. V. Cuevas Sánchez, and A. Díaz-Espejo, "Use of the zim probe to schedule irrigation in a high-density olive orchard," in *Proceedings of the 4th International Conference "Olive growing and Biotechnology of olive products" (OLIVEBIOTEQ 2011)*. Chania, Crete, Greece: Institut de recherche pour le développement (IRD), France, oct 2011, conference dates: 31 Oct–4 Nov 2011. [Online]. Available: https://digital.csic.es/handle/10261/121653 (Cited on pages viii and 15)

[4] J. Pietragalla and A. J. D. Pask, "Stomatal conductance," in *Physiological Breeding II: A Field Guide to Wheat Phenotyping*, A. J. D. Pask, J. Pietragalla, D. M. Mullan, and M. P. Reynolds, Eds. Mexico, D.F.: CIMMYT (International Maize and Wheat Improvement Center), 2012, pp. 15–17. [Online]. Available: https://www.generationcp.org/communications/research-publications/books/doc_details/474-physiological-breeding-ii-a-field-guide-to-wheat-phenotypingbd57.html (Cited on pages viii, 11, 16, and 17)

[5] V. B. Koman, T. T. S. Lew, M. H. Wong, S.-Y. Kwak, J. P. Giraldo, and M. S. Strano, "Persistent drought monitoring using a

microfluidic-printed electro-mechanical sensor of stomata in planta," *Lab on a Chip*, vol. 17, no. 23, p. 4015–4024, 2017. [Online]. Available: http://dx.doi.org/10.1039/C7LC00930E (Cited on pages viii, 17, and 18)

[6] H. Hackl, J. P. Baresel, B. Mistele, Y. Hu, and U. Schmidhalter, "A comparison of plant temperatures as measured by thermal imaging and infrared thermometry," *Journal of Agronomy and Crop Science*, vol. 198, no. 6, p. 415–429, Apr. 2012. [Online]. Available: http://dx.doi.org/10.1111/j.1439-037X.2012.00512.x (Cited on pages viii and 19)

[7] A. Afzal, S. W. Duiker, and J. E. Watson, "Leaf thickness to predict plant water status," *Biosystems Engineering*, vol. 156, p. 148–156, Apr. 2017. [Online]. Available: http://dx.doi.org/10.1016/j.biosystemseng.2017.01.011 (Cited on pages viii, 20, and 21)

[8] T. Repo, "Seasonal changes of frost hardiness in piceaabies and pinussylvestris in finland," *Canadian Journal of Forest Research*, vol. 22, no. 12, p. 1949–1957, Dec. 1992. [Online]. Available: http://dx.doi.org/10.1139/x92-254 (Cited on pages viii, 23, 24, and 25)

[9] E. Azzarello, S. Mugnai, C. Pandolfi, E. Masi, and S. Mancuso, "Stress assessment in plants by impedance spectroscopy," in *Floriculture, Ornamental and Plant Biotechnology: Advances and Topical Issues, Volume III*, J. A. Teixeira da Silva, Ed. Isleworth, UK: Global Science Books, 2006, pp. 140–148. (Cited on pages viii, 26, and 27)

[10] E. C. Weldemariam, "Modeling leaf chlorophyll content in heterogeneous forest using high-resolution multispectral image: A case study of bavaria forest national park," Master's thesis, Faculty of Geo-Information Science and Earth Observation (ITC), University of Twente, Enschede, The Netherlands, Feb. 2016, mSc thesis. [Online]. Available: https://essay.utwente.nl/fileshare/file/83823/83823_weldemariam.pdf (Cited on pages ix and 30)

[11] S. Jacquemoud, "Comparison of four radiative transfer models to simulate plant canopies reflectance direct and inverse mode," *Remote Sensing of Environment*, vol. 74, no. 3, p. 471–481, Dec. 2000. [Online]. Available: http://dx.doi.org/10.1016/S0034-4257(00)00139-5 (Cited on pages ix, 30, and 78)

[12] D. SUHANDY, N. KHURIYATI, and T. MATSUOKA, "Determination of leaf water potential in tomato plants using nir spectroscopy for water stress management," *Environment Control in Biology*, vol. 44, no. 4, p. 279–284, 2006. [Online]. Available: http://dx.doi.org/10.2525/ecb.44.279 (Cited on pages ix, 31, and 32)

[13] T. D. Nuwarapaksha, S. S. Udumann, N. S. Dissanayaka, R. M. N. Dilshan, and A. J. Atapattu, *Revolutionizing Agriculture by Advanced Water and Irrigation Management Technologies*. IGI Global, Dec. 2024, p. 285–318. [Online]. Available: http://dx.doi.org/10.4018/979-8-3693-6920-3.ch009 (Cited on pages ix, 34, 35, and 36)

[14] B. Geldhof, J. Pattyn, D. Eyland, S. Carpentier, and B. Van de Poel, "A digital sensor to measure real-time leaf movements and detect abiotic stress in plants," *Plant Physiology*, vol. 187, no. 3, p. 1131–1148, Aug. 2021. [Online]. Available: http://dx.doi.org/10.1093/plphys/kiab407 (Cited on pages xi, 33, 85, and 90)

[15] M. Gassara, M. Elleuchi, and M. Abid, "Cloud-based platforms for lora internet of things: a survey," *International Journal of Informatics and Communication Technology (IJ-ICT)*, vol. 10, no. 1, p. 54, Apr. 2021. [Online]. Available: http://dx.doi.org/10.11591/ijict.v10i1.pp54-64 (Cited on pages xiii, 37, and 39)

[16] K. Mekki, E. Bajic, F. Chaxel, and F. Meyer, "A comparative study of lpwan technologies for large-scale iot deployment," *ICT Express*, vol. 5, no. 1, p. 1–7, Mar. 2019. [Online]. Available: http://dx.doi.org/10.1016/j.icte.2017.12.005 (Cited on pages xiii and 39)

[17] J. Rockström, W. Steffen, K. Noone, Persson, F. S. Chapin, E. F. Lambin, T. M. Lenton, M. Scheffer, C. Folke, H. J. Schellnhuber, B. Nykvist, C. A. de Wit, T. Hughes, S. van der Leeuw, H. Rodhe, S. Sörlin, P. K. Snyder, R. Costanza, U. Svedin, M. Falkenmark, L. Karlberg, R. W. Corell, V. J. Fabry, J. Hansen, B. Walker, D. Liverman, K. Richardson, P. Crutzen, and J. A. Foley, "A safe operating space for humanity," *Nature*, vol. 461, no. 7263, p. 472–475, Sep. 2009. [Online]. Available: http://dx.doi.org/10.1038/461472a (Cited on page 1)

[18] J. S. Famiglietti, "The global groundwater crisis," *Nature Climate Change*, vol. 4, no. 11, p. 945–948, Oct. 2014. [Online]. Available: http://dx.doi.org/10.1038/nclimate2425 (Cited on page 1)

[19] A. Nilahyane, R. Ghimire, B. Sharma Acharya, M. E. Schipanski, C. P. West, and A. K. Obour, "Overcoming agricultural sustainability challenges in water-limited environments through soil health and water conservation: insights from the ogallala aquifer region, usa," *International Journal of Agricultural Sustainability*, vol. 21, no. 1, May 2023. [Online]. Available: http://dx.doi.org/10.1080/14735903.2023.2211484 (Cited on page 1)

[20] R. Lal, "Soil health and carbon management," *Food and Energy Security*, vol. 5, no. 4, p. 212–222, Nov. 2016. [Online]. Available: http://dx.doi.org/10.1002/fes3.96 (Cited on page 1)

[21] G. Schaible and M. Aillery, "Water conservation in irrigated agriculture: Trends and challenges in the face of emerging demands," *SSRN Electronic Journal*, 2012. [Online]. Available: http://dx.doi.org/10.2139/ssrn.2186555 (Cited on page 1)

[22] Y. Ma, J. Wang, and M. Zhu, "Research on optimization strategy of agricultural water conservancy costs based on clustering algorithm," *Applied Mathematics and Nonlinear Sciences*, vol. 9, no. 1, Jan. 2024. [Online]. Available: http://dx.doi.org/10.2478/amns-2024-3629 (Cited on page 1)

[23] K. E. Trenberth, A. Dai, G. van der Schrier, P. D. Jones, J. Barichivich, K. R. Briffa, and J. Sheffield, "Global warming and changes in drought," *Nature Climate Change*, vol. 4, no. 1, p. 17–22, Dec. 2013. [Online]. Available: http://dx.doi.org/10.1038/nclimate2067 (Cited on page 1)

[24] J. V. Stafford, "Implementing precision agriculture in the 21st century," *Journal of Agricultural Engineering Research*, vol. 76, no. 3, p. 267–275, Jul. 2000. [Online]. Available: http://dx.doi.org/10.1006/jaer.2000.0577 (Cited on pages 1 and 36)

[25] R. K. Sidhu, R. Kumar, P. Rana, and M. Jat, "Automation in drip irrigation for enhancing water-use efficiency in cereal systems of south asia: Status and prospects," in *Advances in Water Resources*. Academic Press, 2021, vol. 155, pp. 103–124. [Online]. Available: https://www.sciencedirect.com/science/article/abs/pii/S0065211321000286 (Cited on pages 1 and 34)

[26] K. TAKATA, "Aquaporins: water channel proteins of the cell membrane," *Progress in Histochemistry and Cytochemistry*, vol. 39, no. 1, p. 1–83, May 2004. [Online]. Available: http://dx.doi.org/10.1016/j.proghi.2004.03.001 (Cited on page 4)

[27] D. T. Clarkson, "Roots and the delivery of solutes to the xylem," *Philosophical Transactions of the Royal Society of London. Series B: Biological Sciences*, vol. 341, no. 1295, pp. 5–17, Jul 1993, published 29 July 1993. [Online]. Available: https://royalsocietypublishing.org/doi/10.1098/rstb.1993.0086 (Cited on page 4)

[28] A. A. Salih, I. A. Ali, A. Lux, M. Luxová, Y. Cohen, Y. Sugimoto, and S. Inanaga, "Rooting, water uptake, and xylem structure adaptation to drought of two sorghum cultivars," *Crop Science*, vol. 39, no. 1, p. 168–173, Jan. 1999. [Online]. Available: http://dx.doi.org/10.2135/cropsci1999.0011183X003900010027x (Cited on page 4)

[29] T. N. Buckley, G. P. John, C. Scoffoni, and L. Sack, "How does leaf anatomy influence water transport outside the xylem?" *Plant Physiology*, vol. 168, no. 4, p. 1616–1635, Jun. 2015. [Online]. Available: http://dx.doi.org/10.1104/pp.15.00731 (Cited on page 4)

[30] S. Perilli, R. Di Mambro, and S. Sabatini, "Growth and development of the root apical meristem," *Current Opinion in Plant Biology*, vol. 15, no. 1, p. 17–23, Feb. 2012. [Online]. Available: http://dx.doi.org/10.1016/j.pbi.2011.10.006 (Cited on page 4)

[31] M. M. Caldwell, "Root extension and water absorption," in *Water and Plant Life: Problems and Modern Approaches*, ser. Ecological Studies, O. L. Lange, L. Kappen, and E. D. Schulze, Eds. Berlin, Heidelberg: Springer, 1976, vol. 19, pp. 63–85, part of the Ecological Studies book series (ECOLSTUD, volume 19). [Online]. Available: https://link.springer.com/chapter/10.1007/978-3-642-66429-8_5 (Cited on page 4)

[32] A. Carminati, M. Zarebanadkouki, E. Kroener, M. A. Ahmed, and M. Holz, "Biophysical rhizosphere processes affecting root water uptake," *Annals of Botany*, vol. 118, no. 4, p. 561–571, Jun. 2016. [Online]. Available: http://dx.doi.org/10.1093/aob/mcw113 (Cited on pages 4 and 11)

[33] M. Shafiei, R. Kumar, and K. Karimi, "Pretreatment of lignocellulosic biomass," in *Lignocellulose-Based Bioproducts*, ser. Biofuel and Biorefinery Technologies, K. Karimi, Ed. Cham: Springer, 2015, vol. 1, pp. 85–154, first Online: 01 January 2015. [Online]. Available: https://link.springer.com/chapter/10.1007/978-3-319-14033-9_3 (Cited on pages 4 and 5)

[34] P. Nortes, A. Pérez-Pastor, G. Egea, W. Conejero, and R. Domingo, "Comparison of changes in stem diameter and water potential values for detecting water stress in young almond trees," *Agricultural Water Management*, vol. 77, no. 1–3, p. 296–307, Aug. 2005. [Online]. Available: http://dx.doi.org/10.1016/J.AGWAT.2004.09.034 (Cited on page 5)

[35] T. MCBURNEY and P. A. COSTIGAN, "The relationship between stem diameter and water potentials in stems of young cabbage plants," *Journal of Experimental Botany*, vol. 35, no. 12, p. 1787–1793, 1984. [Online]. Available: http://dx.doi.org/10.1093/jxb/35.12.1787 (Cited on page 5)

[36] X. Zhang, H. Li, H. Liu, J. Wang, and X. Qiang, "Response of tomato quality parameters to water deficit under soil salinity and simulation based on stem water potential," *Horticulturae*, vol. 11, no. 2, p. 114, Jan. 2025. [Online]. Available: http://dx.doi.org/10.3390/horticulturae11020114 (Cited on page 5)

[37] L. Sossountzov, "Structure et fonctionnement du méristème apical des ptéridophytes : présent et avenir," *Bulletin de la Société Botanique de France*, vol. 119, no. 5-6, pp. 341–352, 1972. [Online]. Available: https://www.tandfonline.com/doi/abs/10.1080/00378941.1972.10839038 (Cited on page 5)

[38] S. A. Braybrook and C. Kuhlemeier, "How a plant builds leaves," *The Plant Cell*, vol. 22, no. 4, p. 1006–1018, Apr. 2010. [Online]. Available: http://dx.doi.org/10.1105/tpc.110.073924 (Cited on page 5)

[39] F. W. Went, "Auxin, the plant growth-hormone," *The Botanical Review*, vol. 1, no. 5, p. 162–182, May 1935. [Online]. Available: http://dx.doi.org/10.1007/BF02870150 (Cited on page 5)

[40] Z. Yang, J. Xia, J. Hong, C. Zhang, H. Wei, W. Ying, C. Sun, L. Sun, Y. Mao, Y. Gao, S. Tan, J. Friml, D. Li, X. Liu, and L. Sun, "Structural insights into auxin recognition and efflux by arabidopsis pin1," *Nature*, vol. 609, no. 7927, p. 611–615, Aug. 2022. [Online]. Available: http://dx.doi.org/10.1038/s41586-022-05143-9 (Cited on page 5)

[41] S. Descomps, "Action de l'éclairement continu sur l'appareil photosynthétique du melon et de la tomate," *Bulletin de la Société Botanique de France. Lettres Botaniques*, vol. 133, no. 4-5, pp. 327–342, 1986. [Online]. Available: https://www.tandfonline.com/doi/abs/10.1080/01811797.1986.10824717 (Cited on page 5)

[42] D. Wilson, "Effect of light intensity and co_2 on apparent photosynthesis and its relationship with leaf anatomy in genotypes of *Lolium perenne* l." *New Phytologist*, vol. 68, no. 3, pp. 627–644, 1969. [Online]. Available: https://nph.onlinelibrary.wiley.com/doi/10.1111/j.1469-8137.1969.tb06467.x (Cited on page 5)

[43] R. Oguchi, Y. Onoda, I. Terashima, and D. Tholen, "Leaf anatomy and function," in *The Leaf: A Platform for Performing Photosynthesis*, ser. Advances in Photosynthesis and Respiration, W. W. I. Adams and I. Terashima, Eds. Cham: Springer, 2018, vol. 44, pp. 97–139, first Online: 25 October 2018. [Online]. Available: https://link.springer.com/chapter/10.1007/978-3-319-93594-2_5 (Cited on page 5)

[44] H. Miyake, "Starch accumulation in the bundle sheaths of c3plants: A possible pre-condition for c4photosynthesis," *Plant and Cell Physiology*, vol. 57, no. 5, p. 890–896, Mar. 2016. [Online]. Available: http://dx.doi.org/10.1093/pcp/pcw046 (Cited on page 6)

[45] H. Bauwe, "Photosynthetic enzyme activities and immunofluorescence studies on the localization of ribulose-1,5-bisphosphate carboxylase/oxygenase in leaves of c3, c4, and c3c4 intermediate species of flaveria (asteraceae)," *Biochemie und Physiologie der Pflanzen*, vol. 179, no. 4, p. 253–268, Jan. 1984. [Online]. Available: http://dx.doi.org/10.1016/S0015-3796(84)80041-4 (Cited on page 6)

[46] J. Males and H. Griffiths, "Stomatal biology of cam plants," *Plant Physiology*, vol. 174, no. 2, p. 550–560, Feb. 2017. [Online]. Available: http://dx.doi.org/10.1104/pp.17.00114 (Cited on page 6)

[47] R. T. Furbank and C. Foyer, "C_4 plants as valuable model experimental systems for the study of photosynthesis," *New Phytologist*, vol. 109, no. 3, pp. 265–277, 1988. [Online]. Available: https://nph.onlinelibrary.wiley.com/doi/10.1111/j.1469-8137.1988.tb04195.x (Cited on page 6)

[48] R. Ceulemans, I. Impens, and V. Steenackers, "Stomatal and anatomical leaf characteristics of 10 populus clones," *Canadian Journal of Botany*, vol. 62, no. 3, p. 513–518, Mar. 1984. [Online]. Available: http://dx.doi.org/10.1139/b84-076 (Cited on page 6)

[49] J. H. Grabber and G. A. Jung, "Isolation of parenchyma and sclerenchyma cell types from the plant parts of grasses," *Crop*

Science, vol. 31, no. 3, p. 838–842, May 1991. [Online]. Available: http://dx.doi.org/10.2135/cropsci1991.0011183X003100030058x (Cited on pages 6 and 7)

[50] E. Merilo, I. Jõesaar, M. Brosché, and H. Kollist, "To open or to close: species-specific stomatal responses to simultaneously applied opposing environmental factors," *New Phytologist*, vol. 202, no. 2, p. 499–508, Jan. 2014. [Online]. Available: http://dx.doi.org/10.1111/nph.12667 (Cited on pages 6 and 7)

[51] A. Heintz and A. Piatnitski, "Osmosis for non-electrolyte solvents in permeable periodic porous media," *Networks and Heterogeneous Media*, vol. 11, no. 3, p. 471–499, Aug. 2016. [Online]. Available: http://dx.doi.org/10.3934/nhm.2016005 (Cited on pages 6, 7, and 8)

[52] Q. Chai, Y. Gan, C. Zhao, H.-L. Xu, R. M. Waskom, Y. Niu, and K. H. M. Siddique, "Regulated deficit irrigation for crop production under drought stress. a review," *Agronomy for Sustainable Development*, vol. 36, no. 1, Dec. 2015. [Online]. Available: http://dx.doi.org/10.1007/s13593-015-0338-6 (Cited on pages 7, 8, 11, and 29)

[53] C. Bartell, H. K. Bayabil, B. Schaffer, F. Tilahun, and F. Getachew, "Measuring leaf water potential," UF/IFAS Extension, University of Florida, Tech. Rep. AE563, oct 2021, department of Agricultural and Biological Engineering; Published October 13, 2021. [Online]. Available: https://edis.ifas.ufl.edu/publication/AE563 (Cited on page 9)

[54] R. I. Papendick and G. S. Campbell, "Theory and measurement of water potential," in *Water Potential Relations in Soil Microbiology*, ser. SSSA Special Publication, J. F. Parr, W. R. Gardner, and L. F. Elliott, Eds. Madison, WI: Soil Science Society of America, 1981, no. 9, pp. 1–22. [Online]. Available: https://acsess.onlinelibrary.wiley.com/doi/10.2136/sssaspecpub9.c1 (Cited on page 9)

[55] I. R. Cowan, "Transport of water in the soil-plant-atmosphere system," *The Journal of Applied Ecology*, vol. 2, no. 1, p. 221, May 1965. [Online]. Available: http://dx.doi.org/10.2307/2401706 (Cited on page 9)

[56] M. M. González-Real, H.-Q. Liu, and A. Baille, "Influence of fruit sink strength on the distribution of leaf photosynthetic traits in fruit-bearing shoots of pepper plants (*Capsicum annuum* l.)," *Environmental and*

Experimental Botany, vol. 66, no. 2, pp. 195–202, 2009. [Online]. Available: https://doi.org/10.1016/j.envexpbot.2009.01.005 (Cited on page 10)

[57] V. Parkash and S. Singh, "A review on potential plant-based water stress indicators for vegetable crops," *Sustainability*, vol. 12, no. 10, p. 3945, May 2020. [Online]. Available: http://dx.doi.org/10.3390/su12103945 (Cited on pages 10, 11, and 16)

[58] R. Liao, S. Zhang, X. Zhang, M. Wang, H. Wu, and L. Zhangzhong, "Development of smart irrigation systems based on real-time soil moisture data in a greenhouse: Proof of concept," *Agricultural Water Management*, vol. 245, p. 106632, Feb. 2021. [Online]. Available: http://dx.doi.org/10.1016/j.agwat.2020.106632 (Cited on page 11)

[59] S. Merrium, Z. Ali, M. Habib-ur Rahman, S. Hakeem, and M. A. Khalid, "Leaf rolling and leaf angle improve fog capturing and transport in wheat; adaptation for drought stress in an arid climate," *Botanical Studies*, vol. 63, no. 1, p. 13, May 2022, published 16 May 2022; Received 05 Jan 2022; Accepted 27 Apr 2022. [Online]. Available: https://as-botanicalstudies.springeropen.com/articles/10.1186/s40529-022-00343-y (Cited on page 11)

[60] J.-F. Briat, K. Ravet, N. Arnaud, C. Duc, J. Boucherez, B. Touraine, F. Cellier, and F. Gaymard, "New insights into ferritin synthesis and function highlight a link between iron homeostasis and oxidative stress in plants," *Annals of Botany*, vol. 105, no. 5, p. 811–822, May 2009. [Online]. Available: http://dx.doi.org/10.1093/aob/mcp128 (Cited on pages 11 and 14)

[61] I. Ensminger, F. Busch, and N. P. A. Huner, "Photostasis and cold acclimation: sensing low temperature through photosynthesis," *Physiologia Plantarum*, vol. 126, no. 1, pp. 28–44, 2006. [Online]. Available: https://onlinelibrary.wiley.com/doi/10.1111/j.1399-3054.2006.00627.x (Cited on pages 11 and 14)

[62] M. K. Bartlett, C. Scoffoni, R. Ardy, Y. Zhang, S. Sun, K. Cao, and L. Sack, "Rapid determination of comparative drought tolerance traits: using an osmometer to predict turgor loss point," *Methods in Ecology and Evolution*, vol. 3, no. 5, p. 880–888, Jul. 2012. [Online]. Available: http://dx.doi.org/10.1111/j.2041-210X.2012.00230.x (Cited on pages 11 and 15)

[63] J. J. Schwinefus, C. Checkal, B. Saksa, N. Baka, K. Modi, and C. Rivera, "Molar mass and second virial coefficient of polyethylene glycol by vapor pressure osmometry," *Journal of Chemical Education*, vol. 92, no. 12, p. 2157–2160, Sep. 2015. [Online]. Available: http://dx.doi.org/10.1021/acs.jchemed.5b00369 (Cited on pages 11 and 15)

[64] R. Ball and D. Oosterhuis, "Measurement of root and leaf osmotic potential using the vapor-pressure osmometer," *Environmental and Experimental Botany*, vol. 53, no. 1, p. 77–84, Feb. 2005. [Online]. Available: http://dx.doi.org/10.1016/j.envexpbot.2004.03.003 (Cited on pages 11 and 15)

[65] M. Z. Liu, G. M. Jiang, Y. G. Li, S. L. Niu, L. M. Gao, L. Ding, and Y. Peng, "Leaf osmotic potentials of 104 plant species in relation to habitats and plant functional types in hunshandak sandland, inner mongolia, china," *Trees*, vol. 17, no. 6, p. 554–560, Jun. 2003. [Online]. Available: http://dx.doi.org/10.1007/s00468-003-0277-8 (Cited on page 11)

[66] Q. Sun, L. Lai, J. Zhou, S. Yi, X. Liu, J. Guo, and Y. Zheng, "Differences in ecological traits between plants grown in situ and ex situ and implications for conservation," *Sustainability*, vol. 14, no. 9, p. 5199, Apr. 2022. [Online]. Available: http://dx.doi.org/10.3390/su14095199 (Cited on page 11)

[67] A. Verhoef, "The effect of temperature differences between porometer head and leaf surface on stomatal conductance measurements," *Plant, Cell and Environment*, vol. 20, no. 5, pp. 641–646, 1997. [Online]. Available: https://onlinelibrary.wiley.com/doi/10.1111/j.1365-3040.1997.00098.x (Cited on pages 11 and 16)

[68] I. G. Cummings, J. B. Reid, and A. Koutoulis, "Red to far-red ratio correction in plant growth chambers—growth responses and influence of thermal load on garden pea," *Physiologia Plantarum*, vol. 131, no. 2, pp. 171–179, oct 2007. [Online]. Available: https://onlinelibrary.wiley.com/doi/10.1111/j.1399-3054.2007.00958.x (Cited on pages 11 and 16)

[69] D. Grossi, F. Emanuelli, G. Di Lorenzo, L. Brancadoro, O. Failla, M. Grando, and A. Scienza, "Methods to dissect grapevine rootstocks responses to drought stress," *Acta Horticulturae*, no. 1136, p. 229–234, Jul. 2016. [Online]. Available: http://dx.doi.org/10.17660/ActaHortic.2016.1136.31 (Cited on pages 11 and 16)

[70] M. M. Caldwell, "Root extension and water absorption," in *Water and Plant Life: Problems and Modern Approaches*, ser. Ecological Studies, O. L. Lange, L. Kappen, and E.-D. Schulze, Eds. Berlin, Heidelberg: Springer, 1976, vol. 19, pp. 63–85, part of the Ecological Studies book series (ECOLSTUD, volume 19). [Online]. Available: https://link.springer.com/chapter/10.1007/978-3-642-66429-8_5 (Cited on page 11)

[71] Y. Osakabe, K. Osakabe, K. Shinozaki, and L.-S. P. Tran, "Response of plants to water stress," *Frontiers in Plant Science*, vol. 5, Mar. 2014. [Online]. Available: http://dx.doi.org/10.3389/fpls.2014.00086 (Cited on page 11)

[72] F. N. Dalton, W. N. Herkelrath, D. S. Rawlins, and J. D. Rhoades, "Time-domain reflectometry: Simultaneous measurement of soil water content and electrical conductivity with a single probe," *Science*, vol. 224, no. 4652, p. 989–990, Jun. 1984. [Online]. Available: http://dx.doi.org/10.1126/science.224.4652.989 (Cited on page 11)

[73] P. F. Scholander, E. D. Bradstreet, E. A. Hemmingsen, and H. T. Hammel, "Sap pressure in vascular plants: Negative hydrostatic pressure can be measured in plants." *Science*, vol. 148, no. 3668, p. 339–346, Apr. 1965. [Online]. Available: http://dx.doi.org/10.1126/science.148.3668.339 (Cited on pages 12 and 45)

[74] M. J. Powell, "Ultrastructural changes in nuclear membranes and organelle associations during mitosis of the aquatic fungus entophlyctis sp." *Canadian Journal of Botany*, vol. 53, no. 7, p. 627–646, Apr. 1975. [Online]. Available: http://dx.doi.org/10.1139/b75-078 (Cited on page 12)

[75] C. M. Rodriguez-Dominguez, A. Forner, S. Martorell, B. Choat, R. Lopez, J. M. R. Peters, S. Pfautsch, S. Mayr, M. R. Carins-Murphy, S. A. M. McAdam, F. Richardson, A. Diaz-Espejo, V. Hernandez-Santana, P. E. Menezes-Silva, J. M. Torres-Ruiz, T. A. Batz, and L. Sack, "Leaf water potential measurements using the pressure chamber: Synthetic testing of assumptions towards best practices for precision and accuracy," *Plant, Cell amp; Environment*, vol. 45, no. 7, p. 2037–2061, Apr. 2022. [Online]. Available: http://dx.doi.org/10.1111/pce.14330 (Cited on page 12)

[76] A. BENZIONI and C. ITAI, "Preconditioning of tobacco and bean leaves to heat shock by high temperature or nacl," *Physiologia*

Plantarum, vol. 35, no. 2, p. 80–84, Oct. 1975. [Online]. Available: http://dx.doi.org/10.1111/j.1399-3054.1975.tb03872.x (Cited on page 13)

[77] A. D. Boursianis, M. S. Papadopoulou, P. Diamantoulakis, A. Liopa-Tsakalidi, P. Barouchas, G. Salahas, G. Karagiannidis, S. Wan, and S. K. Goudos, "Internet of things (iot) and agricultural unmanned aerial vehicles (uavs) in smart farming: A comprehensive review," *Internet of Things*, vol. 18, p. 100187, May 2022. [Online]. Available: http://dx.doi.org/10.1016/j.iot.2020.100187 (Cited on pages 15 and 35)

[78] O. Ali, I. Cheddadi, B. Landrein, and Y. Long, "Revisiting the relationship between turgor pressure and plant cell growth," *New Phytologist*, vol. 238, no. 1, p. 62–69, Jan. 2023. [Online]. Available: http://dx.doi.org/10.1111/nph.18683 (Cited on page 15)

[79] H. G. L. Coster, E. Steudle, and U. Zimmermann, "Turgor pressure sensing in plant cell membranes," *Plant Physiology*, vol. 58, no. 5, p. 636–643, Nov. 1976. [Online]. Available: http://dx.doi.org/10.1104/pp.58.5.636 (Cited on page 15)

[80] C. Ballester, M. Castiella, U. Zimmermann, S. Rüger, M. Martínez Gimeno, and D. Intrigliolo, "Usefulness of the zim-probe technology for detecting water stress in clementine and persimmon trees," *Acta Horticulturae*, no. 1150, p. 105–112, Jan. 2017. [Online]. Available: http://dx.doi.org/10.17660/ActaHortic.2017.1150.15 (Cited on page 15)

[81] V. Gonzalez-Dugo and P. J. Zarco-Tejada, "Assessing the impact of measurement errors in the calculation of cwsi for characterizing the water status of several crop species," *Irrigation Science*, vol. 42, no. 3, p. 431–443, Aug. 2022. [Online]. Available: http://dx.doi.org/10.1007/s00271-022-00819-6 (Cited on pages 16 and 19)

[82] J. Diaz-Pérez, K. Shackel, and E. Sutter, "Relative water content and water potential of tissue 1," *Journal of Experimental Botany*, vol. 46, no. 1, p. 111–118, 1995. [Online]. Available: http://dx.doi.org/10.1093/jxb/46.1.111 (Cited on pages 16 and 45)

[83] J. Martínez, H. Silva, J. Ledent, and M. Pinto, "Effect of drought stress on the osmotic adjustment, cell wall elasticity and cell volume of six cultivars of common beans (phaseolus vulgaris l.)," *European Journal of Agronomy*, vol. 26, no. 1, p. 30–38, Jan. 2007. [Online]. Available: http://dx.doi.org/10.1016/j.eja.2006.08.003 (Cited on pages 16, 45, and 70)

[84] J. M. Bennett, K. J. Boote, and L. C. Hammond, "Relationships among water potential components, relative water content, and stomatal resistance of field-grown peanut leaves1," *Peanut Science*, vol. 11, no. 1, p. 31–35, Jan. 1984. [Online]. Available: http://dx.doi.org/10.3146/i0095-3679-11-1-10 (Cited on pages 16 and 45)

[85] L. González and M. González-Vilar, "Determination of relative water content," in *Handbook of Plant Ecophysiology Techniques*, M. J. Reigosa Roger, Ed. Dordrecht: Springer, 2001, pp. 207–212, online ISBN: 978-0-306-48057-7. [Online]. Available: https://link.springer.com/chapter/10.1007/0-306-48057-3_14 (Cited on page 16)

[86] R. E. Smart and G. E. Bingham, "Rapid estimates of relative water content," *Plant Physiology*, vol. 53, no. 2, p. 258–260, Feb. 1974. [Online]. Available: http://dx.doi.org/10.1104/pp.53.2.258 (Cited on pages 16 and 45)

[87] P. E. WEATHERLEY, "A porometer for use in the field," *New Phytologist*, vol. 65, no. 3, p. 376–387, Jul. 1966. [Online]. Available: http://dx.doi.org/10.1111/j.1469-8137.1966.tb06374.x (Cited on page 16)

[88] V. B. Koman, M. Park, T. T. S. Lew, S. Wan, E. S. Yarwood, X. Gong, T. S. Shikdar, R. J. Oliver, J. Cui, P. Gordiichuk, R. Sarojam, and M. S. Strano, "Emerging investigator series: linking nanoparticle infiltration and stomatal dynamics for plant nanobionics," *Environmental Science: Nano*, vol. 9, no. 4, p. 1236–1246, 2022. [Online]. Available: http://dx.doi.org/10.1039/D1EN01154E (Cited on page 17)

[89] R. Chen, S. Ren, S. Li, D. Han, K. Qin, X. Jia, H. Zhou, and Z. Gao, "Recent advances and prospects in wearable plant sensors," *Reviews in Environmental Science and Bio/Technology*, vol. 22, no. 4, p. 933–968, Aug. 2023. [Online]. Available: http://dx.doi.org/10.1007/s11157-023-09667-y (Cited on page 17)

[90] H. Lin, Y. Chen, H. Zhang, P. Fu, and Z. Fan, "Stronger cooling effects of transpiration and leaf physical traits of plants from a hot dry habitat than from a hot wet habitat," *Functional Ecology*, vol. 31, no. 12, p. 2202–2211, Jul. 2017. [Online]. Available: http://dx.doi.org/10.1111/1365-2435.12923 (Cited on page 18)

[91] S. K. Gupta, J. Ram, and H. Singh, "Comparative study of transpiration in cooling effect of tree species in the atmosphere," *Journal of Geoscience*

and Environment Protection, vol. 6, no. 8, pp. 151–166, Aug. 2018. [Online]. Available: https://www.scirp.org/journal/paperinformation?paperid=86938 (Cited on page 18)

[92] H. G. Jones, *Application of Thermal Imaging and Infrared Sensing in Plant Physiology and Ecophysiology*. Elsevier, 2004, p. 107–163. [Online]. Available: http://dx.doi.org/10.1016/S0065-2296(04)41003-9 (Cited on pages 19 and 20)

[93] N. Nadezhdina, "Sap flow index as an indicator of plant water status," *Tree Physiology*, vol. 19, no. 13, p. 885–891, Nov. 1999. [Online]. Available: http://dx.doi.org/10.1093/treephys/19.13.885 (Cited on page 20)

[94] J. Fernández, M. Palomo, A. Dıaz-Espejo, B. Clothier, S. Green, I. Girón, and F. Moreno, "Heat-pulse measurements of sap flow in olives for automating irrigation: tests, root flow and diagnostics of water stress," *Agricultural Water Management*, vol. 51, no. 2, p. 99–123, Oct. 2001. [Online]. Available: http://dx.doi.org/10.1016/S0378-3774(01)00119-6 (Cited on pages 20 and 22)

[95] J. L. Heitman, J. M. Basinger, G. J. Kluitenberg, J. M. Ham, J. M. Frank, and P. L. Barnes, "Field evaluation of the dual-probe heat-pulse method for measuring soil water content," *Vadose Zone Journal*, vol. 2, no. 4, p. 552–560, Nov. 2003. [Online]. Available: http://dx.doi.org/10.2136/vzj2003.5520 (Cited on page 20)

[96] D. Chen, Y. Wang, S. Liu, X. Wei, and X. Wang, "Response of relative sap flow to meteorological factors under different soil moisture conditions in rainfed jujube (ziziphus jujuba mill.) plantations in semiarid northwest china," *Agricultural Water Management*, vol. 136, p. 23–33, Apr. 2014. [Online]. Available: http://dx.doi.org/10.1016/j.agwat.2014.01.001 (Cited on page 20)

[97] G. Noun, M. Lo Cascio, D. Spano, S. Marras, and C. Sirca, "Plant-based methodologies and approaches for estimating plant water status of mediterranean tree species: A semi-systematic review," *Agronomy*, vol. 12, no. 9, p. 2127, Sep. 2022. [Online]. Available: http://dx.doi.org/10.3390/agronomy12092127 (Cited on page 20)

[98] N. C. Turner, "Techniques and experimental approaches for the measurement of plant water status," *Plant and Soil*, vol. 58, no. 1–3, p. 339–366, Feb.

1981. [Online]. Available: http://dx.doi.org/10.1007/BF02180062 (Cited on pages 20 and 21)

[99] I. Offenthaler, P. Hietz, and H. Richter, "Wood diameter indicates diurnal and long-term patterns of xylem water potential in norway spruce," *Trees*, vol. 15, no. 4, p. 215–221, Mar. 2001. [Online]. Available: http://dx.doi.org/10.1007/s004680100090 (Cited on page 21)

[100] T. Chan, T. Hölttä, F. Berninger, H. Mäkinen, P. Nöjd, M. Mencuccini, and E. Nikinmaa, "Separating water-potential induced swelling and shrinking from measured radial stem variations reveals a cambial growth and osmotic concentration signal," *Plant, Cell amp; Environment*, vol. 39, no. 2, p. 233–244, Apr. 2015. [Online]. Available: http://dx.doi.org/10.1111/pce.12541 (Cited on page 21)

[101] E. Garnier and A. Berger, "Effect of water stress on stem diameter changes of peach trees growing in the field," *The Journal of Applied Ecology*, vol. 23, no. 1, p. 193, Apr. 1986. [Online]. Available: http://dx.doi.org/10.2307/2403091 (Cited on pages 21 and 22)

[102] Z. Meng, A. Duan, D. Chen, K. B. Dassanayake, X. Wang, Z. Liu, H. Liu, and S. Gao, "Suitable indicators using stem diameter variation-derived indices to monitor the water status of greenhouse tomato plants," *PLOS ONE*, vol. 12, no. 2, p. e0171423, Feb. 2017. [Online]. Available: http://dx.doi.org/10.1371/journal.pone.0171423 (Cited on page 22)

[103] J. Ross and M. Sulev, "Sources of errors in measurements of par," *Agricultural and Forest Meteorology*, vol. 100, no. 2–3, p. 103–125, Feb. 2000. [Online]. Available: http://dx.doi.org/10.1016/S0168-1923(99)00144-6 (Cited on pages 22 and 88)

[104] M. I. N. ZHANG and J. H. M. WILLISON, "Electrical impedance analysis in plant tissues11," *Journal of Experimental Botany*, vol. 42, no. 11, p. 1465–1475, 1991. [Online]. Available: http://dx.doi.org/10.1093/jxb/42.11.1465 (Cited on page 22)

[105] ——, "Electrical impedance analysis in plant tissues8," *Journal of Experimental Botany*, vol. 44, no. 8, p. 1369–1375, 1993. [Online]. Available: http://dx.doi.org/10.1093/jxb/44.8.1369 (Cited on page 22)

[106] T. Repo, G. Zhang, A. Ryyppö, and R. Rikala, "The electrical impedance spectroscopy of scots pine (pinus sylvestris l.) shoots

in relation to cold acclimation," *Journal of Experimental Botany*, vol. 51, no. 353, p. 2095–2107, Dec. 2000. [Online]. Available: http://dx.doi.org/10.1093/jexbot/51.353.2095 (Cited on page 22)

[107] D. Jamaludin, S. Abd Aziz, D. Ahmad, and H. Z. Jaafar, "Impedance analysis of labisia pumila plant water status," *Information Processing in Agriculture*, vol. 2, no. 3–4, p. 161–168, Oct. 2015. [Online]. Available: http://dx.doi.org/10.1016/j.inpa.2015.07.004 (Cited on pages 22 and 23)

[108] R. Basak, K. A. Wahid, A. Dinh, R. Soolanayakanahally, R. Fotouhi, and A. S. Mehr, "Rapid and efficient determination of relative water contents of crop leaves using electrical impedance spectroscopy in vegetative growth stage," *Remote Sensing*, vol. 12, no. 11, p. 1753, May 2020. [Online]. Available: http://dx.doi.org/10.3390/rs12111753 (Cited on pages 23 and 29)

[109] P. Deurenberg, A. Andreoli, and A. de Lorenzo, "Multi-frequency bioelectrical impedance: a comparison between the cole-cole modelling and hanai equations with the classical impedance index approach," *Annals of Human Biology*, vol. 23, no. 1, p. 31–40, Jan. 1996. [Online]. Available: http://dx.doi.org/10.1080/03014469600004252 (Cited on page 23)

[110] F. R. Harker and J. H. Maindonald, "Ripening of nectarine fruit (changes in the cell wall, vacuole, and membranes detected using electrical impedance measurements)," *Plant Physiology*, vol. 106, no. 1, p. 165–171, Sep. 1994. [Online]. Available: http://dx.doi.org/10.1104/pp.106.1.165 (Cited on pages 23 and 24)

[111] U. KYLE, "Bioelectrical impedance analysis?part i: review of principles and methods," *Clinical Nutrition*, vol. 23, no. 5, p. 1226–1243, Oct. 2004. [Online]. Available: http://dx.doi.org/10.1016/j.clnu.2004.06.004 (Cited on page 23)

[112] A. D. Bauchot, F. Harker, and W. Arnold, "The use of electrical impedance spectroscopy to assess the physiological condition of kiwifruit," *Postharvest Biology and Technology*, vol. 18, no. 1, p. 9–18, Jan. 2000. [Online]. Available: http://dx.doi.org/10.1016/S0925-5214(99)00056-3 (Cited on page 24)

[113] A. R. Varlan and W. Sansen, "Nondestructive electrical impedance analysis in fruit: Normal ripening and injuries characterization," *Electro- and*

Magnetobiology, vol. 15, no. 3, p. 213–227, Jan. 1996. [Online]. Available: http://dx.doi.org/10.3109/15368379609012878 (Cited on page 24)

[114] J. J. Ackmann and M. A. Seitz, "Methods of complex impedance measurements in biologic tissue," *Critical Reviews in Biomedical Engineering*, vol. 11, no. 4, pp. 281–311, 1984, pMID: 6391815. [Online]. Available: https://pubmed.ncbi.nlm.nih.gov/6391815/ (Cited on pages 24 and 48)

[115] C. C. Murdock and E. E. Zimmerman, "Polarization impedance at low frequencies," *Physics*, vol. 7, no. 6, p. 211–219, Jun. 1936. [Online]. Available: http://dx.doi.org/10.1063/1.1745387 (Cited on page 24)

[116] S. A. R. Mousavi, C. T. Nguyen, E. E. Farmer, and S. Kellenberger, "Measuring surface potential changes on leaves," *Nature Protocols*, vol. 9, no. 8, p. 1997–2004, Jul. 2014. [Online]. Available: http://dx.doi.org/10.1038/nprot.2014.136 (Cited on page 24)

[117] F. Postic and C. Doussan, "Benchmarking electrical methods for rapid estimation of root biomass," *Plant Methods*, vol. 12, no. 1, Jun. 2016. [Online]. Available: http://dx.doi.org/10.1186/s13007-016-0133-7 (Cited on pages 24 and 48)

[118] R. van Es, J. Hauck, V. J. H. M. van Driel, K. Neven, H. van Wessel, P. A. Doevendans, and F. H. M. Wittkampf, "Novel method for electrode-tissue contact measurement with multi-electrode catheters," *EP Europace*, vol. 20, no. 1, pp. 149–156, jan 2018, published online 7 Jan 2017; PMID: 28064250. [Online]. Available: https://academic.oup.com/europace/article/20/1/149/2863965 (Cited on page 24)

[119] A. Sureshkumar and R. Gunabalan, "Design of robust guaranteed margin stability region pi controller for automotive led lighting with parameter uncertainty," *IEEE Access*, vol. 10, p. 15657–15670, 2022. [Online]. Available: http://dx.doi.org/10.1109/ACCESS.2022.3146392 (Cited on page 24)

[120] M. Zhang, T. Repo, J. Willison, and S. Sutinen, "Electrical impedance analysis in plant tissues: on the biological meaning of cole-cole? in scots pine needles," *European Biophysics Journal*, vol. 24, no. 2, Oct. 1995. [Online]. Available: http://dx.doi.org/10.1007/BF00211405 (Cited on page 25)

[121] S. Grimnes and O. Martinsen, "Cole electrical impedance model—a critique and an alternative," *IEEE Transactions on Biomedical Engineering*, vol. 52, no. 1, p. 132–135, Jan. 2005. [Online]. Available: http://dx.doi.org/10.1109/TBME.2004.836499 (Cited on page 25)

[122] R. I. HAYDEN, C. A. MOYSE, F. W. CALDER, D. P. CRAWFORD, and D. S. FENSOM, "Electrical impedance studies on potato and alfalfa tissue," *Journal of Experimental Botany*, vol. 20, no. 2, p. 177–200, 1969. [Online]. Available: http://dx.doi.org/10.1093/jxb/20.2.177 (Cited on page 25)

[123] Y. Liu, X. Ma, L. Shu, G. P. Hancke, and A. M. Abu-Mahfouz, "From industry 4.0 to agriculture 4.0: Current status, enabling technologies, and research challenges," *IEEE Transactions on Industrial Informatics*, vol. 17, no. 6, p. 4322–4334, Jun. 2021. [Online]. Available: http://dx.doi.org/10.1109/TII.2020.3003910 (Cited on pages 26 and 36)

[124] F. Kovács, Odry, Z. Vizvári, S. Kabalan, E. Papdi, P. Odry, and K. Juhos, "A novel approach to water stress assessment in plants: New bioimpedance method with pso-optimized cole-cole impedance modeling," *Computers and Electronics in Agriculture*, vol. 234, p. 110167, Jul. 2025. [Online]. Available: http://dx.doi.org/10.1016/j.compag.2025.110167 (Cited on page 27)

[125] T. Repo, Y. Cao, R. Silvennoinen, and H. Ozier-Lafontaine, *Electrical Impedance Spectroscopy and Roots*. Springer Berlin Heidelberg, Oct. 2011, p. 25–49. [Online]. Available: http://dx.doi.org/10.1007/978-3-642-22067-8_2 (Cited on page 28)

[126] M. K. Transtrum and J. P. Sethna, "Improvements to the levenberg–marquardt algorithm for nonlinear least-squares minimization," *arXiv preprint arXiv:1201.5885*, 2012. [Online]. Available: https://arxiv.org/abs/1201.5885 (Cited on page 28)

[127] M. Van Haeverbeke, B. De Baets, and M. Stock, "Plant impedance spectroscopy: a review of modeling approaches and applications," *Frontiers in Plant Science*, vol. 14, Jul. 2023. [Online]. Available: http://dx.doi.org/10.3389/fpls.2023.1187573 (Cited on pages 29, 72, and 73)

[128] R. L. Cooper, M. A. Thomas, and D. N. McLetchie, "Impedance measures for detecting electrical responses during acute injury and exposure of compounds to roots of plants," *Methods and Protocols*, vol. 5, no. 4, p. 56,

Jun. 2022. [Online]. Available: http://dx.doi.org/10.3390/mps5040056 (Cited on page 29)

[129] W. J. Pech-Rodríguez, G. G. Suarez-Velázquez, E. N. Armendáriz-Mireles, C. A. Calles-Arriaga, and E. Rocha-Rangel, "Performance assessment of heuristic genetic algorithm (hga) for electrochemical impedance spectroscopy parameter estimation," *Axioms*, vol. 12, no. 1, p. 84, Jan. 2023. [Online]. Available: http://dx.doi.org/10.3390/axioms12010084 (Cited on page 29)

[130] S. Simondi, E. Casaretto, G. Quero, S. Ceretta, V. Bonnecarrère, and O. Borsani, "A simple and accurate method based on a water-consumption model for phenotyping soybean genotypes under hydric deficit conditions," *Agronomy*, vol. 12, no. 3, p. 575, Feb. 2022. [Online]. Available: http://dx.doi.org/10.3390/agronomy12030575 (Cited on page 29)

[131] J. C. Nouaze, J. H. Kim, G. R. Jeon, and J. H. Kim, "Monitoring of indoor farming of lettuce leaves for 16 hours using electrical impedance spectroscopy (eis) and double-shell model (dsm)," *Sensors*, vol. 22, no. 24, p. 9671, Dec. 2022. [Online]. Available: http://dx.doi.org/10.3390/s22249671 (Cited on pages 29 and 81)

[132] H. Gan, C. Xu, W. Hou, J. Guo, K. Liu, and Y. Xue, "Spatiotemporal graph convolutional network for automated detection and analysis of social behaviours among pre-weaning piglets," *Biosystems Engineering*, vol. 217, p. 102–114, May 2022. [Online]. Available: http://dx.doi.org/10.1016/j.biosystemseng.2022.03.005 (Cited on page 29)

[133] J. Cui, M. Sawut, N. Ailijiang, A. Manlike, and X. Hu, "Estimation of leaf water content of a fruit tree by in situ vis-nir spectroscopy using multiple machine learning methods in southern xinjiang, china," *Agronomy*, vol. 14, no. 8, p. 1664, 2024, published 29 July 2024. [Online]. Available: https://www.mdpi.com/2073-4395/14/8/1664 (Cited on page 29)

[134] R. DE BEI, D. COZZOLINO, W. SULLIVAN, W. CYNKAR, S. FUENTES, R. DAMBERGS, J. PECH, and S. TYERMAN, "Non-destructive measurement of grapevine water potential using near infrared spectroscopy: Measure of grapevine water potential using nir," *Australian Journal of Grape and Wine Research*, vol. 17, no. 1, p. 62–71, Dec. 2010. [Online]. Available: http://dx.doi.org/10.1111/j.1755-0238.2010.00117.x (Cited on pages 30, 31, 32, and 46)

[135] M. P. Diago, J. Fernández-Novales, S. Gutiérrez, M. Marañón, and J. Tardaguila, "Development and validation of a new methodology to assess the vineyard water status by on-the-go near infrared spectroscopy," *Frontiers in Plant Science*, vol. 9, Jan. 2018. [Online]. Available: http://dx.doi.org/10.3389/fpls.2018.00059 (Cited on pages 30 and 46)

[136] S. Ullah, A. K. Skidmore, M. Naeem, and M. Schlerf, "An accurate retrieval of leaf water content from mid to thermal infrared spectra using continuous wavelet analysis," *Science of The Total Environment*, vol. 437, p. 145–152, Oct. 2012. [Online]. Available: http://dx.doi.org/10.1016/j.scitotenv.2012.08.025 (Cited on pages 30 and 31)

[137] S. Ullah, A. K. Skidmore, T. A. Groen, and M. Schlerf, "Evaluation of three proposed indices for the retrieval of leaf water content from the mid-wave infrared (2–6m) spectra," *Agricultural and Forest Meteorology*, vol. 171–172, p. 65–71, Apr. 2013. [Online]. Available: http://dx.doi.org/10.1016/j.agrformet.2012.11.014 (Cited on pages 31 and 32)

[138] M. F. Buitrago, T. A. Groen, C. A. Hecker, and A. K. Skidmore, "Changes in thermal infrared spectra of plants caused by temperature and water stress," *ISPRS Journal of Photogrammetry and Remote Sensing*, vol. 111, p. 22–31, Jan. 2016. [Online]. Available: http://dx.doi.org/10.1016/j.isprsjprs.2015.11.003 (Cited on page 32)

[139] G. PUGLIELLI, L. GRATANI, and L. VARONE, "Leaf rolling as indicator of water stress in cistus incanus from different provenances," *Photosynthetica*, vol. 57, no. 1, p. 202–208, Jan. 2019. [Online]. Available: http://dx.doi.org/10.32615/ps.2019.014 (Cited on page 33)

[140] Y. A. Othman and D. Leskovar, "Leaf orientation method as a proxy for sensing nitrogen and water deficit in tomato plants," *HortScience*, vol. 59, no. 12, p. 1740–1748, Dec. 2024. [Online]. Available: http://dx.doi.org/10.21273/HORTSCI18176-24 (Cited on pages 33 and 85)

[141] E. Bwambale, F. K. Abagale, and G. K. Anornu, "Smart irrigation monitoring and control strategies for improving water use efficiency in precision agriculture: A review," *Agricultural Water Management*, vol. 260, p. 107324, Feb. 2022. [Online]. Available: http://dx.doi.org/10.1016/j.agwat.2021.107324 (Cited on pages 34 and 36)

[142] M. N. Anjum, M. J. M. Cheema, F. Hussain, and R.-S. Wu, *Precision irrigation.* Elsevier, 2023, p. 85–101. [Online]. Available: http://dx.doi.org/10.1016/B978-0-443-18953-1.00007-6 (Cited on pages 34 and 35)

[143] M. A. Derebe and L. A. Asres, "Assessment of surface irrigation potential and crop water demand in daramalo wereda, southern ethiopia," *World Water Policy*, vol. 11, no. 1, p. 304–325, Oct. 2024. [Online]. Available: http://dx.doi.org/10.1002/wwp2.12226 (Cited on page 34)

[144] A. Singh, G. K. Vani, D. Rathi, S. Naberia, and U. Kumar, "Dynamics of surface and groundwater irrigation systems across districts of madhya pradesh in india: An economic analysis," *Journal of Scientific Research and Reports*, vol. 31, no. 7, pp. 1194–1206, 2025, hAL Id: hal-05185873. [Online]. Available: https://hal.science/hal-05185873 (Cited on page 34)

[145] E. L. Gray, A. Rahman, M. Neghaban-Azar, and A. Shirmohammadi, "Watershed-scale investigation of the net-benefit of irrigation with reclaimed water," 2025. [Online]. Available: http://dx.doi.org/10.2139/ssrn.5316621 (Cited on page 34)

[146] B. Kelley, Y. Dong, M. I. Chilvers, and N. Das, "Understanding the impact of irrigation scheduling on water use efficiency in corn and soybean production in humid climates: insights from on-farm demonstration," *Frontiers in Agronomy*, vol. 7, may 2025, section: Field Water Management; Published 30 May 2025. [Online]. Available: https://www.frontiersin.org/journals/agronomy/articles/10.3389/fagro.2025.1496198/full (Cited on page 34)

[147] J. Pathania, P. Verma, S. Bodh, and S. Das, "Role of robotics and artificial intelligence in horticulture for sustainable resource development: A review," *Environmental Engineering and Management Journal*, vol. 24, no. 1, jan 2025. [Online]. Available: https://doi.org/10.30638/eemj.2025.008 (Cited on pages 34 and 35)

[148] J. Manikandan, J. U. Saran, S. Samitha, and K. Rhikshitha, "An effective study on the machine vision-based automatic control and monitoring in furrow irrigation and precision irrigation," p. 323–342, Nov. 2024. [Online]. Available: http://dx.doi.org/10.1002/9781394186686.ch14 (Cited on page 34)

[149] E. M. Haacker, K. A. Cotterman, S. J. Smidt, A. D. Kendall, and D. W. Hyndman, "Effects of management areas, drought, and commodity prices on groundwater decline patterns across the high plains aquifer," *Agricultural Water Management*, vol. 218, p. 259–273, Jun. 2019. [Online]. Available: http://dx.doi.org/10.1016/j.agwat.2019.04.002 (Cited on page 35)

[150] S. Ofori, A. Puškáčová, I. Růžičková, and J. Wanner, "Treated wastewater reuse for irrigation: Pros and cons," *Science of The Total Environment*, vol. 760, p. 144026, Mar. 2021. [Online]. Available: http://dx.doi.org/10.1016/j.scitotenv.2020.144026 (Cited on page 35)

[151] M. Savitha, "Smart crop field irrigation in iot architecture using sensors," *International Journal of Advanced Research in Computer Science*, vol. 9, no. 1, p. 302–306, Feb. 2018. [Online]. Available: http://dx.doi.org/10.26483/ijarcs.v9i1.5348 (Cited on page 35)

[152] E. A. Abioye, M. S. Z. Abidin, M. S. A. Mahmud, S. Buyamin, M. H. I. Ishak, M. K. I. A. Rahman, A. O. Otuoze, P. Onotu, and M. S. A. Ramli, "A review on monitoring and advanced control strategies for precision irrigation," *Computers and Electronics in Agriculture*, vol. 173, p. 105441, Jun. 2020. [Online]. Available: http://dx.doi.org/10.1016/j.compag.2020.105441 (Cited on page 36)

[153] X. Zhang, J. Zhang, L. Li, Y. Zhang, and G. Yang, "Monitoring citrus soil moisture and nutrients using an iot based system," *Sensors*, vol. 17, no. 3, p. 447, Feb. 2017. [Online]. Available: http://dx.doi.org/10.3390/s17030447 (Cited on page 36)

[154] S. Alharbi, A. Felemban, A. Abdelrahim, and M. Al-Dakhil, "Agricultural and technology-based strategies to improve water-use efficiency in arid and semiarid areas," *Water*, vol. 16, no. 13, p. 1842, Jun. 2024. [Online]. Available: http://dx.doi.org/10.3390/w16131842 (Cited on page 36)

[155] P. Zhang, Z. Guo, S. Ullah, G. Melagraki, A. Afantitis, and I. Lynch, "Nanotechnology and artificial intelligence to enable sustainable and precision agriculture," *Nature Plants*, vol. 7, no. 7, pp. 864–876, jul 2021, published online: 24 June 2021. [Online]. Available: https://www.nature.com/articles/s41477-021-00946-6 (Cited on page 36)

[156] V. Choudhary, P. Guha, G. Pau, and S. Mishra, "An overview of smart agriculture using internet of things (iot) and web services,"

Environmental and Sustainability Indicators, vol. 26, p. 100607, Jun. 2025. [Online]. Available: http://dx.doi.org/10.1016/j.indic.2025.100607 (Cited on pages 37, 40, and 104)

[157] J. Mabrouki, M. Azrour, D. Dhiba, Y. Farhaoui, and S. E. Hajjaji, "Iot-based data logger for weather monitoring using arduino-based wireless sensor networks with remote graphical application and alerts," *Big Data Mining and Analytics*, vol. 4, no. 1, p. 25–32, Mar. 2021. [Online]. Available: http://dx.doi.org/10.26599/BDMA.2020.9020018 (Cited on page 37)

[158] K. A and R. Vadivel, "Optimized water management for precision agriculture using iot-based smart irrigation system," *World Journal of Advanced Research and Reviews*, vol. 21, no. 3, p. 802–811, Mar. 2024. [Online]. Available: http://dx.doi.org/10.30574/wjarr.2024.21.3.0682 (Cited on page 37)

[159] K. S. Enock, M. J. Sagali, U. I. Jeannick, and D. Chen, "Lora-based smart agriculture monitoring and automatic irrigation system," *Journal of Computer and Communications*, vol. 13, no. 03, p. 1–20, 2025. [Online]. Available: http://dx.doi.org/10.4236/jcc.2025.133001 (Cited on pages 37 and 116)

[160] Link Labs, "Lora: A breakdown of what it is & how it works," June 2018, explains LoRa as a proprietary PHY and notes Semtech's 2012 acquisition of Cycleo. [Online]. Available: https://www.link-labs.com/blog/what-is-lora (Cited on page 38)

[161] S. Montagny, *LoRa® – LoRaWAN® and Internet of Things: For Beginners*, Annecy, France, 2022, free eBook; updated editions available online. [Online]. Available: https://www.univ-smb.fr/lorawan/wp-content/uploads/2022/01/Book-LoRa-LoRaWAN-and-Internet-of-Things.pdf (Cited on pages 38 and 39)

[162] LoRa Alliance, "Lorawan® 1.0.4 specification," Standard specification, Oct 2020, section on network architecture/topology (star-of-stars). [Online]. Available: https://lora-alliance.org/resource_hub/lorawan-specification-v1-0-4/ (Cited on pages 38 and 39)

[163] The Things Network, "Lorawan architecture (network components and topology)," https://www.thethingsnetwork.org/docs/lorawan/architecture/, n.d., explains gateways, network server, and star-of-stars topology. (Cited on page 38)

[164] The Things Industries, "The things stack: Open source lorawan network server," https://www.thethingsindustries.com/docs/, open-source LoRaWAN stack powering TTN. (Cited on page 40)

[165] ChirpStack Project, "Chirpstack — open-source lorawan network server stack," https://www.chirpstack.io/, project homepage with overview and releases. (Cited on page 40)

[166] N. Hema and K. Kant, "Cost-effective smart irrigation controller using automatic weather stations," *International Journal of Hydrology Science and Technology*, vol. 9, no. 1, pp. 1–27, January 2019. (Cited on page 40)

[167] InfluxData, Inc., *InfluxDB OSS v2 Documentation*, 2025, accessed: 2025-11-01. [Online]. Available: https://docs.influxdata.com/influxdb/v2/ (Cited on page 40)

[168] Grafana Labs, *Grafana Documentation*, 2025, accessed: 2025-11-02. [Online]. Available: https://grafana.com/docs/ (Cited on page 40)

[169] L. González and M. González-Vilar, *Determination of Relative Water Content*. Kluwer Academic Publishers, p. 207–212. [Online]. Available: http://dx.doi.org/10.1007/0-306-48057-3_14 (Cited on page 45)

[170] S. W. Ritchie, H. T. Nguyen, and A. S. Holaday, "Leaf water content and gas-exchange parameters of two wheat genotypes differing in drought resistance," *Crop Science*, vol. 30, no. 1, p. 105–111, Jan. 1990. [Online]. Available: http://dx.doi.org/10.2135/cropsci1990.0011183X003000010025x (Cited on page 45)

[171] Gibertini Elettronica S.r.l. Crystal – Magnetic Compensation Analytical Balance; Gibertini: Milan, Italy, 2024. Available online: https://www.gibertini.com/en/product/crystal (accessed on 28 May 2025). (Cited on page 45)

[172] D. T. MacDougal, "Streaming movements of solutions in plants," *American Journal of Botany*, vol. 33, no. 5, p. 318–328, May 1946. [Online]. Available: http://dx.doi.org/10.1002/j.1537-2197.1946.tb10380.x (Cited on page 45)

[173] N. Makni, S. Loddo, and M. Barbaro, *Real-World Implementation of an Innovative Vineyard Water Management Platform: A Case Study*. Springer Nature Switzerland, 2025, p. 505–513. [Online]. Available: http://dx.doi.org/10.1007/978-3-031-84100-2_60 (Cited on pages 45 and 83)

[174] LITE-ON Technology Corp.; LITE-ON Electronics, Inc. IR Emitter and Detector. Report, April 2000. Available online: https://optoelectronics.liteon.com/upload/download/DS-50-92-0005/E2871.pdf (accessed on 6 May 2025). (Cited on page 47)

[175] Vishay Semiconductors. Silicon PIN Photodiode. Technical Report, July 2011. Available online: https://eeshop.unl.edu/pdf/bpv23f.pdf (accessed on 6 May 2025). (Cited on page 47)

[176] Texas Instruments. OPA2137: Precision Low Noise Operational Amplifier; Texas Instruments: Dallas, TX, USA, 2015. Available online: https://www.ti.com/lit/ds/symlink/opa2137.pdf (accessed on 19 May 2025). (Cited on page 47)

[177] Digilent, Inc. Analog Discovery 2™ Reference Manual. September 2015. Available online: https://cdn-shop.adafruit.com/product-files/4652/4652$_m$*anual.pdf* (*accessed on* 6 *May* 2025). (*Cited on page* 47)

[178] S. Goossens, J. Cappelle, G. Leenders, T. Reher, V. De Smedt, B. Van de Poel, L. De Strycker, and L. Van der Perre, "Lightweight energy-constraint wireless sensor solution for plant monitoring," in *2024 IEEE SENSORS*. IEEE, Oct. 2024, p. 1–4. [Online]. Available: http://dx.doi.org/10.1109/SENSORS60989.2024.10784661 (Cited on page 51)

[179] SenseCAP S2120 8-in-1 LoRaWAN Weather Sensor - Seeed Studio. (Cited on page 59)

[180] SenseCAP S2100 - LoRaWAN® Data Logger - Seeed Studio. (Cited on page 60)

[181] Maize Diseases—Retrospect and Prospect | SpringerLink. (Cited on page 60)

[182] R. Yuvarani, U. Shankar, S. B. Gowdar, S. Kumar, and S. S. Hiremath, *Plant Health and Disease Management: A Modern Approach*. Lucknow, Uttar Pradesh, India: Textify Publishers, 2025. [Online]. Available: https://www.researchgate.net/publication/391264793_Plant_Health_and_Disease_Management_A_Modern_Approach (Cited on page 60)

[183] Industrial PAR Sensor, MODBUS-RTU RS485 - Seeed Studio. (Cited on page 61)

[184] *RAK7249 WisGate Edge Max Datasheet*, RAKwireless Technology Co., Ltd., Shenzhen, China, n.d., product datasheet for the RAK7249 LoRaWAN gateway. [Online]. Available: https://docs.rakwireless.com/product-categories/wisgate/rak7249/datasheet/ (Cited on page 62)

[185] M. Sugiyama and M. Okajima, "Application of electrochemical impedance spectroscopy and modeling of the novel equivalent circuit for monitoring cellular tissues," *Theoretical and Experimental Plant Physiology*, vol. 34, no. 4, p. 501–508, Sep. 2022. [Online]. Available: http://dx.doi.org/10.1007/s40626-022-00260-2 (Cited on page 72)

[186] S. Yin and L. Dong, "Plant tattoo sensor array for leaf relative water content, surface temperature, and bioelectric potential monitoring," *Advanced Materials Technologies*, vol. 9, no. 12, Apr. 2024. [Online]. Available: http://dx.doi.org/10.1002/admt.202302073 (Cited on page 72)

[187] A. Mascia, R. Collu, N. Makni, M. Concas, M. Barbaro, and P. Cosseddu, "Impedance characterization and modeling of gold, silver, and pedot:pss ultra-thin tattoo electrodes for wearable bioelectronics," *Sensors*, vol. 25, no. 15, p. 4568, Jul. 2025. [Online]. Available: http://dx.doi.org/10.3390/s25154568 (Cited on page 72)

[188] J. A. Barbosa, V. M. S. Freitas, L. H. B. Vidotto, G. R. Schleder, R. A. G. de Oliveira, J. F. da Rocha, L. T. Kubota, L. C. S. Vieira, H. C. N. Tolentino, I. T. Neckel, A. L. Gobbi, M. Santhiago, and R. S. Lima, "Biocompatible wearable electrodes on leaves toward the on-site monitoring of water loss from plants," *ACS Applied Materials & Interfaces*, vol. 14, no. 20, p. 22989–23001, 2022. [Online]. Available: https://doi.org/10.1021/acsami.2c02943 (Cited on pages 72 and 83)

[189] M. Murbach, B. Gerwe, N. Dawson-Elli, and L.-k. Tsui, "impedance.py: A python package for electrochemical impedance analysis," *Journal of Open Source Software*, vol. 5, no. 52, p. 2349, Aug. 2020. [Online]. Available: http://dx.doi.org/10.21105/joss.02349 (Cited on page 73)

[190] P. Virtanen, R. Gommers, T. E. Oliphant, M. Haberland, T. Reddy, D. Cournapeau, E. Burovski, P. Peterson, W. Weckesser, J. Bright, S. J. van der Walt, M. Brett, J. Wilson, K. J. Millman, N. Mayorov, A. R. J. Nelson, E. Jones, R. Kern, E. Larson, C. J. Carey, Polat, Y. Feng, E. W. Moore, J. VanderPlas, D. Laxalde, J. Perktold, R. Cimrman, I. Henriksen, E. A. Quintero, C. R. Harris, A. M. Archibald, A. H. Ribeiro, F. Pedregosa, P. van Mulbregt, A. Vijaykumar, A. P. Bardelli, A. Rothberg, A. Hilboll, A. Kloeckner, A. Scopatz, A. Lee, A. Rokem, C. N. Woods, C. Fulton, C. Masson, C. Häggström, C. Fitzgerald, D. A. Nicholson, D. R. Hagen, D. V. Pasechnik, E. Olivetti, E. Martin, E. Wieser, F. Silva, F. Lenders, F. Wilhelm, G. Young, G. A. Price, G.-L. Ingold, G. E. Allen, G. R. Lee, H. Audren, I. Probst, J. P. Dietrich, J. Silterra, J. T. Webber, J. Slavič,

J. Nothman, J. Buchner, J. Kulick, J. L. Schönberger, J. V. de Miranda Cardoso, J. Reimer, J. Harrington, J. L. C. Rodríguez, J. Nunez-Iglesias, J. Kuczynski, K. Tritz, M. Thoma, M. Newville, M. Kümmerer, M. Bolingbroke, M. Tartre, M. Pak, N. J. Smith, N. Nowaczyk, N. Shebanov, O. Pavlyk, P. A. Brodtkorb, P. Lee, R. T. McGibbon, R. Feldbauer, S. Lewis, S. Tygier, S. Sievert, S. Vigna, S. Peterson, S. More, T. Pudlik, T. Oshima, T. J. Pingel, T. P. Robitaille, T. Spura, T. R. Jones, T. Cera, T. Leslie, T. Zito, T. Krauss, U. Upadhyay, Y. O. Halchenko, and Y. Vázquez-Baeza, "Scipy 1.0: fundamental algorithms for scientific computing in python," *Nature Methods*, vol. 17, no. 3, p. 261–272, Feb. 2020. [Online]. Available: http://dx.doi.org/10.1038/s41592-019-0686-2 (Cited on page 73)

[191] J. Nocedal and S. J. Wright, *Numerical Optimization*, 2nd ed., ser. Springer Series in Operations Research and Financial Engineering. New York, NY, USA: Springer, 2006. (Cited on page 74)

[192] J. Peñuelas and I. Filella, "Visible and near-infrared reflectance techniques for diagnosing plant physiological status," *Trends in Plant Science*, vol. 3, no. 4, p. 151–156, Apr. 1998. [Online]. Available: http://dx.doi.org/10.1016/S1360-1385(98)01213-8 (Cited on page 78)

[193] J. Peñuelas, S. Munné-Bosch, J. Llusià, and I. Filella, "Leaf reflectance and photo- and antioxidant protection in field-grown summer-stressed phillyrea angustifolia. optical signals of oxidative stress?" *New Phytologist*, vol. 162, no. 1, p. 115–124, Jan. 2004. [Online]. Available: http://dx.doi.org/10.1046/j.1469-8137.2004.01007.x (Cited on page 78)

[194] C. Shimbori and Y. Kurata, "Nondestructive measurement of water content in hardwood leaves using near-infrared spectroscopy," *BioResources*, vol. 12, no. 4, p. 9244–9252, Oct. 2017. [Online]. Available: http://dx.doi.org/10.15376/biores.12.4.9244-9252 (Cited on page 78)

[195] K. Sand-Jensen, J. Borum, C. L. Møller, and L. Baastrup-Spohr, "Physiological adaptation and plant distribution along a steep hydrological gradient," *Plants*, vol. 11, no. 13, p. 1683, Jun. 2022. [Online]. Available: http://dx.doi.org/10.3390/plants11131683 (Cited on page 78)

[196] M. M. Nour, H. R. Aljabi, A. A. AL-Huqail, B. Horneburg, A. E. Mohammed, and M. O. Alotaibi, "Drought responses and adaptation in plants differing in life-form," *Frontiers in Ecology and Evolution*, vol. 12, Nov. 2024. [Online]. Available: http://dx.doi.org/10.3389/fevo.2024.1452427 (Cited on page 78)

[197] S. M. Gleason, D. R. Wiggans, C. A. Bliss, J. S. Young, M. Cooper, K. R. Willi, and L. H. Comas, "Embolized stems recover overnight in zea mays: The role of soil water, root pressure, and nighttime transpiration," *Frontiers in Plant Science*, vol. 8, Apr. 2017. [Online]. Available: http://dx.doi.org/10.3389/fpls.2017.00662 (Cited on page 78)

[198] M. Delacre, D. Lakens, and C. Leys, "Why psychologists should by default use welch's t-test instead of student's t-test," *International Review of Social Psychology*, vol. 30, no. 1, p. 92–101, Apr. 2017. [Online]. Available: http://dx.doi.org/10.5334/irsp.82 (Cited on page 78)

[199] X. Jin, C. Shi, C. Y. Yu, T. Yamada, and E. J. Sacks, "Determination of leaf water content by visible and near-infrared spectrometry and multivariate calibration in *miscanthus*," *Frontiers in Plant Science*, vol. 8, p. 721, 2017. [Online]. Available: https://doi.org/10.3389/fpls.2017.00721 (Cited on page 79)

[200] E. Serrano-Finetti, A. Martínez-Morales, M. J. Zhang, I. G. Rossi, F. Casini, L. Campanello, A. Nardi, P. Pinna, and A. Porfiri, "Toward noninvasive monitoring of plant leaf water content: A multi-frequency electrical impedance spectroscopy approach," *Sensors and Actuators A: Physical*, vol. 359, p. 114231, 2023. [Online]. Available: https://doi.org/10.1016/j.sna.2023.114231 (Cited on page 81)

[201] J. Ma, K. Liu, C. Chen, F. Ahmad, and B. Qiu, "Influence of plant leaf moisture content on retention of electrostatic-induced droplets," *Sustainability*, vol. 13, no. 21, p. 11685, 2021. [Online]. Available: https://doi.org/10.3390/su132111685 (Cited on page 81)

[202] S. Seker *et al.*, ""on-plant" wearable electrochemical sensor for aerosol lead (pb) detection in atmospheric samples," *Science of the Total Environment*, vol. 965, p. 174053, 2025. [Online]. Available: https://doi.org/10.1016/j.scitotenv.2025.174053 (Cited on page 83)

[203] K. McCree, "The measurement of photosynthetically active radiation," *Solar Energy*, vol. 15, no. 1, p. 83–87, May 1973. [Online]. Available: http://dx.doi.org/10.1016/0038-092X(73)90010-8 (Cited on pages 88 and 98)

[204] Lifely: Costruisci il tuo smart garden. Provisional entry — fill author/org/date. [Online]. Available: https://www.lifely.cc/it/ (Cited on page 105)

[205] Abinsula - costruisci un software personalizzato per la tua azienda. Provisional entry — fill author/org/date. [Online]. Available: https://abinsula.com/it/ (Cited on page 105)

[206] Spritz – istituto per la bioeconomia. Provisional entry — fill author/org/date. [Online]. Available: https://www.ibe.cnr.it/progetti/spritz/ (Cited on page 105)

[207] Agriturismo agave alghero. Provisional entry — fill author/org/date. [Online]. Available: https://www.agriturismoagave.com/ (Cited on page 105)

[208] C. Pham, *Building Low-Cost Gateways and Devices for Open LoRa IoT Test-Beds*. Springer International Publishing, Nov. 2016, p. 70–80. [Online]. Available: http://dx.doi.org/10.1007/978-3-319-49580-4_7 (Cited on page 107)

[209] SPRITZ Project, "Spritz dashboard," https://spritzpro.com/dashboard/, 2025, accessed: 2025-10-21. (Cited on page 112)

[210] A. Morchid, Z. Said, A. Y. Abdelaziz, P. Siano, and H. Qjidaa, "Fuzzy logic-based iot system for optimizing irrigation with cloud computing: Enhancing water sustainability in smart agriculture," *Smart Agricultural Technology*, vol. 11, p. 100979, Aug. 2025. [Online]. Available: http://dx.doi.org/10.1016/j.atech.2025.100979 (Cited on page 115)

[211] C. M. A. Kalaany, H. N. Kimaita, A. A. Abdelmoneim, R. Khadra, B. Derardja, and G. Dragonetti, "The potential of low-cost iot-enabled agrometeorological stations: A systematic review," *Sensors*, vol. 25, no. 19, p. 6020, Oct. 2025. [Online]. Available: http://dx.doi.org/10.3390/s25196020 (Cited on page 115)

[212] E. Artetxe, O. Barambones, I. Martín Toral, J. Uralde, I. Calvo, and A. del Rio, "Smart iot irrigation system based on fuzzy logic, lora, and cloud integration," *Electronics*, vol. 13, no. 10, p. 1949, May 2024. [Online]. Available: http://dx.doi.org/10.3390/electronics13101949 (Cited on page 116)

Acknowledgements

This thesis was produced while attending the PhD programme in Electronics and Computer Engineering at the University of Cagliari, Cycle XXXVIII, with the support of a scholarship co-financed by the Ministerial Decree no. 352 of 9th April 2022, based on the NRRP - funded by the European Union - NextGenerationEU - Mission 4 “Education and Research”, Component 2 “From Research to Business”, Investment 3.3, and by the company Abinsula S.r.l.